THE UNIVERSITY OF CHICAGO

BRIGHT INFRARED NANOCRYSTALS: SYNTHESIS AND NONRADIATIVE MECHANISMS

A DISSERTATION SUBMITTED TO
THE FACULTY OF THE DIVISION OF THE PHYSICAL SCIENCES
IN CANDIDACY FOR THE DEGREE OF
DOCTOR OF PHILOSOPHY

DEPARTMENT OF CHEMISTRY

BY
ANANTH KAMATH

CHICAGO, ILLINOIS
DECEMBER 2023

To my family.

"Emotional maturity is the compass guiding the voyage of success; intelligence is merely the wind in its sails. Alone, it can lead us off course, but paired with emotional understanding, it propels us to our true destination." - Unknown

TABLE OF CONTENTS

LIST OF FIGURES

LIST OF TABLES

ACKNOWLEDGMENTS

I want to thank Philippe for having me in the group. It hasn't been a smooth journey, but it was a great learning experience, and has made me the scientist I am today. I want to thank all my group members for their help: Guohua Shen, Xin Tang, Matt Ackerman, Chris Melnychuk, Haozhi Zhang, John Peterson, Xingyu Shen, and Augustin Caillas.

First and foremost, I am thankful to my family for their support. I am especially thankful to my father, who gave me the freedom and upbringing to make bold decisions in my career, and pursue a path that I found the most rewarding. I want to thank my mother for her eternal support during our daily morning phone calls. I want to thank Arjunanna and Ashwini for always being there for me. I want to thank Chaya pacchi who traveled all the way from India to attend my defense and convocation. I want to thank my music teacher, Meera aunty, who I consider as part of my family. She has been there for my during my toughest times, and I am extremely grateful for her support.

It was difficult moving to the US away from my family in India, and it was so much smoother because of my relatives here. I want to thank all my relatives in the US: Sandesh bappa's family at New Jersey, Prathiba mayi's family at New York, Shanthakka's family in New Jersey, Prachi and Anshu at New Jersey, Amitanna's family at South Carolina, Vidya mami's family at South Carolina, and Aditi pacchi's family at Atlanta.

I want to thank Ashwin Rode who I met during my first year, and has provided constant encouragement to pursue my passion in Hindustani Classical Music.

During my time at Chicago, I have made countless friends, and unfortunately it is difficult to thank everyone in this section. I first want to thank Anuva and Sarthak at Urbana-Champaign, who were my lifeline during my times of crisis; and Ram, who has been my closest friend throughout. I want to thank members of the Gobi group: Sridevi, Shriya, Naren, Subhayan, Alistair, Avishek and Arpan. I had a lot of fun during our video calls. I want to thank members of the shellshock group: Anuva, Sarthank, Esha, Amruta, Mandu,

Biswadeep and Suvam, for the fun weekly games during the pandemic. I also want Agnish, Manish and Pranjal; Sam and Michael from our first year board game group; Srijanee from the Urbana group; Aritrajit my roommate.

A new chapter of my life begun when I started my pivot towards neuroscience and bioengineering. The biggest source of inspiration was Prof. Aneesh Vettil, who picked me up during the darkest times of my PhD, and inspired me to find a field that I found exciting and fulfilling. Talking to him has helped me have an unbelievable amount of optimism and stubbornness, which helped me stick to my path, unperturbed by the loads of discouragement I encountered along the way. I want to thank Prof. Bozhi Tian, who has been a source of unlimited support, and has helped and encouraged me in any way possible. My PhD journey was hugely influenced by my mentors outside my group, who were available for periodic check-ins, provided me constant encouragement and feedback, provided recommendation letters, and with whom I could be myself, and felt truly understood. I want to thank Michael Tessel, Vera Dragisich, Aaron Dinner, Amanda Young, Allison Squires, Dmitri Talapin, S Ramakrishnan, Gautam Bharali, and Anshu Pandey. I want to thank Poojya Ravishankar and Nabilah Hamdiah, who are the neuroscientists who provided constant support during my pivot.

I want to thank Claire, who has been my constant neuroscience buddy, and who fills me with energy every time we chat. I have been able to sustain my motivation in my pivot because of support from all my friends: Shi En Kim, Matt Ackerman, Tomojit Chowdhury, Fauzia Mujid, James Callahan, Melina Vanni-Gonzales, Chaitra Agrahar, Annika Hirmke, Kavya Pillai, Adarsh Suresh, Naga Bhavya Teja, Lavanya Taneja, Shubhashree Pani, Siddhartha Sohoni, Chuanwang Yang, Baorui Cheng, Brennan Ashwood, Irma Avdic, Anuj Apte, and Nesar Ramachandra.

I finally want to thank my plants, who made my apartment feel like home; and the Ram's cats: Kalu Itani and Maya Itani, who always filled me with joy.

ABSTRACT

The field of semiconductor quantum dots has seen tremendous progress over the last few decades. Although quantum dots emitting at visible wavelengths have been extensively studied and display near-unity quantum yields, quantum dots remain relatively poor emitters in the midwave- shortwave- infrared wavelengths. Quantum dots hold immense potential for fabricating low cost infrared detectors and emitters, but their performance is severely limited by their poor emission efficiency and fast nonradiative relaxation. In my PhD, I have developed methods to slow the nonradiative rate in quantum dots in midwave- and shortwave- infrared wavelengths, and developed insights into the underlying nonradiative mechanisms.

CHAPTER 1

INTRODUCTION

1.1 Infrared quantum dots

Colloidal quantum dots (QDs) are semiconductor nanoparticles that are a few nanometers in size. From a commercial perspective, the two most attractive properties of QDs are their size-tuneable optical properties, and their solution processibility [13]. In contrast to bulk semiconductors that need to be fabricated by expensive vapor-phase lithography, QDs can be synthesized by a simple solution-phase chemical synthesis. This solution processibility leads to much lower costs, with added benefits such as large-scale fabrication, and preparing flexible devices [13].

By a simple tweaking of the synthetic conditions, the energy levels of the QDs can be modified. This 'color tuning' enables generation of materials with precise emission properties. The most popular commercial application of QDs is as phosphors in TVs, due to the much better color purity of QDs compared to OLEDs. A comprehensive review of the QD field can be found in the reviews elsewhere [13, 14].

In contrast to QDs emitting in the visible wavelengths, which are the most widely studied systems in the field, QDs emitting in the infrared are far less studied. The infrared spectrum comprises of three windows: the near-infrared (NIR, 780nm - 2.5μm), midwave-infrared (MWIR, 2.5μm - 8μm), longwave-infrared (LWIR, 8μm - 15μm) and far-infrared (FIR, 15μm - 1mm). The NIR is further subdivided into regions called NIR-I (780nm - 1μm) and NIR-II (1.3μm - 2.5μm). The NIR-II region is also called the shortwave infrared (SWIR). The chief applications of infrared QDs are as detectors and emitters. SWIR detectors have applications in low-visibility imaging, spectroscopy and gas sensing [15], and MWIR detectors have applications in gas sensing, thermal detection and spectroscopy [16, 17]. MWIR and SWIR emitters have applications in gas sensing and spectroscopy. SWIR emitters also

have application in bioimaging, as fluorophores at this wavelength range undergo much less scattering in tissue as compared to visible wavelengths [9, 4].

A chief benefit of infrared QDs over their visible counterparts is the lack of alternative materials showing high performance. While organic semiconductors offer a low-cost alternative to inorganic materials as visible emitters, organic molecules display very poor performance in the infrared wavelengths. The PLQY of organic semiconductors is several orders of magnitude lower than QDs (See Fig. 1.4 in Ref. [18]), making them unfeasible for fabricating infrared detectors and emitters. As a result, the only alternative materials are bulk semiconductors. The fabrication requirement for bulk semiconductor crystals makes the detectors extremely expensive. For instance, the state-of-the art mid-infrared detectors are made from mercury cadmium telluride alloys (MCT), which requires fabrication by molecule-beam epitaxy and flip-chip bonding. The solution-processibility of QDs brings down the material drastically, and can lead to much lower costs of the infrared detectors. This will open infrared detection for use in consumer markets such as self-driving cars, which were previously impractical due to the prohibitive cost.

1.2 Nonradiative mechanisms

Despite their advantages, the PLQY of QDs has been very low [19]. In contrast to the gold-standard CdSe/CdS QDs that have PLQY of $\sim$100% at visible wavelengths, the brightest PLQY of infrared QDs are $\sim$40% in the SWIR [5], and only $\sim$0.1% in the MWIR [20]. The low emission efficiency makes MWIR QDs noncompetitive against thermal light sources. The low PLQY of the MWIR QDs also results in poorer mid-infrared detectors. The fast nonradiative decay responsible for the low PLQY results in a higher dark current due to thermal recombination [19]. In order to slow the recombination, the detectors have to be cooled to cryogenic temperatures, which makes the cameras bulky and expensive. Hence, in order to obtain high-performance low-cost MWIR detectors and emitters, it is necessary to

overcome the fast nonradiative relaxation in these materials [19].

To design strategies to slow the nonradiative relaxation, it is essential to understand the mechanisms governing the relaxation. The most common nonradiative mechanism in QDs in surface trapping, where an undercoordinated surface atom leads to a defect state with energy lying within the bandgap [21]. After photoexcitation, the either the electron or hole can relax to this defect state, and remaining essentially non-emissive. Surface trapping is also called Shockey-Reed-Hall (SRH) recombination, and it plays a dominant role in bulk semiconductors. In QDs with bandgap in the visible and near-infrared, surface trapping is the dominant relaxation mechanism [21].

For QDs emitting in the infrared, two other relaxation mechanisms are observed. One mechanism is a near-field Forster resonance energy transfer (FRET) to ligand vibrations on the QD surface, which was first proposed by Guyot-Sionnest and coworkers [22]. Due to the nanometer- separation between the QD center and the ligands, and due to the strong absorption of ligands in the infrared, this mechanism plays a dominant role in QDs emitting in the SWIR and MWIR. A third mechanism that might play an important role is nonradiative decay to lattice phonons [23, 24, 25, 26]. Phonon vibrations in QDs have an energy of $\sim$100-300 cm^{-1}. After photoexcitation, the QD exciton can relax via coupling to a high-order multiphonon transition, either by a direct quantum-mechanical coupling, or by a radiative Forster energy transfer. Though this involves a high-order ($>\sim$10) nonlinear phonon process, the rate could be enhanced due to the higher anharmonicity of phonon modes on the QDs surface [27]. It is important to determine the underlying nonradiative mechanism, as it will dictate the strategy to employ to overcome it.

Surface trapping can be overcome by suitable coordination of the defect states on the QD surface. This can be achieved either by coordinating the QDs with suitable ligands, or by growth of an epitaxial type-I shell [21]. The shell is said to have a type-I alignment when the conduction band of the shell is at a higher energy than the core, and the valence band

is at a lower energy than the core. This leads to confinement of the electron and hole to the core of the core/shell QD, and creation of a tunneling barrier between the exciton and the surface defect state. Growth of an epitaxial shell is the most common way to obtain bright QDs, and this has led to development of visible-emitting CdSe/CdS QDs with PLQYs approach 100% [28]. Growing a shell has its limitations however. The shell material should be lattice-matched to the core to minimize strain upon epitaxial growth. Introduction of lattice strain has been shown to lead to a decrease in PLQY at large shell thicknesses [29]. Another challenge with growth of a shell is that it introduces an insulating barrier between the core QD and the environment, and leads to a poor mobility in QD devices [19]. For obtaining better-performing mid-IR QD detectors and emitters, shell growth should either be minimized, or limited to a small thickness.

FRET to ligands can be overcome by passivation of QDs by ligands that have minimal absorption at the QD emission frequency, or by growth of a type-I shell to separate the QD emitter and the ligand absorbers [22, 30]. If the nonradiative mechanism is dominated by relaxation to lattice phonons, little can be done to overcome it, as it is intrinsic to the QD material. Use of QD materials with a low phonon frequency, a low electron-phonon coupling and low anharmonicity could possibly lower the multiphonon relaxation rate.

The most common strategy to experimentally determine the relaxation mechanism is through a measurement of the temperature-dependence of the nonradiative rate γ_{nr}. Surface trapping shows an activated Arrhenius-type exponential behavior with temperature [31]:

$$\gamma_{nr} \propto e^{\frac{-E_b}{k_B T}} \tag{1.1}$$

where E_b is the activation barrier. This should manifest as a linear trend in a log-linear plot between the nonradiative rate and $\frac{1}{T}$.

Under the limit of low electron-phonon coupling and low anharmonicity, multiphonon relaxation shows an exponential dependence on the temperature and the phonon order 'n'

[32]:

$$\gamma_{nr} \sim T^n$$
$$n = \frac{\omega_{QD}}{\omega_0} \tag{1.2}$$

where ω_{QD} and ω_0 are the emission frequencies of the QD and phonon mode respectively. This should show as a linear trend in a log-log plot between the nonradiative rate and T. It should also show as a linear trend in a log-linear plot between the nonradiative rate and ω_{QD}.

In contrast to the temperature dependence of surface trapping and multiphonon relaxation, FRET to ligands is temperature independent. Hence, measurement of the temperature-dependent PLQY will help determine the nonradiative relaxation.

Another method to determine the relaxation mechanism is through the different effects of the shell thickness on the PLQY. For surface trapping $\gamma_{nr} \sim e^{\frac{-t}{t_0}}$ [33], where t is the shell thickness, and t_0 is a measure of the tunneling barrier arising from the shell. For ligand FRET $\gamma_{nr} \sim R^{-4}$ [22] where R is the total core/shell QD radius, and for multiphonon relaxation the nonradiative rate is independent of shell thickness. Thus, measurement of the nonradiative rate as a function of shell thickness will help determine the relaxation mechanism.

A comprehensive description of different nonradiative mechanisms and their impact on QD devices can be found in the PhD thesis of Dr. Christopher Melnychuk [18].

1.3 Shell growth for mercury chalcogenide QDs

Since the early years of development of quantum dots (QDs), growth of a semiconductor shell around the QD has been the go-to method for enhancing the photoluminescence quantum yield (PLQY) [34, 29]. For QDs emitting at visible wavelengths, the dominant nonradiative

mechanism is surface trapping. By growing a shell with a type-I shell material, a tunneling barrier is introduced between the exciton and the trap states, leading to a drastic improvement in PLQY with even a relatively thin shell (∼3 monolayers) [34, 29].

For HgSe and HgTe QDs emitting in the mid-infrared (∼5 μm wavelength), which are the most promising candidates as mid-infrared active materials [35, 7, 17], only a small increase in the PLQY is observed upon growth of a thin shell [20, 36]. The PL also shows a negligible temperature dependence, which suggests that surface trapping might be playing an insignificant role in these systems [20]. Measurement of PLQY of HgTe QDs suggest that FRET to surface ligands might play a dominant role in QDs emitting at infrared wavelengths. When the measured PLQY of HgTe QDs as a function of size was compared to the calculated PLQY by a FRET to oleylamine ligands, a good agreement was observed [7]. The FRET mechanism was also supported by measurements of intraband lifetime in optically excited CdSe- based core/shell QDs [30]. The measured intraband lifetime showed a good agreement with the calculated FRET rate, where a significant lengthening was observed only on growth of a thick shell (∼10 monolayers).

These works provide the motivation for growing a thick shell on HgSe and HgTe QDs. Despite several attempts to grow a thick type-I shell around HgSe and HgTe QDs, growth of only a thin shell (<∼3 monolayers) has been achieved [20, 36, 37]. In addition, there has been no conclusive demonstration of the nonradiative mechanism, and the PLQY has been low in the SWIR (<∼40% at 1.5μm [5]) and MWIR (<∼0.1% at 5μm [20]). In my PhD research, I have developed strategies for the growth of a thick type-I shell around HgSe QDs, to obtain bright emission at 5 μm through the intraband transition [38], and at 1.7μm - 2μm through the interband transition [39]. My work demonstrated ligand-FRET as the dominant nonradiative mechanism in these wavelength ranges. By growth of the thick shell, we have achieved the synthesis of QDs with PLQY of 2% at 5 μm and 63% at 1.7 μm, which are the brightest reports to-date.

CHAPTER 2

DESIGN OF THICK SHELL QUANTUM DOTS

In contrast to visible-emitting QDs like CdSe, growth of a type-I shell on HgSe QDs has unique challenges. The most feasible shell candidates for HgSe cores are CdSe and CdS, due to their type-I band alignment, crystal structure match (zincblende), and low lattice mismatch (4% for CdS and 0% for CdSe). However, there is a large difference between the growth temperatures for HgSe cores, and CdS or CdSe shell. While HgSe QDs are typically grown at temperatures around 100°C - with Ostwald ripening being observed at higher temperatures - CdS and CdSe QDs are typically grown at temperatures in excess of 200°C [40, 41, 42, 43, 44, 45, 46, 47, 48, 49].

To avoid ripening of the cores during the shell growth, previous reports have used low temperatures (<100°C) for growth of a CdS or CdSe shell on HgSe QDs [20, 36, 37]. The shell was either grown at room temperature by a biphasic cALD procedure [20, 37], or at 100°C using highly reactive Cd- and S- precursors [36]. These procedures were successful in growing a shell upto 3 monolayers. In the case of cALD growth, further half- cycles did not lead to a thicker shell [20], and in the case of hot-injection at 100°C, homogeneous nucleation of the shell material was observed [36]. When a CdSe shell was grown at 200°C using $Cd(oleate)_2$ and TOPSe, a tetrahedral shell was observed, with an insignificant effect on the intraband PLQY [20]. These reports show that homogeneous nucleation and faceted / irregular shell growth are the greatest challenges for growth of a thick shell on HgSe QDs.

It is typically assumed that QDs grow by a LaMer growth mechanism, where the growth rate is controlled by diffusion of precursors to the QD surface, and the kinetics of QD growth independent of the QD size [50, 51]. However, an early report by Mulvaney and coworkers on growth of CdSe/CdS QDs suggest a deviation from the LaMer model [42]. Most protocols for shell growth employ a SILAR (Selective Ion Layer Adsorption and Reaction) protocol [52], where the cationic and anionic precursors are alternatively added, with a

certain reaction time between additions to ensure complete reaction of the precursor. This protocol is based on the reasoning that each half-reaction will lead to a saturation of the QD surface, and no unreacted precursor should remain in solution when the other reagent is added. Homogeneous nucleation can thus be avoided, in principle, if the precursor amounts are precisely calculated and the reaction time is long enough. However, Mulvaney and coworkers observe that the shell saturates upto a particular size, which depended on the growth temperature. After reaching this size, further precursor addition led to homogeneous nucleation of the shell material. This could not be prevented even upon increasing the reaction time [42]. The shell did not grow thicker unless the reaction temperature was increased. These observations suggest the importance of reaction kinetics for shell growth on QDs: the rate of monomer deposition on the QD surface is size-dependent. When the QD size is large enough, the activation barrier for growth is too large at that temperature, which leads to homogeneous nucleation upon addition of further precursors [42].

This hypothesis is supported by the fact that all successful protocols for growth of a thick CdS or CdSe shell on CdSe [40, 41, 42, 43, 44], PbS [45], PbSe [46, 47], ZnSe [48] and InP [49] QDs use high reaction temperatures in the 240-300°C range. When the temperature is high enough, homogeneous nuclei become unstable, and deposit on the larger core/shell QDs by Ostwald ripening. Under these conditions, both the cationic and anionic reagents can be injected simultaneously without observing homogeneous nucleation, such as the CdSe/CdS growth protocol by Bawendi and coworkers [43]. These observations show the necessity of a high temperature for avoiding homogeneous nucleation during growth of a thick shell on HgSe QDs.

Apart from avoiding homogeneous nucleation, a high reaction temperature also leads to a spherical shell morphology, instead of faceting or an irregular shell growth. This is observed in HgSe/CdSe and HgTe QDs, where a tetrahedral morphology is observed [20, 53]. In order to obtain a spherical growth and avoid faceting, it is necessary to perform shell growth under

a kinetic regime. This can be achieved when the reaction temperature is significantly higher than the minimum temperature required for decomposition of the shell growth reagents.

Using the above design principles, we have achieved a spherical shell growth without homogeneous nucleation, by using highly reactive shell precursors, at high growth temperatures [38, 39]. The upper limit of the temperature is set by the onset of alloying at the core/shell interface. HgSe/CdSe and HgSe/CdS QDs show interfacial alloying at temperatures above around 250°C [20] . To prevent interfacial alloying, we have set 220°C as the upper limit for the shell growth. For synthesis of HgSe/CdS QDs, we have used $Cd(DEDTC)_2$ as a highly reactive single-source CdS precursor at 220°C (Chapter 3), and for HgSe/CdSe QDs, we have used $Cd(acetate)_2$ and Se/OAm as highly reactive CdSe precursors at 200-220°C (Chapter 4).

Before performing the thick shell growth at these elevated temperatures, it is necessary to grow a thin shell on HgSe QDs at temperatures <100°C to impart thermal stability and avoid core ripening [20]. Although this could be done at room temperature using cALD [20, 37], we avoided it due to its limited scalability and tedious procedure. In Chapters 3 and 4, we have developed the synthesis of a thin CdS and CdSe shell on HgSe QDs at 90-100°C by a hot-injection procedure [38, 39]. This reaction was simple, and could easily be scaled upto 80mg of HgSe QDs.

CHAPTER 3

NONRADIATIVE MECHANISMS IN THE MID-INFRARED

This section has been adapted from Kamath et. al. [38]

3.1 Introduction

The control of intraband carrier relaxation in semiconductor quantum dots (QDs) is a long-standing topic of interest due to its central role in QD optoelectronic technologies [54, 14, 55]. In applications utilizing the interband emission of light, such conventional QD lasers and LEDs, fast intraband relaxation is desired. In contrast, other applications such as solar energy harvesting utilizing hot-carrier extraction and carrier multiplication, are significantly aided when intraband relaxation is slow [56, 57, 58]. Slow intraband relaxation is also required when intraband transitions, typically between the two lowest quantized conduction levels $1S_e$ and $1P_e$, are utilized directly for light emission and detection such as in infrared optoelectronics [35, 19, 1, 59, 60, 61]. It is therefore of broad practical importance to understand and control intraband relaxation rates.

Due to the large energy spacing between QD conduction states, it was initially believed that electronic relaxation should be very slow due to the low expected rate of multiphonon emission across such gaps. This is known as the "phonon bottleneck" effect [62]. Electronic phonon bottlenecks are rarely observed in practice, however, because electrons can undergo sub-picosecond relaxation by coupling to a valence hole in a process known as Auger cooling [56, 63, 64, 65, 66]. Experiments which inhibit Auger cooling, either by hole localization [30, 22, 67] or by n-doping [1, 68], accomplish slower relaxation rates which are often attributed to Forster-like near-field energy transfer involving surface ligand vibrations [1, 30, 22, 7, 8]. This usually produces intraband lifetimes of tens to hundreds of picoseconds [1, 22, 67, 68]. Prior to the present work, the longest reported intraband lifetime at 5 µm (2000 cm^{-1}) was 1.5

ns in a thick-shell CdSe/ZnS/ZnSe/CdSe QD heterostructure passivated by hole-extracting ligands [30].

Recent atomistic simulations [23] using a semiclassical electron-phonon coupling framework [24] predict that a ∼1 ns lifetime is the fundamental upper limit due to phonon processes intrinsic to all nanocrystals. Fully quantum-mechanical models, however, imply that much longer microsecond lifetimes are attainable when electron-phonon coupling and lattice anharmonicity are small, as in II-VI semiconductors [25, 26]. Furthermore, molecular dynamics simulations and neutron scattering experiments have suggested the presence of strong surface-derived anharmonicities which could fundamentally limit intraband lifetimes to sub-nanosecond levels [27, 69]. There is consequently a substantial uncertainty regarding the basic limits on maximum achievable intraband lifetimes. A natural experimental test would be to examine the intraband lifetime in a strongly confined QD where Auger cooling, nonradiative energy transfer, and other non-phonon relaxation mechanisms are minimized.

As a first step to address this issue, we report here the synthesis and spectroscopy of thick shell n-type HgSe/CdS core/shell QDs. HgSe QDs are a convenient system for studies of intraband electronic relaxation due to their air-stable n-doping [35, 70], intraband photoluminescence and absence of Auger electron cooling [1]. They are also investigated for mid-infrared optoelectronics due to suppressed multicarrier Auger recombination [1], solution processability and greatly reduced material costs relative to epitaxial materials [35, 71]. Prior studies focused on HgSe QDs with no shell or thin shells [1, 36, 37, 20], and the intraband photoluminescence quantum yields (PLQYs) remained around 0.1% [20], indicating sub-nanosecond intraband nonradiative lifetimes [1]. When growing core/shell nanocrystals, high temperatures are usually needed to promote a compact shell growth. Established procedures for growing thick CdE (E=S/Se) shells on CdSe [40, 41, 42, 43, 44], PbS [45], PbSe [46, 47], ZnSe [48] and InP [49] QDs demand temperatures in the 240°C - 300°C temperature range. This substantially exceeds the alloying temperature for HgSe/CdS [20] and motivates

the development of a new synthetic protocol. Although HgSe/CdS can be grown by colloidal atomic layer deposition (cALD), such procedures are prone to substantial homogeneous nucleation of CdS nanocrystals after a few shell layers [37, 20].

In this work, the synthesis of thick-shell HgSe/CdS QDs under milder conditions is accomplished via a two-step growth procedure utilizing highly reactive single-source precursors [72, 73, 74]. We demonstrate increasing intraband lifetimes and PLQYs with increasing shell thickness, resulting in the highest photoluminescence efficiencies and longest intraband lifetimes reported to date at 2000 cm^{-1} (5 µm).

3.2 Synthesis of thick-shell HgSe/CdS core/shell QDs

All syntheses were performed on 4.8 ± 0.5 nm diameter HgSe QD cores to obtain intraband photoluminescence peaked near 2000 cm^{-1}, the spectral region of interest for mid-infrared photodetectors and light sources. The HgSe/CdS synthesis begins with an initial CdS growth at 80°C utilizing cadmium bis(phenyldithiocarbamate) ($Cd(PDTC)_2$), a highly reactive single-source precursor previously used for the low-temperature growth of CdSe/CdS nanobelts [75]. Through a kinetics study, we found that $Cd(PDTC)_2$ decomposes to CdS at temperatures above 60°C, and that the optimal temperature for shell growth is 80°C (See Section 3.6.10). This single-step synthesis avoids complications associated with multi-step room-temperature cALD [37, 20] and it has the added advantage of easy scalability. After growth of a 0.6 nm thick CdS layer, the QDs exhibited thermal stability (Fig. 3.6) such that thicker CdS shells could be subsequently grown using cadmium bis(diethyldithiocarbamate) ($Cd(DEDTC)_2$) at 220°C. This temperature was found to provide a good balance between minimizing interfacial core/shell alloying and promoting quasi-spherical shell growth (See Section 3.6.9) [20].

HgSe QDs display the cubic zincblende structure [35], while CdS may grow along either cubic zincblende or hexagonal wurtzite structures depending on the synthetic conditions [72].

The growth of a wurtzite shell on a zincblende core produces polypods [47, 76, 77, 78] which can promote fast nonradiative relaxation [47]. It is therefore necessary to grow the CdS shell along a zincblende structure, and we accomplish this through an appropriate choice of ligands. Growth of CdS has been previously reported to occur along a zincblende structure when cadmium carboxylates are used as ligands [79]. Indeed, during syntheses with only $Cd(DEDTC)_2$ and amine ligands, we observe a significant wurtzite shell component, and the CdS shell begins to develop tetrapodal arms (Fig. 3.9(C,D)) [74]. We find that cadmium oleate works as a good ligand to promote CdS growth along a zincblende structure (Fig. 3.9(I,K)), allowing growth of a thick and uniform shell (Fig. 3.1, Fig. 3.9(E,F)). We note that the cadmium oleate should contain no residual oleic acid, as even slight amounts lead to QDs with poor intraband photoluminescence.

Transmission electron microscopy (TEM) images indicate that the nanocrystal diameter grows from 4.8 nm to 15.3 nm during 30 minutes of CdS growth using $Cd(DEDTC)_2$ (Fig. 3.1A – D). At diameters above 12 nm, they begin growing as bullet shapes. The average diameter was measured from the TEM images as a geometric mean of the short diameters and long axis (See Section 3.8.3). The pXRD in Fig. 3.1E indicates that thick CdS shell growth occurs predominantly in a zincblende structure. Wurtzite peaks along the (100), (101) and (103) planes (at 25°, 29° and 48° respectively) are observed, which accounts for 25% of the total signal (Fig. 3.13). The absorption spectra (Fig. 3.1F) show the onset of a strong visible absorption due to the CdS shell, while the HgSe interband and intraband absorptions at 6000 cm^{-1} and 2500 cm^{-1} are retained (Fig. 3.7). This demonstrates that the integrity of the cores is maintained after the shell growth.

Under these synthetic conditions, we observe that the nanocrystal size measured by TEM is larger than predicted by the precursor amount added. We also observe a red tail in the visible absorption beyond the CdS band edge, whose intensity varies with synthetic conditions. We believe that during the initial stages of the thick-shell HgSe/CdS synthesis,

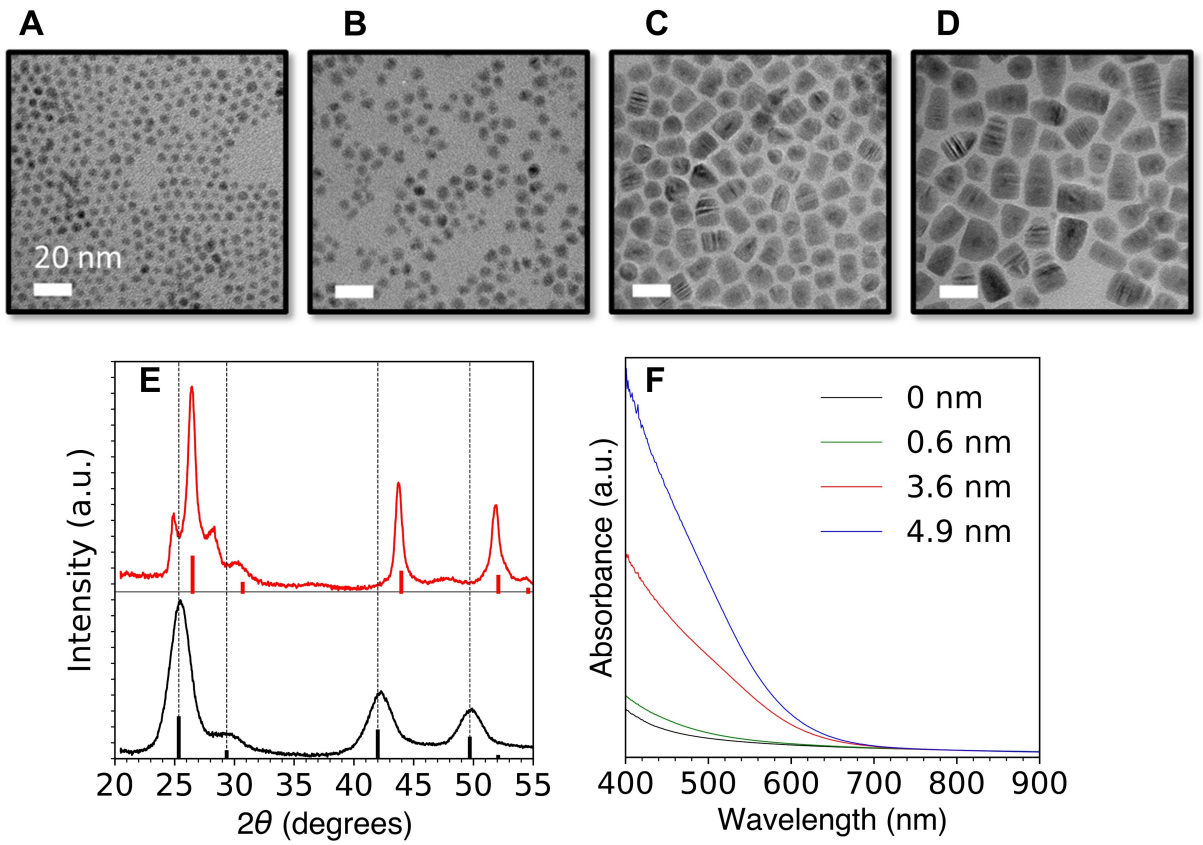

Figure 3.1: (A-D) TEM images of HgSe/CdS QDs with a core diameter of (A) (4.8 ± 0.6) nm and core/shell diameter of (B) (6.0 ± 1.2) nm, (C) (11.5 ± 1.4) nm, (D) (15.3 ± 2.7) nm. (E) powder XRD spectra of (black) 4.8 nm HgSe and (red) 19 nm HgSe/CdS QDs. Solid bars indicate the XRD peaks of bulk zincblende HgSe and CdS respectively. (F) Absorption spectra of HgSe and HgSe/CdS QDs with the indicated shell thicknesses, normalized to HgSe core absorption at 808 nm.

a fraction of the thin shell HgSe/CdS QDs dissolve and deposit upon the remaining QDs as a HgCdSSe shell. This would explain the red tail and larger core/shell sizes than calculated from the amounts of precursors added. A batch-to-batch variability is observed in the extent of dissolution, and it also depends on the heating rate. The benefit, however, is the promotion of compact thick shell growth. We attribute this to reduced strain at the core/shell interface, with a possible gradient-alloying. We observe no noticeable effect on the intraband and interband absorptions (see Section 3.8.1 for more details).

3.3 Measurement and chemical control of $1S_e$ occupancy

Although HgSe QDs are n-type under ambient conditions with electrons in $1S_e$ [1, 70], CdS shell growth tends to remove the natural doping. One must therefore n-dope the HgSe/CdS QDs after synthesis to turn on the $1S_e$ – $1P_e$ intraband transition. Several methods are commonly employed to dope QDs including incorporation of aliovalent impurities [80, 81, 82], surface oxidation [83, 84], changing surface dipole through ligand exchange [35, 85, 86], charge injection through electrochemistry [87, 88, 89, 90, 91, 92] or redox agents [93, 94, 95]. Here we employ a surface dipole modification which, as depicted in Fig. 3.2A, shifts the absolute positions of the QD energy levels relative to a fixed environmental Fermi level. We denote the QDs with 0, 1 and 2 electrons in the $1S_e$ state as $1S_e(0)$, $1S_e(1)$ and $1S_e(2)$ respectively. Since the $1S_e$ occupancy (doping) affects absorption and photoluminescence, it is necessary to control and characterize the doping.

The doping of HgSe/CdS QDs after synthesis is sensitive to the quantities of cadmium oleate ligand and CdS precursor utilized during the shell growth. Cadmium oleate promotes n-doping, attributed to the introduction of a positive surface species and inward-pointing surface dipole (Fig. 3.2A-B). The $Cd(DEDTC)_2$ precursor evolves H_2S during the reaction [73, 96] and likely deposits S^{2-} on the QD surface, which reduces the n-doping. To control the doping, we developed a procedure in which we first oxidize the HgSe/CdS QDs by treatment with ammonium sulfide at 40°C to achieve a $1S_e$ occupancy (N_e) of $\sim$0 (See Section 3.6.8). The QDs are subsequently treated with cadmium acetate at 180°C, and the doping level can be tuned by changing the cadmium acetate amount (Fig. 3.2D). At low dopings, the intraband absorption is shadowed by the surface ligand absorption (Fig. 3.11(D)). To obtain quantitative optical measurement of the doping, we used a solution of molecular iodine in TCE as a temporary oxidizing agent that does not change the ligand absorption [97]. A subtractive procedure then eliminated the ligand absorption, giving a

clean intraband absorption required for optical doping determination (Fig. 3.11). The interband and intraband absorptions are linearly related as would be expected from a transfer of oscillator strength, as shown in Fig. 3.2C (see Fig. 3.19 for comparison of oscillator strengths). From a linear fit to the intraband – interband trend, we determine the N_e of any QD sample from the ratio of the intraband peak absorbance to the y-intercept.

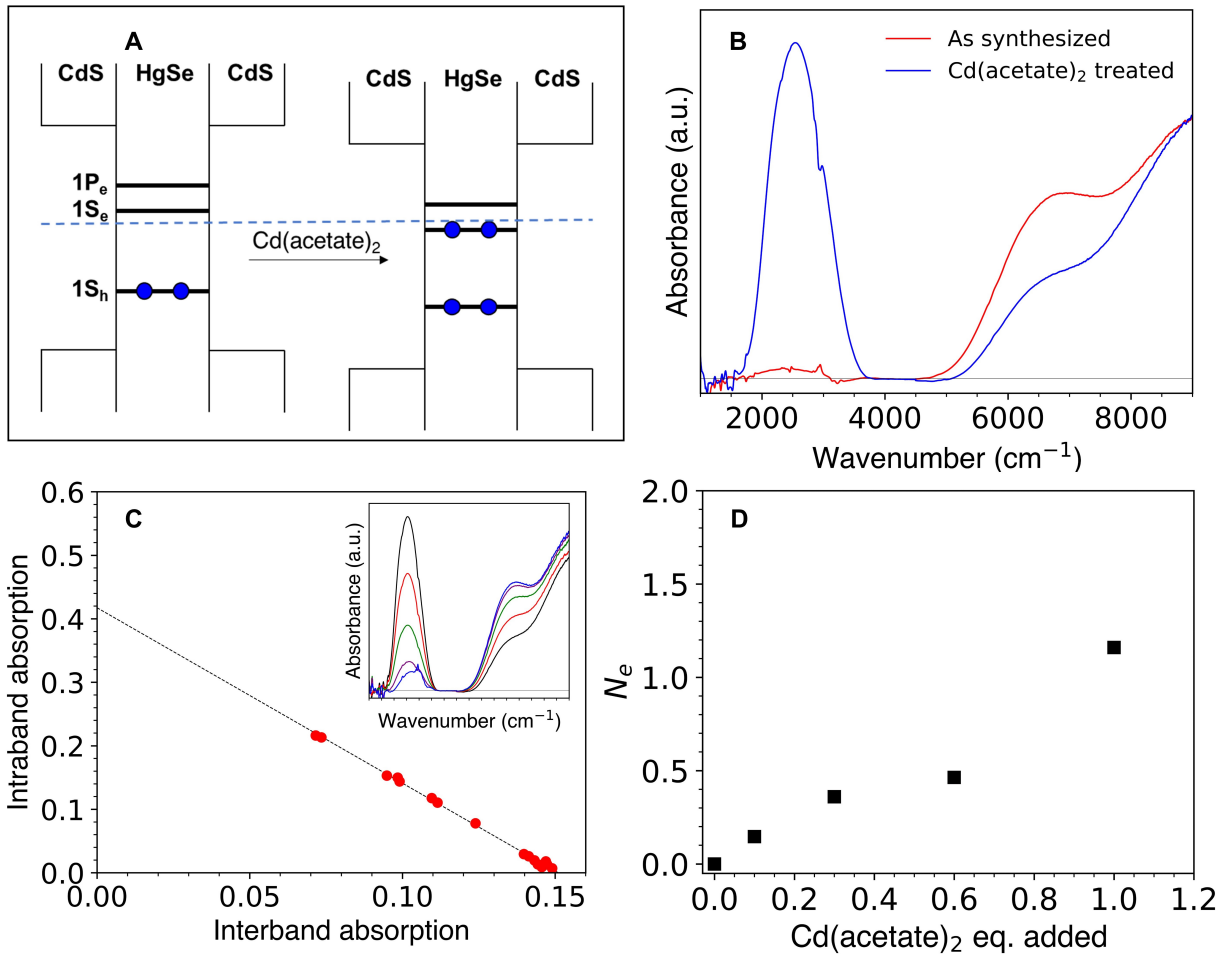

Figure 3.2: Control of the $1S_e$ occupancy (N_e) of HgSe/CdS QDs. (A) Cartoon of surface dipole n-doping mechanism in HgSe/CdS QDs. The ambient Fermi level is indicated by the dashed blue line. (B) FTIR spectra of HgSe/CdS QDs (red) after synthesis, and (blue) after treatment with cadmium acetate. Absorptions from the ligands are subtracted for clarity. (C) Plot of intraband vs interband absorption of HgSe/CdS QDs with different doping levels. Inset shows the FTIR spectra (after subtraction of ligand absorption) of HgSe/CdS QDs after titrating with I_2. (D) Average $1S_e$ occupancy (N_e) as function of the surface equivalents of cadmium acetate added (see Section 3.6.8).

3.4 Photoluminescence and nonradiative relaxation

Photoluminescence spectra of the QDs were recorded in solution by excitation with an 808 nm laser. Photoexcitation of $1S_e(0)$ QDs can only lead to interband emission. On the other hand, photoexcitation of the $1S_e(1)$ and $1S_e(2)$ HgSe/CdS QDs can lead to formation of a hole in either the valence band or the conduction band. Due to fast hole cooling, likely by hole Auger cooling [56] in n-doped HgSe QDs, the hole relaxes to the $1S_e$ state within a few picoseconds [1]. This leads to only intraband emission in n-doped $1S_e(1)$ and $1S_e(2)$ QDs, irrespective of whether the photoexcitation is from the valence or conduction band (Kasha's rule) [98].

As shown in Fig. 3.3, the absorption and photoluminescence (PL) spectral peaks of HgSe/CdS QDs show a negligible redshift compared to HgSe QDs, supporting the strong type-I core/shell band alignment. The PL quantum efficiencies (PLQE), defined here as the global fraction of interband or intraband photons emitted per photon absorbed, do not directly inform on the nonradiative relaxation because they depend on the doping level. We therefore determine the contributions from $1S_e(0)$, $1S_e(1)$ and $1S_e(2)$ populations to the PLQE, and normalize by the relative populations to determine the absolute PL quantum yields (PLQYs) of the three species. The interband emission is expected to primarily arise from $1S_e(0)$ QDs as noted earlier, while to a first approximation the intraband emission should be proportional to the sum of $1S_e(1)$ and $1S_e(2)$ populations.

Intraband and interband PLQE data at different ensemble N_e are shown for 4.8 nm diameter HgSe (Fig. 3.4A) and for similar HgSe with 3.4 nm CdS shell thickness (Fig. 3.4B). N_e at a fixed Fermi level is determined by Fermi-Dirac statistics, while the fraction of QDs with 0, 1 or 2 electrons in the $1S_e$ state is expected to follow a binomial distribution if there is no significant electronic correlation (See Section 3.8.4). The interband emissions in Fig. 3.4 are well-fit by the $1S_e(0)$ occupancy, which is consistent with Kasha's rule. The

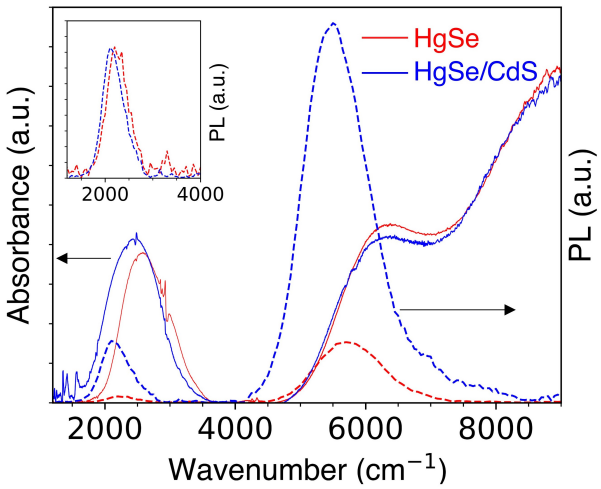

Figure 3.3: Absorption (solid lines) and PL (dashed lines) spectra of (red) (4.8 ± 0.6) nm HgSe and (blue) (10.2 ± 1.6) nm HgSe/CdS with $N_e = 0.5$. The ligand absorptions have been subtracted for clarity. The inset shows a comparison of intraband PL spectra with the HgSe PL scaled 10×.

fitting gives interband PLQYs of $(9.5 \pm 1.0) \times 10^{-3}$ and $(3.6 \pm 0.1) \times 10^{-2}$ for HgSe and HgSe/CdS respectively. Likewise, the intraband PLQE for HgSe fits well to a sum of $1S_e(1)$ and $1S_e(2)$ populations with a PLQY of $(3.8 \pm 0.5) \times 10^{-4}$ for both species.

In contrast, the intraband PLQE of HgSe/CdS cannot be fit as well by assuming a constant intraband PLQY (Fig. 3.4B, dashed blue). The decreasing intraband PLQY of HgSe/CdS with the doping (Fig. 3.4B, inset) suggests the presence of a nonradiative pathway that changes with the doping. This interpretation is qualitatively supported by PL lifetime measurements on HgSe/CdS QDs which show a faster intraband decay at higher doping levels (Fig. 3.14). One possible mechanism is the presence of defect states in the CdS shell close to the $1S_e$ of HgSe which would be occupied upon surface dipole-induced energy level shifting (Fig. 3.2A). Indeed, bulk CdS is known to exhibit deep electronic defect states which can be infrared active [2, 3, 99]. The filling of these defect states could introduce a nonradiative pathway either by hole-trapping or resonant energy transfer (Fig. 3.20).

To minimize the doping-dependent nonradiative effects and investigate the underlying relaxation mechanisms, we further examined the influence of CdS shell thickness for QDs

with $N_e < 0.2$. These data are shown in Fig. 3.5. Growth of a thick shell leads to a weak increase in the interband PLQY, with the exception of the thin shell HgSe/CdS QDs (Fig. 3.5A, 0.6 nm shell thickness). These QDs display a relatively poor interband PLQY of 0.5% due to the low temperature shell synthesis, which increases to >2% on annealing at 220°C (Fig. 3.6(B)). The weak increase of interband PLQY with shell thickness is qualitatively similar to prior works which reported saturation of interband HgSe/CdS PLQY at moderate shell thicknesses [37, 20]. In contrast, the intraband PLQY exhibits a 30-fold increase over the same shell thickness range (Fig. 3.5A).

The intraband radiative lifetime τ_R of HgSe QDs can be calculated from Eq. 2.1 [100, 101, 102, 103] where p is the transition dipole moment, ω is the angular frequency, ϵ_0 is the vacuum permittivity, and ϵ_1 and ϵ_2 are respectively the real optical dielectric constants of the nanoparticle and the solvent:

$$\frac{1}{\tau_R} = \frac{\omega^3 p^2}{3\pi\epsilon_0\hbar c^3} \times \sqrt{\epsilon_2}\left(\frac{3\epsilon_2}{\epsilon_1 + 2\epsilon_2}\right)^2 \tag{3.1}$$

Due to the strong type-I core/shell band alignment, the emission frequency and transition dipole do not change upon shell growth (Fig. 3.3). Using material parameters discussed in Section 3.8.2, the intraband radiative lifetime τ_R for HgSe QDs emitting at 2050 cm^{-1} (5 microns) is calculated to be 900 ± 300 ns. Growth of a CdS shell changes the dielectric screening, leading to a radiative lifetime of 700 ± 160 ns for thick shell HgSe/CdS QDs. The PLQY is given by

$$PLQY = \frac{\tau_R^{-1}}{\tau_R^{-1} + \tau_{NR}^{-1}} \tag{3.2}$$

and the total nonradiative rates τ_{NR}^{-1} calculated from the measured PLQY are then

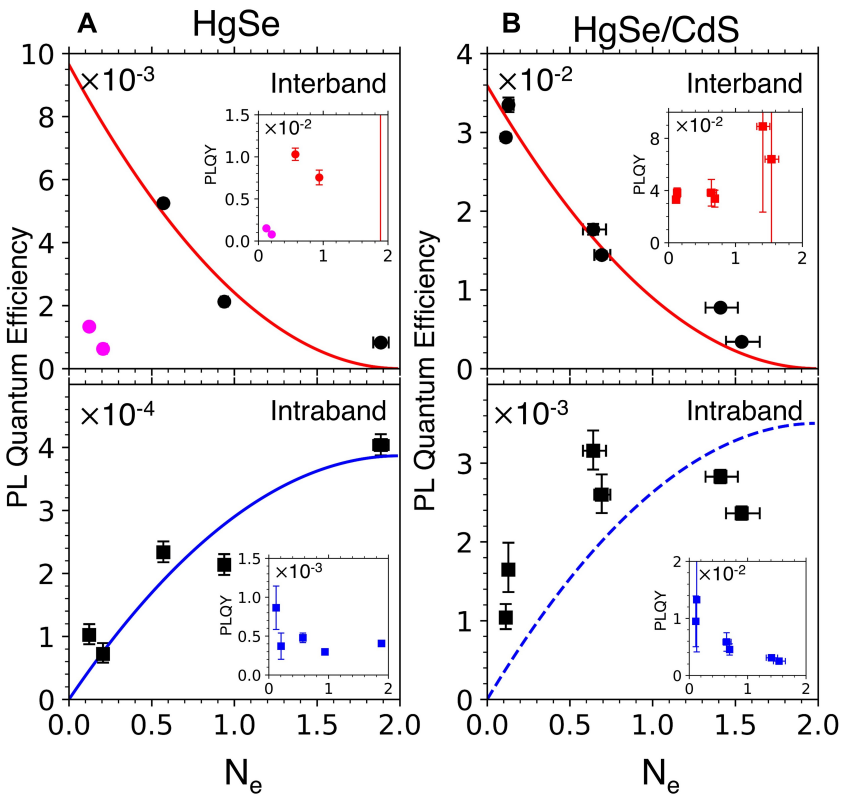

Figure 3.4: PLQE vs N_e for (A) (4.8 ± 0.6) nm HgSe QDs and (B) (11.6 ± 1.6) nm HgSe/CdS QDs. The red curves are fits from the $1S_e(0)$ binomial population. The two samples (pink points) with the lowest dopings for HgSe in (A) have a low interband PL due to the poor surface passivation, and are excluded from the fit. The blue curve in (A) is fit assuming same PLQYs for $1S_e(1)$ and $1S_e(2)$ populations. The data in (B) fits poorly to a constant PLQY (dashed blue). The insets show the PLQY calculated by normalizing the PLQE to $1S_e(0)$ population (for interband) and sum of $1S_e(1)$ and $1S_e(2)$ populations (for intraband).

expected to vary from 700 ps in the HgSe core to 15 ns in HgSe/CdS with 15 nm diameter (See Section 3.8.2). This increasing trend is clearly supported by transient PL measurements, although they exhibit multiexponential behavior, as shown in Fig. 3.5B. The lifetime data for the HgSe cores are similar to those reported previously [1], with two relaxation times of 26 ± 1 ps and 1030 ± 35 ps. About 90% of the time-integrated PL comes from the 1030 ps decay, and the overall transient behavior is consistent with typical PLQYs of the HgSe cores. Shell growth leads to a 25-fold lengthening of the fast lifetime component, while the expected lengthening of the slow lifetime component is not resolved on the timescale of these

measurements. Overall, the PL data indicate that thick CdS shells substantially lengthen average intraband nonradiative lifetimes into the nanosecond regime.

The intraband lifetime derived from the PLQY is at least an order of magnitude longer than the ∼1 ns phonon-mediated lifetime limit predicted by semiclassical simulations [24]. The near-field energy transfer mechanism [30, 22] predicts that the non-radiative rate should scale with the total nanocrystal radius R as R^{-4}, while phonon-mediated relaxation should be independent of shell thickness and relaxation associated with surface anharmonicity should be strongly reduced even at small type-I shell thicknesses. The data of Fig. 3.5A suggest that energy transfer remains the dominant nonradiative mechanism, and that anharmonicity or intrinsic phonon effects are relatively small. The PLQY trend with shell thickness in HgSe/CdS displays a fair agreement with a generic quartic fit, shown in Fig. 3.5A, and the deviations at thicker shells are possibly due to irregular shell growth or strain defects. While the rate of surface trapping should be slow at the shell thicknesses considered here due to the exponential dependence on the tunneling barrier, it is possible that stacking faults arising from lattice strain can allow the carriers to reach the surface [104]. We empirically observe that the intraband PLQY is relatively insensitive to the surface ligand coverage, suggesting that surface trapping is not significant, but we cannot rule out a trapping mechanism with the current data.

It is generally reported that the interband emission of thick shell CdSe/CdS is dimmer than for intermediate shells, possibly due to defects in the thick CdS shell. It is known that bulk crystalline CdS are photoresponsive in the near- and shortwave-infrared via absorption associated with deep traps [2, 3], and the photoresponse can depend sensitively on the CdS growth conditions [99]. Such traps in CdS might also have a negative impact on the photoluminescence quantum yields of both interband and intraband transitions of the HgSe core. For example, electron trapping by states in the shell could prevent bright interband and intraband emission (Fig. 3.20). Further progress in intraband emission will likely benefit

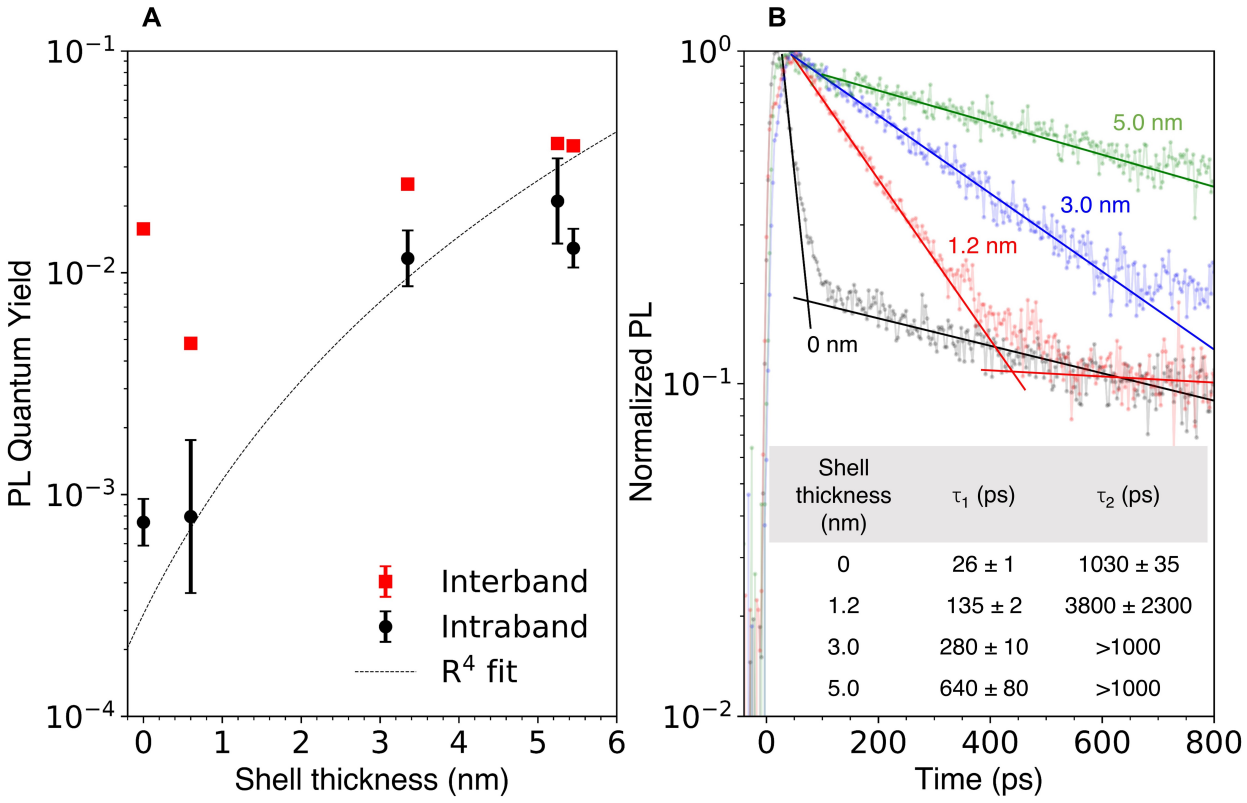

Figure 3.5: (A) (red squares) $1S_e(0)$ interband and (black circles) $1S_e(1)$ intraband PLQY of HgSe/CdS QDs with different shell thicknesses. Except the cores (with $N_e \sim 1$), all samples had $N_e < 0.2$. The intraband PLQY data are fit to an R^4 function (black dotted line), physically motivated by the expected trend from Forster-type nonradiative relaxation to surface vibrations. (B) Intraband PL lifetime traces for HgSe ($N_e \sim 2$) and HgSe/CdS QDs ($N_e < 0.5$). All traces fit well to biexponentials, while the long lifetimes for the thickest samples are too long to determine.

from improved shell growth or a focus on shell materials that are defect-free.

The 2 ± 1% intraband PLQY achieved with thick-shell HgSe/CdS QDs makes them the brightest reported solution-phase chromophores in the 2000 cm^{-1} (5 microns) region at room temperature. This PLQY is also close to the room-temperature record of ∼4% observed in epitaxial III-V superlattices [105, 106]. The ability to engineer QDs with slow nonradiative relaxation is important for mid-infrared photodetectors, where background noise is fundamentally limited by the nonradiative relaxation of thermal carriers [19]. Long lifetimes and high quantum yields should also support mid-infrared emission or lasing by enabling longer

gain lifetimes, lower oscillation thresholds, and smaller saturation intensities [107]. Our results indicate that decoupling the QD excitation from the infrared absorbing environment remains crucial for achieving long intraband lifetimes.

3.5 Conclusions

Infrared nonradiative decay is ubiquitous in solution phase chromophores and inorganic colloidal quantum dots provide an avenue towards brighter emitters. Here we focused on the intraband chromophores provided by n-doped HgSe quantum dots emitting at 5 microns. To obtain brighter photoluminescence and test the fundamental limitations imposed by phonon relaxation, we synthesized thick CdS shells on HgSe QDs. Control of the CdS growth in the zincblende crystal structure allows formation of compact shells up to thicknesses exceeding 7 nm, with total nanocrystal sizes approaching 20 nm. Although the doping disappears upon shell growth, we developed a procedure to regain and control the doping by a post-synthetic treatment with cadmium acetate. The photoluminescence quantum yields were then studied as functions of doping and shell thickness. At low n-doping levels, the HgSe/CdS QDs display the highest intraband PL quantum yields, up to 2% for the thickest shells, corresponding to intraband nonradiative lifetimes estimated in excess of 10 ns. Such lifetimes suggest that phonon-mediated relaxation is at least an order of magnitude slower than predicted by semiclassical electron-phonon relaxation calculations [23, 24]. The quantum yields reported in this study are the largest of all colloidal nanomaterials, interband or intraband, at 5 microns.

3.6 Syntheses and surface modifications

3.6.1 Chemicals

Ammonium hydroxide (NH_4OH, 28-30% in water), carbon disulfide (CS_2, 99.9%), cadmium chloride ($CdCl_2$, 99.99%), cadmium oxide (CdO, 99.9%), oleic acid (90%), cadmium nitrate tetrahydrate (99.997%), 1-dodecanethiol (DDT, 98%), oleylamine (OAm, 70%), hexadecane (99%), dodecylamine (98%), hexadecylamine (90%), 1-octadecene (ODE, 90%), cadmium acetate hydrate ($Cd(OAc)_2$, 99.99%), iodine (I_2, 99.99%), tetrachloroethylene (TCE, 99%) and ammonium sulfide ($(NH_4)_2S$, 40-40% in water) were purchased from Sigma-Aldrich. Mercury (II) chloride ($HgCl_2$, 99.999%), aniline (99%), didodecyldimethylammonium bromide (DDAB, 98%) and formamide (FA, 99%) were purchased from Alfa Aesar. Isopropanol (IPA, 99.9%) was purchased from Fisher, methyl acetate (99%) was purchased from Acros Organics, cadmium bis(diethyldithiocarbamate) ($Cd(DEDTC)_2$) (96%) was purchased from Gelest, and bis(trimethylsilyl)selenide (TMSSe) was purchased from Wonik Materials North America. All chemicals were used without further purification.

3.6.2 Precursors and stock solutions

Synthesis of $Cd(PDTC)_2$: Cadmium bis(phenyldithiocarbamate) was synthesized following reported literature with minor changes [108, 75]. For synthesis of the precursor ammonium phenyldithiocarbamate (NH_4PDTC) [108], 50 mL NH_4OH, 50 mL acetone and 20.1 mL aniline (220 mmol) were added to a 3-neck flask under nitrogen bubbling at room temperature. 13.3 mL CS_2 (220 mmol) was added dropwise with vigorous stirring. The solution developed a red color after 5 minutes, and a pale-yellow crystalline product slowly crystallized and precipitated over the next 90 minutes. The product was collected by vacuum filtration and washed with 120 mL cold ethanol. The NH_4PDTC was dried under vacuum for 3 hours and stored in a freezer to prevent decomposition. 11.2 g of product was obtained.

For synthesis of $Cd(PDTC)_2$ [75], 1.25 g NH_4PDTC was dissolved in 100 mL water in an Erlenmeyer flask. The solution was partially cloudy. 615 mg $CdCl_2$ was dissolved in 80 mL water and added dropwise to the flask over 30 minutes, leading to immediate precipitation of $Cd(PDTC)_2$ as a pale yellow powder. The product was collected by vacuum filtration, and washed with 25 mL cold ethanol. The precipitate was ground with a mortar and pestle, dried under a Schlenk line and stored in a dessicator.

Synthesis of $Cd(oleate)_2$: Cadmium oleate was synthesized using a reported procedure [109]. It was necessary to ensure that the cadmium oleate contained no free oleic acid (as characterized by FTIR), as this resulted in QDs with poor intraband PLQY.

Synthesis of $Cd(DDT)_2$: Cadmium dodecanethiolate was synthesized adapting reported literature [110]. 1.55 g of cadmium nitrate (5 mmol) was dissolved in 25 ml methanol. In an Erlenmeyer flask, 12 mL triethylamine, 12 mL methanol and 2.01 g dodecanethiol were added. The cadmium nitrate solution was added to the flask dropwise with stirring to obtain a white precipitate. The product was collected by vacuum filtration, and washed three times with methanol. The precipitate was ground with a mortar and pestle, dried in a Schlenk line vacuum, and then stored under ambient conditions.

$Cd(PDTC)_2$ solution: A 0.1M solution of cadmium bis(phenyldithiocarbamate) in 20% OAm-hexadecane was prepared by adding 134mg (0.3mmol) of $Cd(PDTC)_2$ to 0.6mL oleylamine and 2.4mL hexadecane. The mixture was vortexed for 15 minutes at room temperature to dissolve. Saturated amine solution: Prepared by mixing a 2:2:1 mass ratio of hexadecane-dodecylamine-hexadecylamine. The mixture was designed from the report by X Peng and coworkers [72], but using longer chain molecules to increase the boiling point. The mixture was solid at room temperature, and had to be melted by warming to $\sim$40°C before use. 20% oleylamine-hexadecane solution: 2 mL of oleylamine was mixed with 8 mL hexadecane.

Cadmium oleate solution: A 0.024M solution was prepared by adding 162mg (0.24mmol)

of $Cd(oleate)_2$ to 10mL of saturated amine solution. The solution was vortexed at room temperature till the $Cd(oleate)_2$ fully dissolved.

Cadmium dodecanethiolate solution: A 0.024M solution was prepared by adding 123mg (0.24mmol) of $Cd(DDT)_2$ to 10mL of saturated amine solution. The solution was heated in air to ∼100°C till the $Cd(DDT)_2$ fully dissolved. The reagent formed a fine gel-like precipitate on cooling, but the precipitated powder was small enough to measure the reagent quantitatively.

$Cd(DEDTC)_2$ precursor solution: A 0.02M CdS precursor solution was prepared by adding 2mL of 0.024M $Cd(oleate)_2$ solution (or $Cd(DDT)_2$ solution) to 10mL of 0.024M cadmium bis(diethyldithiocarbamate) solution (98mg $Cd(DEDTC)_2$ in 10mL saturated amine solution). The mixture was sonicated at room temperature to dissolve, and was warmed to ∼40°C before loading to a syringe pump.

$Cd(acetate)_2$ doping solution: A 0.05M solution of cadmium acetate was prepared by adding 13mg (0.05mmol) cadmium acetate dihydrate to 0.9mL hexadecane and 0.1mL oleylamine in a test tube. The mixture was heated in air to around ∼100°C to dissolve the cadmium acetate. The solution formed a gel on cooling, but it could be dissolved on gentle warming. I_2 solution for doping modification: A 0.02M solution of I_2 in TCE was prepared by adding 10mg I_2 to 2mL TCE and sonicating for 15 mins in a glass vial. A 0.004M solution was prepared by adding 0.4mL of this solution to 1.6mL TCE in another vial.

3.6.3 HgSe core QD synthesis

HgSe core QDs were synthesized following the procedure by Melnychuk et. al [1]. Briefly, 108mg of $HgCl_2$ was added to a 3-neck flask with 10mL oleylamine. The flask was equipped with a stir bar, rubber sleeve stoppers with a thermocouple attached, and connected to a Schlenk line manifold. Three vacuum (p∼1 torr) – Argon flush cycles were performed at room temperature, and the flask was heated at 100°C for 45 minutes. The temperature was

then set to 900C. A TMSSe solution (50μL in 0.95mL oleylamine) was prepared in a N_2-purged glovebox and injected swiftly into the flask. The temperature dropped to 88°C and was kept at this temperature for 2 minutes. The flask was then cooled to room temperature using compressed air, and 10mL octane was added.

Purification of the QDs was done in air. On cooling, the solution was centrifuged to obtain the excess unreacted Hg- complex as a grey pellet. The supernatant containing the HgSe QDs was collected and precipitated by addition of ethanol, and centrifuged. The precipitate was dispersed in 0.1mL oleylamine and 4mL TCE. The solution might appear foamy at this stage due to presence of excess Hg^{2+} species in solution. A second purification was done by addition of 0.8mL of 0.1M DDAB/TCE and precipitated with IPA. After centrifugation, the precipitate was dispersed in 0.1mL oleylamine and 2mL TCE and stored as a stock solution in the freezer. Concentration of the HgSe stock solution was determined by measuring the absorbance at 700 nm using the cross-section of HgSe as 3.5×10^{-18} cm^2 per Hg atom (calculated from the reported cross-section at 415 nm [1] and the measured HgSe absorption spectrum). Around 30mg of HgSe QDs were obtained from the reaction, giving a yield of $\sim$50% with respect to the Selenium added.

3.6.4 Thin shell HgSe/CdS QD synthesis by cALD

HgSe/CdS QDs were synthesized by cALD adapting the work by Shen et. al [20] with notable changes. The reaction was done in a scintillation vial heated at 50-55°C, since this helped prevent the formation of an emulsion. No difference was observed between syntheses in air or in glovebox, so the reaction was done in air. The reaction was performed in dark to prevent photo-oxidation of sulfide to sulfates.

The $(NH_4)_2S$ stock solution was prepared by adding 1 mL of ammonium sulfide solution (40% in water) to 4 mL of formamide (FA) in the glovebox in a scintillation vial. The vial was capped with a rubber stopper and brought to the fume hood.

15mg of purified HgSe QDs was added to a scintillation vial with 4 mL of TCE, 0.4 mL OAm and equipped with a stir bar. 4 mL of formamide (FA) was added, and the vial was heated to 50-55°C with gentle stirring for 10 mins. The FA layer was discarded (to remove residual Hg^{2+}). For the first Cd layer, 4 mL FA was added with 30 mg cadmium acetate, and stirred at 50-55°C for 10 mins. The FA layer was then discarded, 4 mL FA was added and stirred for 2 mins. The FA layer was discarded to remove excess Cd^{2+} and the washing was performed a second time. The washings are an essential part of the procedure to prevent independent nucleation of CdS.

For the first S- layer, 4 mL FA was added, and 0.5 mL of the $(NH_4)_2S$ stock solution was added dropwise. The vial was stirred at 50-55°C for 2 mins. The FA layer was then discarded, 4 mL FA was added and stirred for 2 mins, and then discarded. The washing was done for a second time. Three more Cd- and S- layers were similarly performed using 32 mg, 35 mg and 40 mg cadmium acetate respectively, and 0.5 mL $(NH_4)_2S$ stock solution. A fifth Cd- layer using 45 mg cadmium acetate was performed to n-dope the QDs. The stirring was done gently to avoid formation of an emulsion. If an emulsion was formed, few drops of isopropanol (IPA) were added to aid in the separation of the layers.

After the synthesis of the thin CdS shell, the QDs were purified twice by precipitation – dispersion using IPA and TCE. It is important to note that the cALD reaction is sensitive to the stirring speed. Excessive stirring leads to formation of an emulsion and incomplete removal of excess Cd^{2+} and S^{2-}, leading to independent nucleation of CdS.

3.6.5 Thin shell HgSe/CdS QD synthesis using Cd(PDTC)$_2$

Unless otherwise noted, all syntheses of thin shell HgSe/CdS QDs were performed using this method. Cadmium bis(phenyldithiocarbamate) ($Cd(PDTC)_2$) was used as highly reactive single-source precursor for deposition of a thin shell on HgSe at low temperatures, motivated by the work by Buhro and coworkers [75].

30mg of purified HgSe core QDs was added to a 3-neck flask, and 15mL of a 20% oleylamine – hexadecane solution was added. Three vacuum (p $\sim$ 1 torr) – argon evacuation cycles were performed at room temperature. The temperature was then set to 80°C. When the temperature reached 40°C, 1.17mL of 0.1M $Cd(PDTC)_2$ solution (2 monolayers (ML) of CdS) was injected. The solution was kept at 80°C for 5 minutes. The flask was then cooled to 50°C and 0.82mL of 0.1M $Cd(PDTC)_2$ solution (1 ML of CdS) was injected, and the solution was heated at 80°C for 5 minutes. The flask was then connected to vacuum at 80°C to remove the H_2S formed during the shell growth. When the pressure dropped below 1 torr, the flask was returned to Argon and cooled to room temperature.

The HgSe/CdS QDs showed more colloidal stability than the HgSe cores, and did not require the addition of DDAB during precipitations. The HgSe/CdS QDs were purified in air by precipitation using methyl acetate. Some oily residue was observed after synthesis which is difficult to remove using precipitation / dissolution. 2 mL TCE was added to the black precipitate, and the solution was stored as a stock solution in a vial in the freezer. TEM imaging showed that the QD diameter increased from 4.8 nm to 6.1 nm after the shell growth. No homogeneous nucleation was observed at the above reaction conditions, though homogeneous nucleation was seen when the $Cd(PDTC)_2$ precursor volume was doubled.

The concentration of the QDs was determined using the absorbance at 700nm using the cross-section of HgSe, under the assumption that the shell growth leads to negligible change in absorbance at this wavelength.

3.6.6 Testing the thermal stability of thin shell HgSe/CdS QDs

Prior to the thick CdS shell synthesis, the thin shell HgSe/CdS QDs were annealed in solution to test for thermal stability. Thin shell HgSe/CdS QDs (containing 3 mg of HgSe cores) was purified by precipitation with methyl acetate. 1.5 mL of saturated amine solution was used to dissolve the QDs, and transferred to a 3-neck flask. 8.2mg $Cd(oleate)_2$ (1.5 surface

equivalents) was then added. Three vacuum-Ar cycles were performed, and the solution was heated and kept at 220°C for a desired duration. The solution was cooled to room temperature and precipitated with methyl acetate. The pellet was dispersed in 0.9mL of TCE and 0.1mL oleylamine. The solution was heated to boil (∼110°C - 120°C) for a few seconds to dissolve the saturated amines and passivate the QDs with oleylamine. After cooling to room temperature, the solution was purified twice by precipitation-dispersion using methyl acetate and TCE. The pellet after the second precipitation was dried under vacuum before dispersing in TCE for FTIR measurements. Apart from an increase in the n-doping, no observable change was seen in the thin HgSe/CdS QDs after annealing at 220°C (Fig. 3.6).

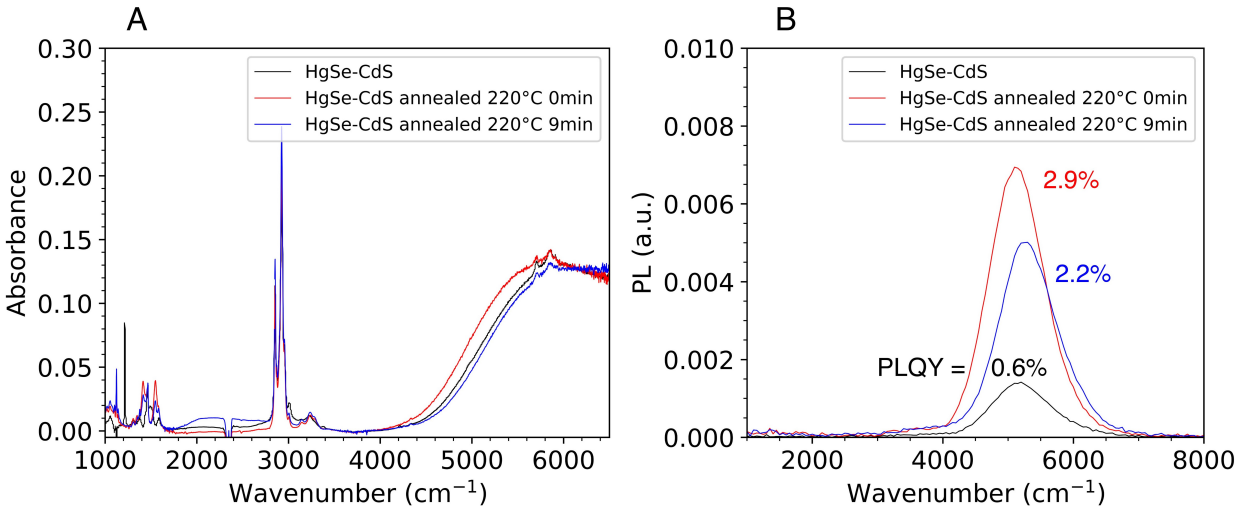

Figure 3.6: (A) Absorption spectra of thin shell HgSe/CdS QDs (diameter = 6.1 nm) before and after annealing in solution at 220°C with cadmium oleate. A small increase in the doping is observed due to the presence of cadmium oleate in solution, but the optical spectra are nearly unchanged, demonstrating the thermal stability of the thin shell HgSe/CdS QDs. (B) PL spectra of thin shell HgSe/CdS QDs before and after annealing at 220°C. Due to the low-temperature synthesis of the thin shell, the interband PLQY is relatively low at 0.6% (black), but rises to ∼2-3% on annealing (red and blue). The intraband PL is too weak to be resolved at this scale.

3.6.7 Thick shell HgSe/CdS QD synthesis

A thick CdS shell was overgrown on the thin shell HgSe/CdS QDs using $Cd(DEDTC)_2$ as a single-source precursor, with amines and $Cd(oleate)_2$ as ligands. The $Cd(oleate)_2$ helped prevent the growth of wurtzite arms during shell growth [74, 111], The concentration of $Cd(oleate)_2$ is crucial, as the sulfur-containing side products from decomposition of $Cd(DEDTC)_2$ reacted with excess $Cd(oleate)_2$ and led to undesired homogeneous nucleation of CdS. We found that a 1:5 molar ratio of $Cd(oleate)_2$: $Cd(DEDTC)_2$ provided a balance to prevent growth of wurtzite arms, while avoiding homogeneous nucleation. Cadmium dodecanethiolate ($Cd(DDT)_2$) was observed to give similar results as cadmium oleate when used as the ligand.

The synthesis was done in the absence of unsaturated solvents, as they led to the formation of a thick oil /gel after synthesis which was difficult to separate from the QDs. We hence employed a 2:2:1 mixture of hexadecane-dodecylamine-hexadecylamine as the solvent, where the mixture aided in entropic dispersion of the QDs [112].

Thin shell HgSe/CdS QDs (containing 8mg of HgSe cores) was precipitated with methyl acetate to remove leftover oleylamine. The pellet was dispersed in 4mL of warmed saturated amine solution, and 1.35mL of 0.024M $Cd(oleate)_2$ solution (1.5 surface equivalents) was added. The mixture was added to a three-neck flask equipped with rubber sleeves and a thermocouple, and connected to a Schlenk line. The 0.02M $Cd(DEDTC)_2$ precursor solution was kept in a plastic syringe connected to a syringe pump. Three vacuum ($p \sim 1$ torr) - Argon cycles were performed, and the solution was heated rapidly to 220°C (average heating rate is around 50°C/min). When the temperature reached 215°C, the precursor solution was injected at rate 0.396 mL/min for 10 mins (equivalent to 3MLs of CdS). The temperature was maintained at 220°C and was not let to exceed 225°C. The flask developed a yellow tinge after a few minutes, indicating the growth of CdS. Depending on the reaction scale and heating rate, a reddish tinge might be observed, indicating dissolution of a fraction of

the QDs and deposition of a HgCdSSe shell on the larger QDs.

After 10 mins, the injection was stopped and the syringe was removed. The solution was cooled to 120°C and evacuated to remove the H_2S formed during the reaction. Removal of the H_2S was necessary to prevent CdS homogeneous nucleation during post-synthetic n-doping or during further CdS shell growth. For a further growth of 3MLs of CdS, the flask was heated to 220°C and 0.02M CdS precursor injection was resumed at 0.650 mL/min for 10 mins (equivalent to 3MLs of CdS). The solution becomes cloudy with time as the dots grow larger. After the injection is complete, the flask was then cooled to 120°C and evacuated. The solution was then cooled to room temperature.

All purifications were done in air. On centrifuging the cooled reaction mixture, the nanocrystals typically precipitated as a thick bulky precipitate. Remaining QDs in the solution were precipitated using methyl acetate and centrifuged. After decanting the supernatant, the precipitate was dispersed in ∼4mL TCE and 0.4mL OAm was added. The solution was brought to a boil (∼110°C - 120°C) for a few seconds to dissolve the saturated amine solvent, and let to cool. The solution was then purified twice by precipitation with methyl acetate and dispersion in TCE. After the second precipitation, the pellet was dried under vacuum, and then dispersed in TCE for measurements.

The shape of the thick shell HgSe/CdS QDs was sensitive to the reaction scale, where a 4 mg reaction scale led to more compact QDs than an 8 mg scale.

3.6.8 Doping control in HgSe/CdS QDs

The as-synthesized HgSe/CdS QDs typically showed a partial n-doping, as seen by the prominent $1S_h$ – $1S_e$ interband absorption and small $1S_e$ – $1P_e$ intraband absorption. To achieve doping control, we first completely undoped the QDs by performing a cALD with $(NH_4)_2S$, and then treated with cadmium acetate to achieve the desired n-doping level [85]. Reaction of cadmium acetate with thick shell HgSe/CdS QDs at room temperature led to

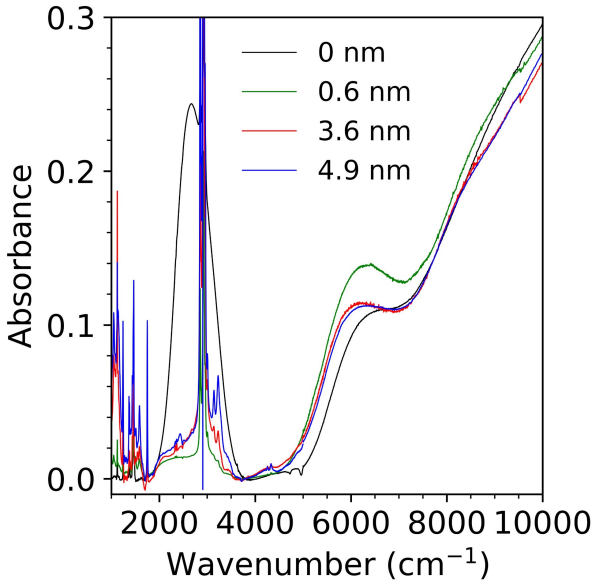

Figure 3.7: FTIR absorption spectra of HgSe QDs and HgSe/CdS QDs with different shell thicknesses (corresponding to samples in Figure 3.1F in the main text). Negligible shifts in the intraband and interband absorptions of HgSe confirms that the integrity of the core is preserved after the thick shell growth. The data is obtained by stitching spectra using an FTIR spectrometer (<5000 cm^{-1}) and a dispersive NIR spectrophotometer (>5000 cm^{-1}).

incomplete n-doping, and it was necessary to perform the surface treatment at an elevated temperature to ensure a complete reaction.

The undoping was performed adapting a reported procedure [20]. At ambient conditions, purified 11nm HgSe/CdS QDs (core diameter 4.8nm, HgSe mass = 6mg) was added to a scintillation vial with 0.3 mL oleylamine and 2.7 mL octane. Separately, 0.16 mL of 40% $(NH_4)_2S$ solution (10x surface equivalents to HgSe/CdS) was mixed with 3mL formamide (FA), and added to the HgSe/CdS solution to form a biphasic mixture. The vial was heated at 40°C with stirring for 5 minutes. The FA layer was removed, and washed with 3 mL of FA to remove excess $(NH_4)_2S$. The washing was repeated another time, after which the QDs were purified twice by precipitation-dispersion using methyl acetate and TCE. After treatment with $(NH_4)_2S$, the intraband absorption was completely bleached (Fig. 3.8).

To n-dope the QDs, the undoped HgSe/CdS QDs (containing 6 mg of HgSe cores) were

added to a three-neck flask with 0.6 mL of oleylamine and 5.4 mL hexadecane. After adding a calculated volume of 0.05M cadmium acetate solution (see Fig. 3.2D of main text. 1.0 mL of cadmium acetate corresponded to 1x surface saturation), the flask was connected to a Schlenk line and three vacuum-Argon cycles were performed. The flask was then heated to 180°C and kept at this temperature for 10 mins.

The reaction mixture was cooled to room temperature, and purified twice by precipitation – dispersion using methyl acetate and TCE. After the second precipitation, the pellet was dried under vacuum before dispersing in TCE for measurements.

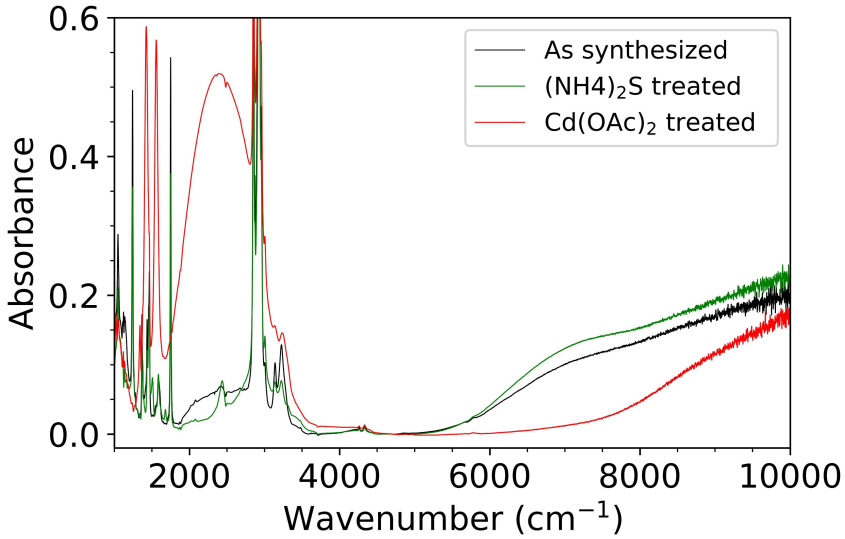

Figure 3.8: FTIR spectra of HgSe/CdS QDs (black) as synthesized, (green) after cALD with $(NH_4)_2S$ and (red) after treatment with cadmium acetate. The doping (N_e) could be controlled to any value between 0 and 2 electrons per QD.

3.6.9 Variations in synthesis of thick shell HgSe/CdS QDs

Synthesis at 160°C with $Cd(oleate)_2$:

Reaction solvent was a 10% solution of OAm in ODE.

The CdS precursor solution (1.5 mg/mL CdS) was prepared by dissolving 46 mg $Cd(DEDTC)_2$ and 74 mg $Cd(oleate)_2$ in 20 mL 10% OAm-ODE by vortexing at room temperature.

Thin shell HgSe/CdS QDs (6 nm diameter, synthesized by cALD) containing 3.3 mg of HgSe cores were purified and added to a 3-neck flask with 2.5mL of 10% OAm-ODE, and 4mg of $Cd(DEDTC)_2$ (corresponding to 1ML of CdS) was added. The flask was evacuated at room temperature in a Schlenk line for 10 minutes, and then filled with Argon. The flask was then heated to 140°C and kept at this temperature for 1 hour. The flask was then heated to 160°C and the CdS precursor was injected using a syringe pump at 1.31 mL/hour. Aliquots were taken and purified twice by precipitation with IPA and dissolution in TCE for TEM imaging. The shell grew like tetrahedra after 4 hours of injection (Fig. 3.9(A)), but became irregular at 19 hours (Fig. 3.9(B))

Synthesis at 220°C without $Cd(oleate)_2$:

Reaction solvent was the saturated amine mixture: a 2:2:1 mixture of hexadecane-dodecylamine-hexadecylamine by mass.

The CdS precursor solution (0.02M in CdS) was prepared by dissolving 164 mg $Cd(DEDTC)_2$ in 20 mL saturated amine mixture by vortexing at room temperature.

Thin shell HgSe/CdS QDs (6 nm diameter, synthesized by using $Cd(PDTC)_2$) containing 4 mg of HgSe cores were purified and added to a 3-neck flask with 2 mL of saturated amine mixture. Three vacuum – argon evacuation cycles were performed at room temperature, with evacuation till 1 torr. The flask was then heated to 220°C. When the temperature reached 200°C, the CdS precursor solution was injected at a rate 0.26 mL/min (3ML CdS in 10 mins). Aliquots were taken and purified by precipitation with IPA and dissolution in TCE for TEM imaging. The shell grew as rods after 10 mins of injection (Fig. 3.9(C)), with arms developing at 25 mins (Fig. 3.9(D)). This corresponds to a large (103) wurtzite feature in the SAED during transmission electron microscopy (Fig. 3.9(K))

Synthesis at 220°C with $Cd(oleate)_2$:

Reaction solvent was the saturated amine mixture: a 2:2:1 mixture of hexadecane-dodecylamine-hexadecylamine by mass.

The CdS precursor solution (0.02M in CdS) was prepared by dissolving 164 mg $Cd(DEDTC)_2$ in 20 mL saturated amine mixture by vortexing at room temperature. A 0.1M solution of $Cd(oleate)_2$ was prepared by adding 17 mg $Cd(oleate)_2$ to 0.25mL of saturated amine mixture and vortexing at room temperature.

Thin shell HgSe/CdS QDs (6 nm diameter, synthesized by using $Cd(PDTC)_2$) containing 4 mg of HgSe cores were purified and added to a 3-neck flask with 2 mL of saturated amine mixture, and 0.14 mL of cadmium oleate solution was added. Three vacuum – argon evacuation cycles were performed at room temperature, with evacuation till 1 torr. The flask was then heated to 220°C. When the temperature reached 220°C, the CdS precursor solution was injected at a rate 0.26 mL/min (3ML CdS in 10 mins). A 2.4 mL aliquot was taken at 10 mins, 0.05 mL of cadmium oleate was added and the CdS precursor was injected at 0.25 mL/min for 13 mins. The aliquots were purified twice by precipitation with IPA and dissolution in TCE for TEM imaging. The shell grew as uniform spheres at 10 mins of injection (Fig. 3.9(E)), with some faceting visible at 23 mins (Fig. 3.9(F)). The addition of cadmium oleate leads to a reduced (103) wurtzite feature in the SAED during transmission electron microscopy (Fig. 3.9(K)).

Synthesis at 220°C with excess $Cd(oleate)_2$:

Reaction solvent was the saturated amine mixture: a 2:2:1 mixture of hexadecane-dodecylamine-hexadecylamine by mass.

The CdS precursor solution (0.02M in CdS) was prepared by dissolving 164 mg $Cd(DEDTC)_2$ in 20 mL saturated amine mixture by vortexing at room temperature. A 0.1M solution of $Cd(oleate)_2$ was prepared by adding 135 mg $Cd(oleate)_2$ to 2 mL of saturated amine mixture and vortexing at room temperature.

Thin shell HgSe/CdS QDs (6 nm diameter, synthesized by using $Cd(PDTC)_2$) containing 4 mg of HgSe cores were purified and added to a 3-neck flask with 2 mL of saturated amine mixture, and 0.54 mL of cadmium oleate solution was added. Three vacuum – argon

evacuation cycles were performed at room temperature, with evacuation till 1 torr. The flask was then heated to 220°C. When the temperature reached 220°C, the CdS precursor solution was injected at a rate 0.27 mL/min (3ML CdS in 10 mins). After 10 mins, the solution was cooled to room temperature, divided into two parts and precipitated with IPA. One part was purified twice by precipitation – dispersion using IPA and TCE for TEM imaging. The other part was precipitated once with IPA, dispersed in 2.6 mL saturated amine mixture, and moved to the 3-neck flask with 0.55 mL of 0.1M cadmium oleate. After three vacuum – Argon cycles, the flask was heated to 220°C and the CdS precursor solution was injected at 0.139 mL/min for 10 mins. The solution was purified twice and imaged by TEM.

The QDs grew as uniform spheres till 10 mins (Fig. 3.9(G)), but homogeneous nucleation of CdS was observed at 20 mins (Fig. 3.9(H)).

3.6.10 Kinetics of decomposition of Cd(PDTC)$_2$

To determine to temperature for growth of a thin CdS shell on HgSe using Cd(PDTC)$_2$, we performed a kinetics study on the decomposition of Cd(PDTC)$_2$. A solution of 0.1 M Cd(PDTC)$_2$ in 20% OAm-ODE was prepared.

Thin HgSe/CdS QDs (synthesized using Cd(PDTC)$_2$) containing 4 mg of HgSe was added to a 3-neck flask with 2 mL of 20% OAm-ODE solution. Three vacuum-argon cycles were performed, and the solution was heated to 60°C. 0.33mL of Cd(PDTC)$_2$ solution was injected. Aliquots were taken immediately (0 mins), 2 mins, 5 mins, 10 mins and 30 mins after injection. The aliquots were stored in a freezer to prevent further reaction.

Absorption spectra of the aliquots were recorded in a quartz cuvette by dilution in TCE, and normalized to absorbance at 1000 nm. The kinetics study was also performed for reaction at 80°C. As shown in Fig. 3.10, the reaction is nearly complete in less than 2 mins at 80°C but took 10 mins at 60°C. The reaction temperature for growth of thin shell HgSe/CdS QDs using Cd(PDTC)$_2$ was thus set at 80°C.

3.7 Characterizations

3.7.1 Infrared absorption and photoluminescence measurements

All measurements were done on QDs dispersed in TCE in a cell with CaF_2 windows and a path length of 0.5mm. Absorption measurements were performed on a ThermoNicolet Nexus 670 FTIR spectrometer, a Nicolet Magna 550 FTIR spectrometer and an Agilent Cary 5000 UV-vis-NIR spectrometer.

Photoluminescence spectra were recorded using a step-scan FTIR spectrometer with an MCT detector and a gated integrator. The samples were excited with a 150mW 808 nm diode laser, modulated at 90 kHz. A Si wafer was placed in front of the detector to block the excitation light. The transmittance of the solution at 808nm was measured using a Si diode detector behind the sample cell. A 3.4µm long-pass filter was placed in front of the detector to block the 1.7 µm interband emission and preferentially measure the 5 µm intraband emission. The PL spectrum was corrected for detector response and atmospheric absorption following Melnychuk et. al [1]. The PL spectrum was normalized by the measured 808 nm absorbance, and was also corrected for the infrared absorption by TCE.

3.7.2 Photoluminescence lifetime measurements

Photoluminescence lifetime measurements were performed by Dr. Christopher Melnychuk. Photoluminescence lifetime measurements were performed using the upconversion apparatus described by Melnychuk et. al. [1] with minor modifications. Samples were dispersed in TCE and placed in a homemade CaF_2 cuvette for the measurements. The beam from a home-built Nd:YLF regenerative amplifier producing 6 ps, 1053 nm pulses at 1 kHz was split into two paths by an 80:20 beamsplitter. The weak path pumped the sample after attenuation, variable optical delay, and weak focusing by a spherical lens to a spot size of 0.5 mm at the sample. The pump optical fluence at the sample was 150 μJ/cm2. The strong

path was brought collinear with the intraband fluorescence by a homemade CaF_2 beamsplitter and parametric mixing in a KTA crystal generated light at the sum-frequency. Filters removed the fundamental and weak second harmonic of the laser. The sum-frequency pulse then passed through a monochromator to a silicon photomultiplier and a gated integrator discriminated it from the background. The spectral resolution of the measurement at 2050 cm^{-1} was 70 cm^{-1} FWHM. Due to the large optical density at 1053 nm of the samples, emission from only a thin liquid layer is detected and the time resolution is expected to be about 8 ps.

3.7.3 Measurement of PLQY and $1S_e$ occupancy

Absolute PL quantum efficiency measurements (PLQE) were done following previous reports [1] using a Spectralon integrating sphere for a reference partially doped HgSe/CdS QD solution. The area under the PL spectrum of HgSe/CdS QDs (normalized to 808 nm absorption and corrected for detector response) was taken between 1600 – 2800 cm^{-1} for intraband, and 4000 – 7000 cm^{-1} for interband spectra. The ranges were taken as 1600 – 3000 cm^{-1} and 5000 – 8000 cm^{-1} for the HgSe cores. The PLQE per unit area was then calculated by dividing the measured PLQE by sum of areas under the intraband and interband PL spectra. The PLQE of other samples were calculated by recording the PL spectra and using the PLQE per area calculated above.

The average occupancy of the $1S_e$ state (N_e) in the HgSe/CdS QDs was determined by undoping the QDs on treatment with I_2. FTIR absorption spectra of the QDs in TCE were measured before and after injection of I_2 in TCE (0.02M or 0.004M). Difference between subsequent spectra were used to calculate the $1S_e$ – $1P_e$ intraband absorption (see Fig. 3.11 for details).

Ne was then calculated as twice the ratio of intraband peak absorbance to the maximum intraband absorbance (Y-intercept in Fig. 3.2(C) in main text). The $1S_e(0)$, $1S_e(1)$ and

$1S_e(2)$ populations were calculated from Ne using a binomial distribution (Section 3.8.4). The fraction of doped QDs was taken as sum of $1S_e(1)$ and $1S_e(2)$ populations, and undoped fraction was $1S_e(0)$. The intraband and interband PLQYs were calculated by normalizing the measured PLQEs to the fraction of doped and undoped QDs respectively.

3.7.4 Particle Size Characterizations

Transmission Electron Microscopy (TEM) images were recorded using an FEI Spirit 120kV electron microscope and an FEI Tecnai F30 300kV microscope. pXRD spectra were recorded on QDs films on Si using a Bruker D8 Powder X-Ray Diffractometer.

3.7.5 Doping – dependent transient lifetime measurements

3.8 Calculations and analyses

3.8.1 Dissolution of thin shell HgSe/CdS QDs and deposition of HgCdSSe shell

During the initial stages of the thick shell HgSe/CdS synthesis, a fraction of the thin shell HgSe/CdS QDs dissolve and deposit on the remaining QDs as a HgCdSSe shell. This leads to a red tail in the visible spectrum beyond the CdS band edge, and larger core/shell sizes than calculated from the precursors added. A batch-to-batch variability is observed in the extent of dissolution, and it also depends on the heating rate. Two synthetic trials are described below that show a substantial QD dissolution (synthesis 1) and a negligible dissolution (synthesis 2).

Synthesis 1 and 2 were performed by the thick shell HgSe/CdS synthesis procedure mentioned in the Methods section. The reaction conditions were nearly identical, except that the syntheses used different batches of thin shell HgSe/CdS QDs, and synthesis 1 used started with a scale of 18 mg of HgSe, while synthesis 2 started with a scale of 6 mg of HgSe. As shown in Fig. 3.15(A, B), the core/shell sizes in synthesis 1 match well with the diameter expected from the $Cd(DEDTC)_2$ precursor added, but the synthesis 2 leads to much larger core/shell diameters. From the size discrepancy in synthesis 2, the fraction of dissolved QDs can be calculated:

Calculation of fraction of dissolved QDs

Denote the initial diameter as di , the expected final diameter as dexp , measured final diameter as dm , and initial number of nanocrystals as N. The initial volume of QDs is $N\frac{\pi}{6}d_i^3$, volume of shell material added is $N\frac{\pi}{6}(d_{exp}^3 - d_i^3)$. The total volume of QD material (HgSe + CdS) is then $N\frac{\pi}{6}d_{exp}^3$. Suppose a fraction x of thin shell HgSe/CdS QDs dissolve during initial stages of the thick shell synthesis. Now the volume of core HgSe material remaining is $N\frac{\pi}{6}d_i^3(1-x)$, volume of HgCdSSe shell material is $N\frac{\pi}{6}(d_{exp}^3 - d_i^3(1-x))$. Since the final diameter of the QDs is: $Initial\ QD\ diameter \times \left(\frac{Total\ QD\ volume}{Initial\ QD\ volume}\right)^{\frac{1}{3}}$, we have

$$d_f = d_i \times \left(\frac{N\frac{\pi}{6}d_{exp}^3}{N\frac{\pi}{6}d_i^3(1-x)}\right)^{\frac{1}{3}} = d_{exp} \times \left(\frac{1}{1-x}\right)^{\frac{1}{3}} \tag{3.3}$$

For synthesis 2, we have $d_i = 6.1nm$, $d_{exp} = 8.4nm$, $d_f = 11.5nm$, we can calculate the dissolved fraction, x =61%. Therefore 61% of the initial thin shell HgSe/CdS QDs dissolve and deposit as a HgCdSSe shell on the remaining QDs.

Doing a similar calculation for the second aliquot of QDs, we have have $d_i = 6.1nm$, $d_{exp} = 10.5nm$, $d_f = 15.3nm$, we get x =68%. This shows that a majority of the dissolution

of the QDs occurs during the initial stages of the thick shell synthesis.

The UV-Vis absorption spectra of HgSe/CdS QDs (Fig. 3.15(C)) from synthesis 2 show a broad red tail in the shell absorption beyond the CdS band edge, consistent with presence of an alloyed HgCdSSe shell. In contrast, the absorption spectra of samples from synthesis 1 show a sharp shell absorption edge, similar to the absorption of CdS QDs. The shell absorbances in synthesis 2 also have a larger intensity than synthesis 1, consistent with the larger sizes measured by TEM.

Despite the significant dissolution of QDs in synthesis 2, the FTIR spectra of HgSe/CdS QDs from synthesis 2 is similar to those from synthesis 1 (Fig. 3.15(D)). This is expected, since 220°C is much higher than the thermal stability window of HgSe, and the ripening dots dissolve nearly instantaneously. Hence none of the cores of the dissolving QDs survive, and the infrared properties of the HgSe/CdS QDs remain unaffected by the dissolution occurring during the synthesis.

3.8.2 Radiative and nonradiative lifetimes of HgSe and HgSe/CdS QDs

The radiative lifetime τ_R of a nanoparticle dipole transition is [100, 101, 102, 103]

$$\frac{1}{\tau_R} = \frac{\omega^3 p^2}{3\pi\epsilon_0\hbar c^3} \times \sqrt{\epsilon_2}\left(\frac{3\epsilon_2}{\epsilon_1 + 2\epsilon_2}\right)^2 \tag{3.4}$$

Here ω is the angular frequency, c is the vacuum light speed, $\hbar$ is the reduced Planck's constant, p is the transition dipole matrix element, ϵ_0 is the vacuum permittivity, and ϵ_1 and ϵ_2 are respectively the real optical dielectric constants of the nanoparticle and its environment. For the intraband transition in HgSe, we calculate the dipole matrix element as:

$$p = e\langle 1S_e|r|1P_e\rangle\langle u_{c,S}|u_{c,P}\rangle \tag{3.5}$$

where e is the electron charge, r is the position operator, $1S_e$ and $1P_e$ are the radial envelope functions, and $u_{c,S}$ and $u_{C,P}$ are the conduction Bloch functions at wavevectors $k_S = \frac{\pi}{R}$ and $k_P = \frac{4.49}{R}$. A two-band Kane model gives $\langle u_{C,S}|u_{C,P}\rangle \approx 1$ and spherical Bessel envelope functions give $\langle 1S_e|r|1P_e\rangle = 0.306R$ [113]. The Kane result for the Bloch overlap may slightly overestimate the overlap based on a comparison to tight-binding calculations on the similar HgTe system [114] and the calculated lifetime is therefore an upper limit. Using the material parameters in Table 3.1 and emission frequency as 2050 cm^{-1} for comparison with lifetime measurements, this gives a radiative lifetime of 900 ns. Taking into account the standard deviation uncertainty in measurement frequency (2050 ± 20) cm^{-1} and ϵ_1 (10 ± 2), we get the core radiative lifetime (900 ± 300) ns. From this calculated radiative lifetime and the measured intraband PLQY of 7.5 × 10^{-4} for HgSe QDs, the nonradiative lifetime is 700 ps, with a one-standard deviation range of 0.40 – 1.1 ns.

Quantity	Value
ϵ_1: optical dielectric constant of HgSe QDs	10 ± 2[115, 116]
ϵ_2: optical dielectric constant of TCE	2.25
ϵ_S: optical dielectric constant of CdS shell	5.3 [117]
R: Radius of HgSe core	2.4 nm
ω for emission at 2050 cm^{-1}	3.9 × 10^{14} rad/s

Table 3.1: Material parameters used for calculation of radiative rate in HgSe and HgSe/CdS QDs.

Growth of the CdS shell leads to a change in the dielectric screening and a decrease in the radiative lifetime. To calculate of the local field factor, we performed an electrostatics calculation of a core/shell dielectric structure analogous to a dielectric sphere [118, 119]. For a core/shell nanocrystal with core radius of R_1 and total radius of R_2, the radiative rate is

found to be:

$$\frac{1}{\tau_R} = \frac{\omega^3 p^2 \sqrt{\epsilon_2}}{3\pi\epsilon_0 \hbar c^3} \left(\left(\frac{R_2}{R_1} \right)^3 \left(\frac{9\epsilon_S \epsilon_2}{\left(\frac{R_2}{R_1} \right)^3 \left((\epsilon_S + 2\epsilon_2)(\epsilon_1 + 2\epsilon_S) - 2(\epsilon_2 - \epsilon_S)(\epsilon_1 - \epsilon_s) \right)} \right) \right)^2 \tag{3.6}$$

The radiative lifetime τ_R as a function of core/shell diameter is plotted in Fig. 3.16. The radiative lifetime approaches a value of 700 ns at diameters greater than 8 nm. Taking into account the uncertainties in frequency and ϵ_1, we get the core/shell lifetime to be (700 $\pm$ 160). We can therefore use this radiative lifetime for all thick shell HgSe/CdS QDs. From this calculated lifetime and the measured intraband PLQY of 2.1 $\times$ 10^{-2} for thick shell HgSe/CdS QDs, the nonradiative lifetime is 15 ns, with a one-standard deviation range of 7.7 – 28 ns.

3.8.3 Measurement of average diameter of bullet-shaped HgSe/CdS QDs

HgSe/CdS QDs develop an anisotropic bullet-shape for HgSe/CdS QDs at large shell thicknesses. To estimate the 'average' diameter, we assumed the nanocrystals to have the same volume as an ellipsoid with two diameters as the short length of the bullet (Fig. 3.17(B)) and the third diameter as the long axis of the bullet (Fig. 3.17(A)). The volume of the nanobullet was then approximated as $\frac{\pi}{6} d_1^2 d_2$, where d_1 is the bullet diameter and d_2 is the axis length. Nanocrystals appearing as circles in the TEM (Fig. 3.17(C)) were assumed to be bullets lying on the short face perpendicular to the axis. The diameter of the circles were thus taken as the bullet diameter d_2. The average d_1 and d_2 values were measured taking an average of 36 values each, and the average diameter was calculated as $d_{average} = (d_1^2 d_2)^{\frac{1}{3}}$.

3.8.4 Calculating the distribution of 1S$_e$(0), 1S$_e$(1) and 1S$_e$(2) QDs

The average 1S$_e$ occupancy (N$_e$) of HgSe in the core or core/shell QDs depends on the position of the Fermi level Ef, determined by the Fermi-Dirac distribution:

$$N_e = 2 \times \left(\frac{1}{e^{\frac{E_{1S_e} - E_f}{k_B T}} + 1} \right) \tag{3.7}$$

Assuming negligible electronic correlation, electrons can occupy the two spin states of 1S$_e$ independently. The fraction of QDs with 0, 1 and 2 electrons in 1S$_e$ then follows a binomial distribution:

$$\begin{aligned} 1S_e(0) \quad fraction &= \left(1 - \left(\frac{N_e}{2}\right)\right)^2 \\ 1S_e(1) \quad fraction &= 2\left(\frac{N_e}{2}\right)\left(1 - \left(\frac{N_e}{2}\right)\right) \\ 1S_e(2) \quad fraction &= \left(\frac{N_e}{2}\right)^2 \end{aligned} \tag{3.8}$$

A visual schematic of the distribution of QDs is shown in Fig. 3.18 for different Fermi level positions.

3.8.5 Fitting of intraband and interband absorptions

3.8.6 Fermi level-dependent defect-assisted nonradiative relaxation in thick shell HgSe/CdS QDs

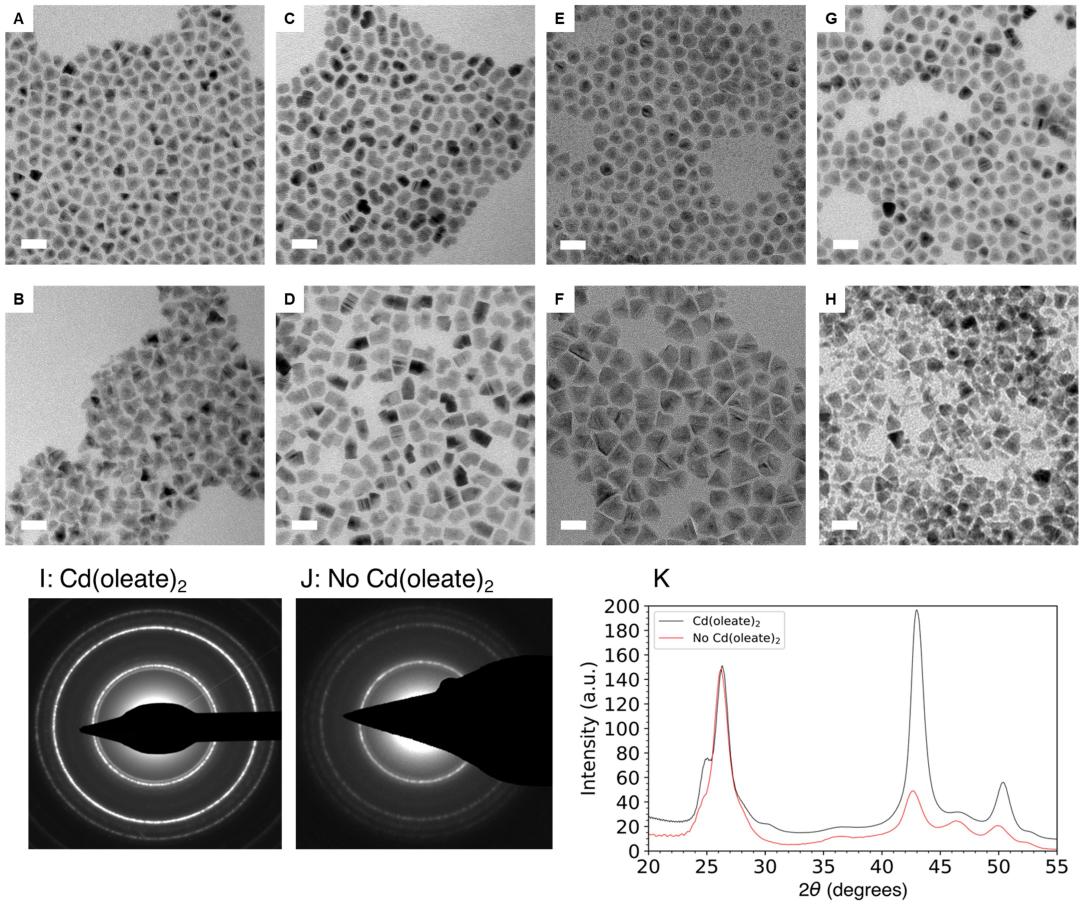

Figure 3.9: TEM images of thick shell HgSe/CdS QDs synthesized by different methods: (A, B) at 160°C with cadmium oleate, (C, D) at 220°C without cadmium oleate, (E, F) at 220°C with ∼1.5 surface equivalents of cadmium oleate, (G, H) at 220°C with excess cadmium oleate. All scale bars are 20 nm. (I, J) SAED images of HgSe/CdS QDs synthesized at 220°C (I) with cadmium oleate and (J) without cadmium oleate. The samples correspond to TEM images in (D) and (F) respectively; (K) radial integration of the SAED spectra to calculate the pXRD spectra. Addition of cadmium oleate during the reaction leads to a reduced (103) wurtzite feature in the pXRD (at 47°) and more compact shell growth.

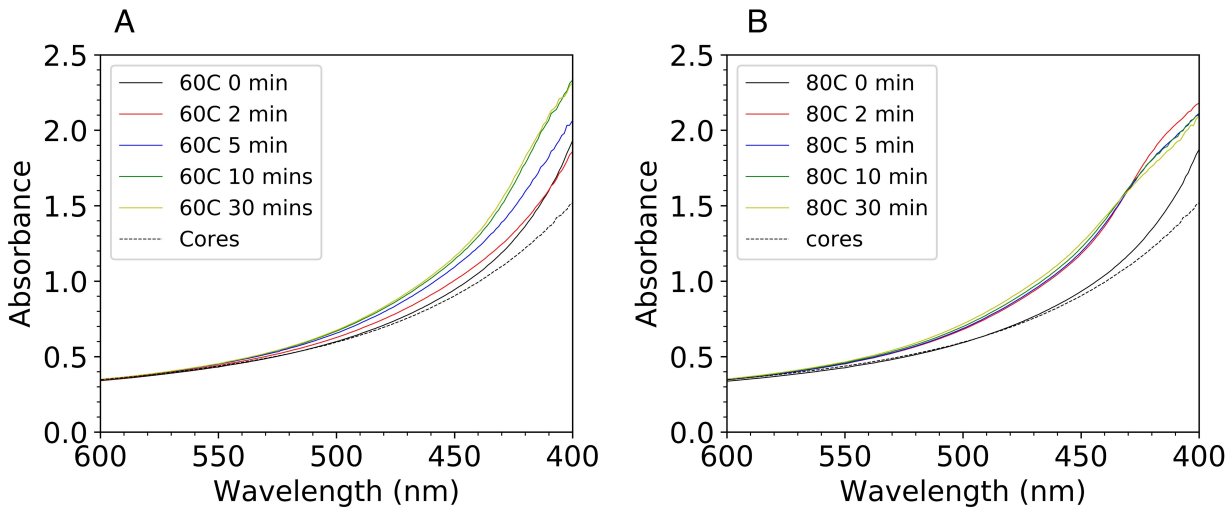

Figure 3.10: Absorption spectra of thin shell HgSe/CdS QDs after injection of $Cd(PDTC)_2$ at (A) 60°C or (B) 80°C, at different times after the injection. The reaction takes 10 mins to complete at 60°C, but finishes in less than 2 mins at 80°C. All spectra are normalized to absorbance at 1000 nm.

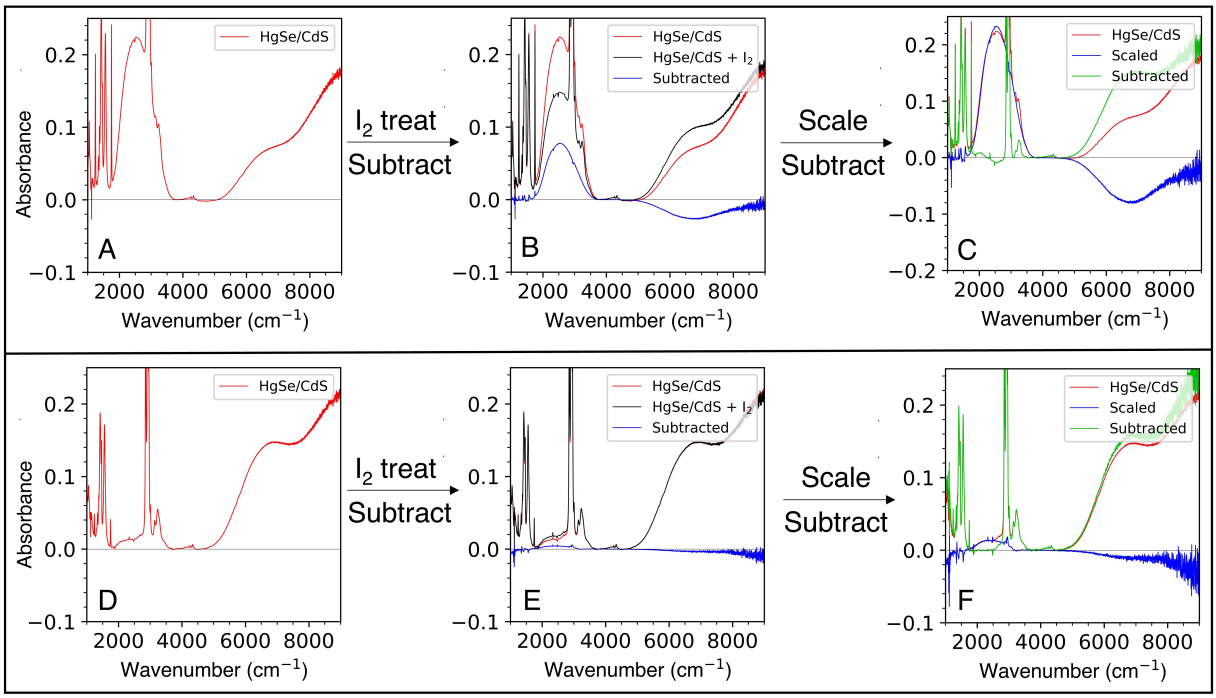

Figure 3.11: Subtraction to measure the intraband absorbance for HgSe/CdS QDs with (A) high doping ($N_e = 1.2$) and (D) low doping ($N_e = 0.07$). (B, E): The sample is treated with I_2 / TCE solution to change the doping (black spectra). The doping decreases if the initial doping was (B) high, and increases if it was (E) low. A subtraction was performed to remove the ligand absorption (blue spectra), resulting in a spectrum with intraband absorption and interband bleach. (C, F): The subtracted spectra from (B) and (E) are then scaled (blue spectra) to match the intraband absorbance of the original HgSe/CdS QDs. Taking a difference between the HgSe/CdS and the scaled spectra gives a sum of ligand and interband absorbance (green spectra). Despite the low n-doping in (D), the subtraction procedure can quantitatively give the intraband absorption (see Figure 3.12).

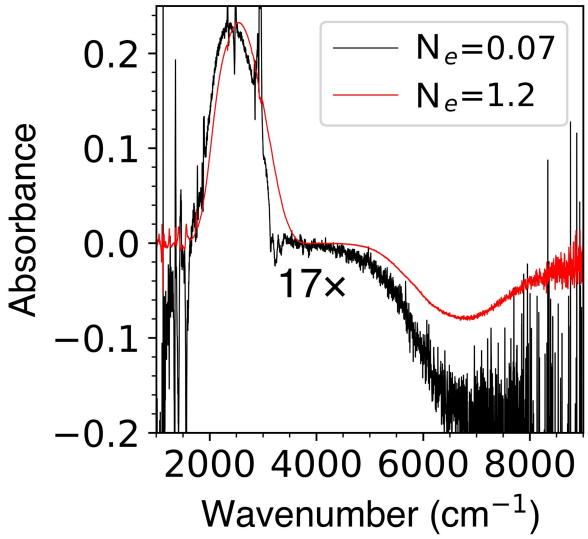

Figure 3.12: Intraband absorbances of HgSe/CdS QDs from Figure 3.11, scaled to compare the lineshapes. The intraband shapes match well, showing the robustness of the subtraction procedure. The interband shape of the $N_e = 0.07$ sample deviates significantly due to scattering artefacts during FTIR measurements.

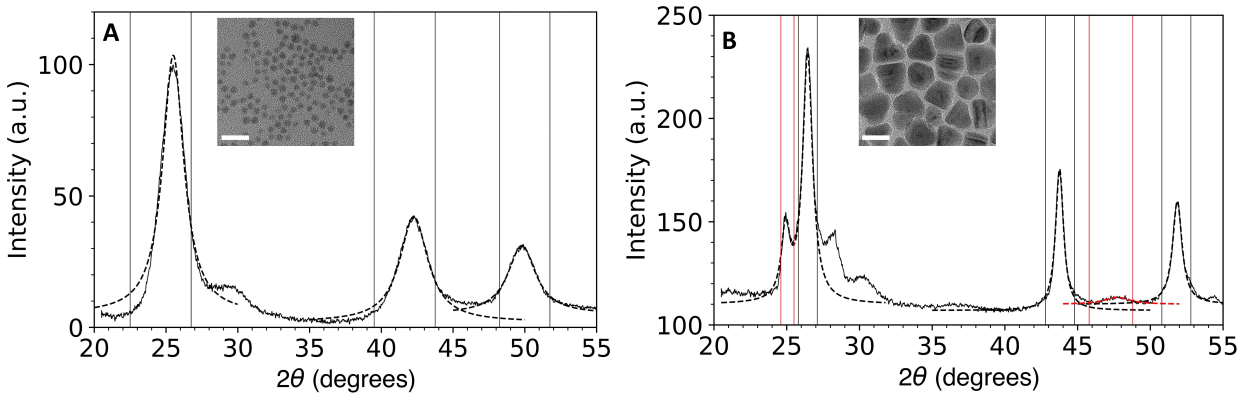

Figure 3.13: Scherrer analysis and Lorentzian fittings (dotted curves) for pXRD of (A) 4.8 nm HgSe and (B) 19 nm HgSe/CdS QDs. TEM images are shown in the insets, with a scale bar of 20 nm. Vertical black lines are the ranges used for the fittings of zincblende peaks, and the vertical red lines is the range used for fitting the (100) and (103) wurtzite peaks. The Scherrer sizes obtained are (4.0 ± 0.5) nm for HgSe, and (11.7 ± 1.5) nm for HgSe/CdS. The smaller Scherrer crystalline size compared to the particle size on TEM is likely due to the presence of grain boundaries and defects in the nanocrystals. To estimate the Wurtzite contribution in the HgSe/CdS spectrum, we assumed that the (100), (002) and (101) peaks have equal intensity, and the peak at 26° includes intensities from wurtzite (002) and zincblende (111) peaks. The zincblende:wurtzite ratio is then calculated as ratio of the areas of the zincblende (111) and wurtzite (100) peaks, which is found to be 3:1. Ratio of average area under the zincblende (220) and (311) peaks with area under the wurtzite (103) peak is 5:1.

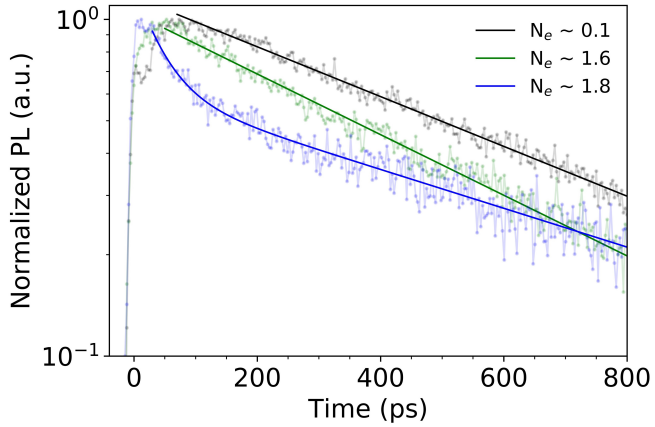

$$y(t) = ae^{-bt} + ce^{-dt}$$

N_e	a	b (ps)	c	d (ps)
0.1	1.165 ± 0	587 ± 26	-	-
1.6	1.042 ± 0	482 ± 23	-	-
1.8	0.609 ± 0	750 ± 540	0.660 ± 0.003	44 ± 18

Figure 3.14: Normalized transient PL measurements (points) on 12 nm HgSe/CdS QDs with different $1S_e$ occupancies (N_e) by doping with cadmium acetate. The Ne $\sim$ 0.1 and $N_e \sim 1.6$ were fit to single exponentials, while the Ne $\sim$ 1.8 was fit to a biexponential. The fitting parameters show that the average lifetime reduces with increase in doping. The noise baseline of the transient PL measurement is at 0.01. The features in early time dynamics suggest that intersublevel relaxation might depend on the doping level [1].

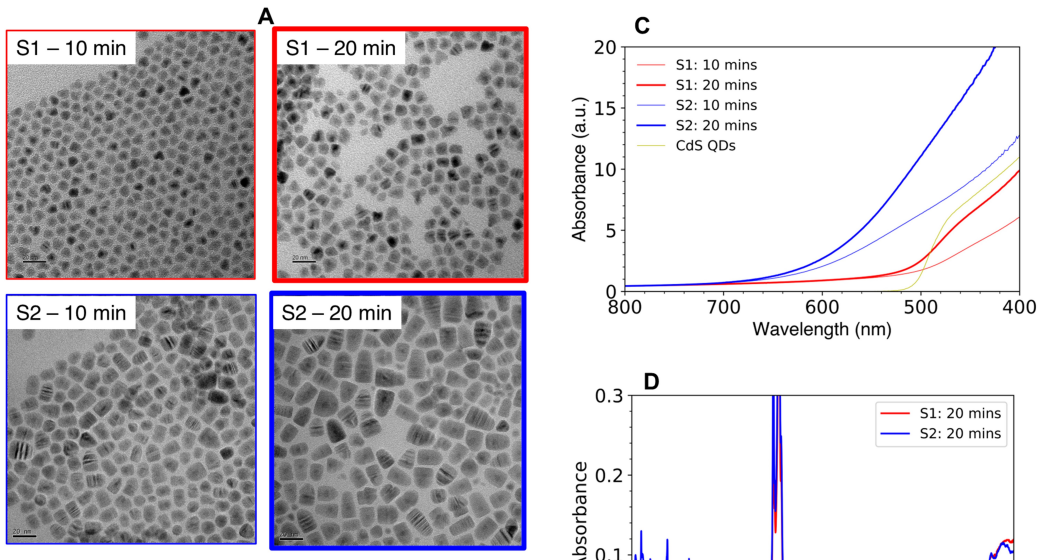

B

Sample	Expected diameter	Measured diameter
S1 – 10 mins	8.2 nm	8.9 nm
S1 – 20mins	**10.2 nm**	**10.5 nm**
S2 – 10mins	8.4 nm	11.5 nm
S2 – 20mins	**10.5 nm**	**15.3 nm**

Figure 3.15: (A) TEM images of thick shell HgSe/CdS QDs for syntheses (red) 1 and (blue) 2. Table (B) shows a negligible QD dissolution in synthesis 1 and the measured core/shell diameters match well with the expected diameters. Synthesis 2 shows a significant QD dissolution and the core/shell sizes are much larger than the expected size. (C) UV-Visible absorption spectra of HgSe/CdS QDs from (red) synthesis 1 and (blue) synthesis 2, normalized to absorbance at 808 nm. The absorbance of samples from synthesis 2 are much larger than synthesis 1. The broad absorption for samples from syntheses 2 confirm the presence of an alloyed HgCdSSe shell. Absorption spectrum of CdS QDs (yellow) is shown for reference. (D) FTIR spectra of HgSe/CdS QDs from syntheses 1 and 2 after 20 mins of reaction, showing nearly identical absorption features from the HgSe cores.

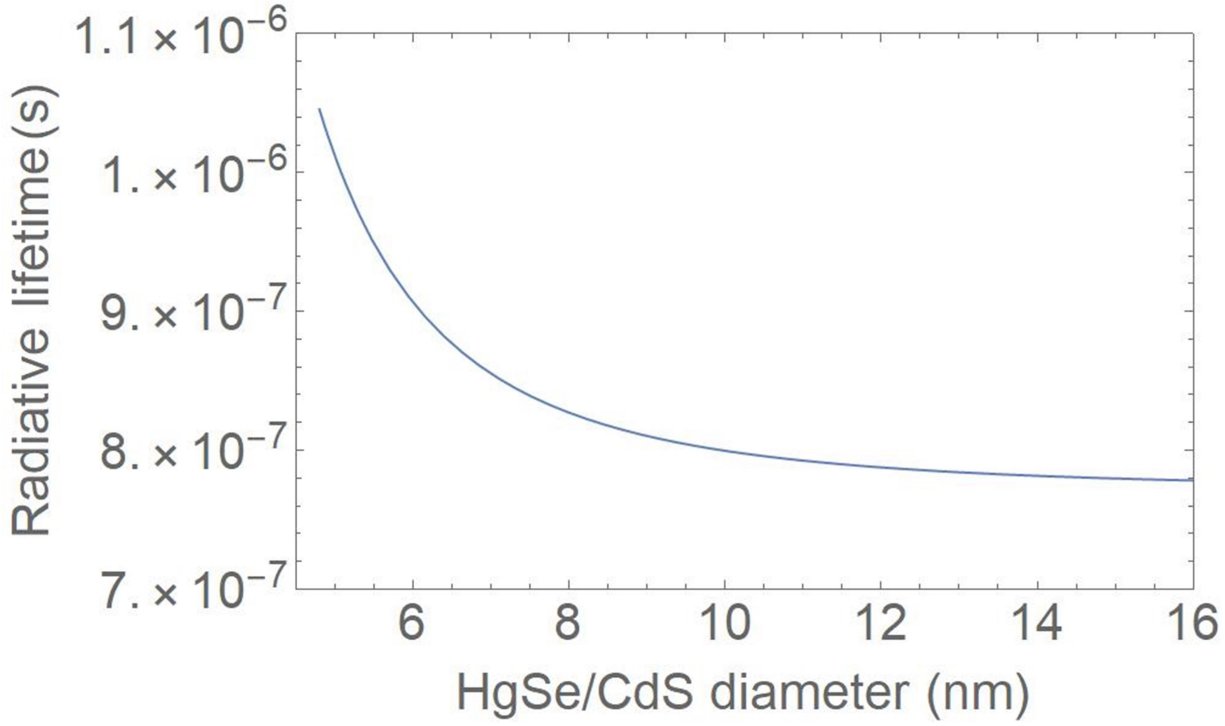

Figure 3.16: Radiative lifetime of HgSe/CdS QDs with a 4.8 nm diameter core, as a function of core/shell diameter. At diameters larger than 8nm, the radiative lifetime saturates to a value around 700 ns.

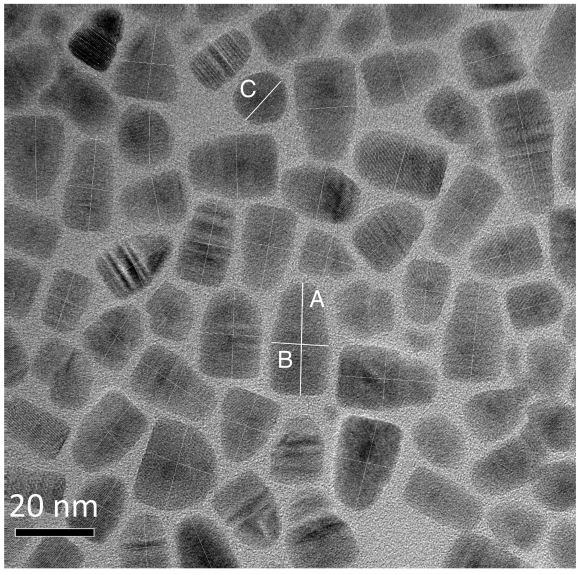

Figure 3.17: Determining the average diameter of bullet-shaped HgSe/CdS QDs.

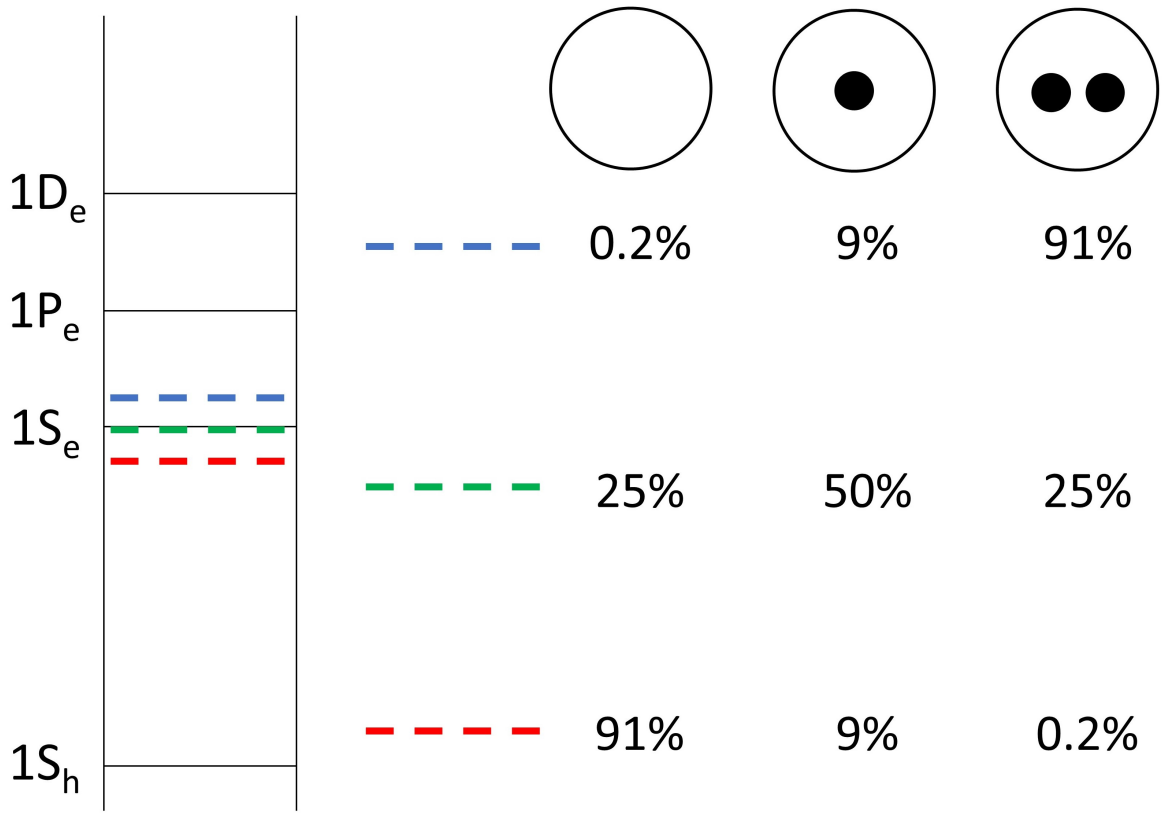

Figure 3.18: Distribution of QDs in $1S_e(0)$, $1S_e(1)$ and $1S_e(2)$ configurations in HgSe at different Fermi level positions (dashed lines).

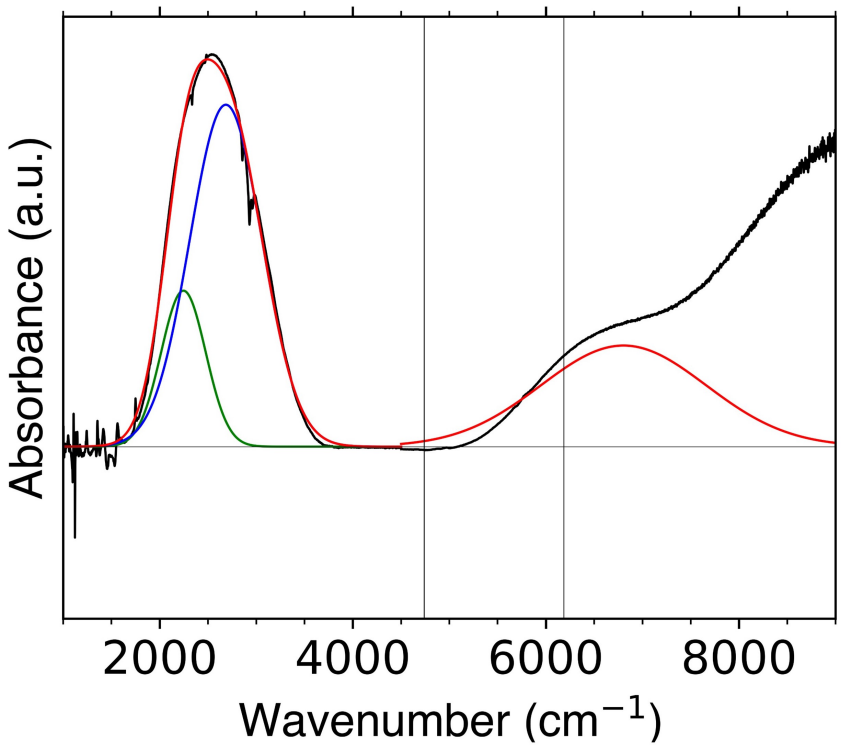

Figure 3.19: Fitting of intraband and interband spectra in thick shell HgSe/CdS QDs. The FTIR measurement is the black curve, while the red curves are fits. The intraband absorption was fit to a sum of gaussians (blue, green) due to the conduction band spin-orbit splitting [1], while the interband was fit to a single Gaussian. Ratio of areas of intraband and interband absorptions is 1.3 : 1, confirming the similar oscillator strengths for the two transitions. The fitting range for the interband absorption is shown by the vertical lines.

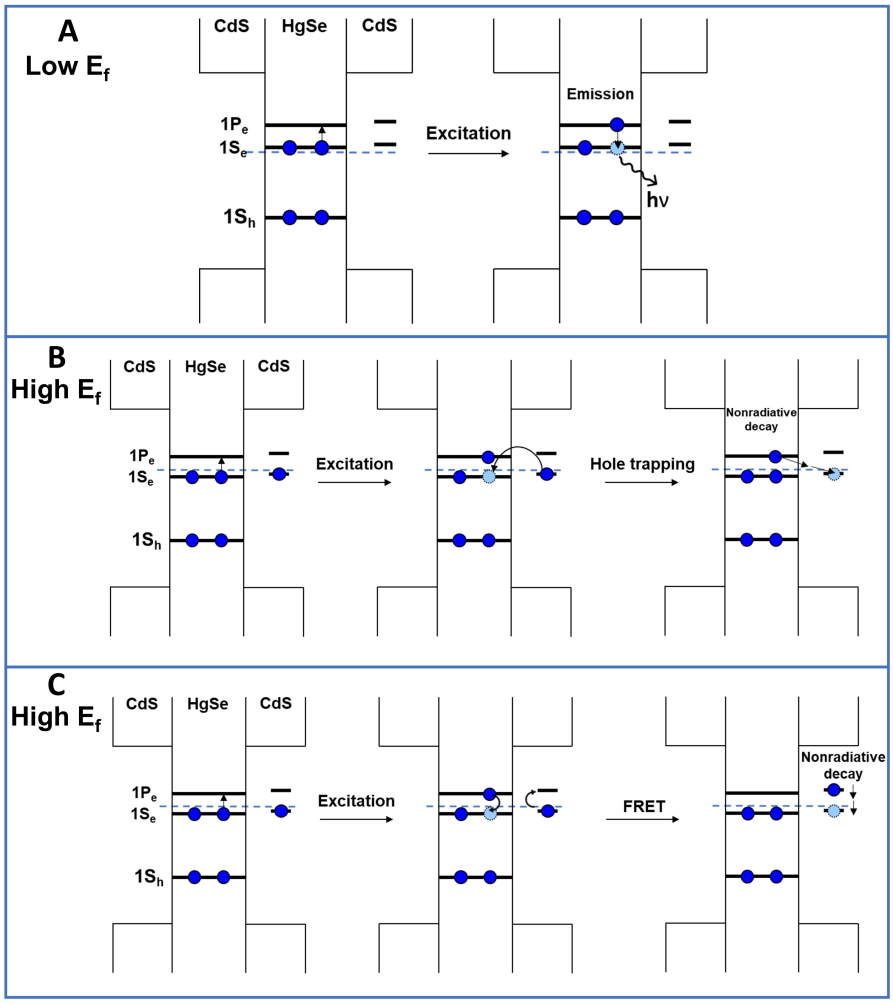

Figure 3.20: Fermi level-dependent defect-assisted nonradiative relaxation in HgSe/CdS QDs. Fermi level is denoted by the dashed blue line. Proposed mechanism of Fermi level-dependent PLQY for thick shell HgSe/CdS QDs at (A) low Fermi levels and (B, C) high Fermi levels. The CdS shell might have localized defect states (two levels are depicted) that are close to the $1S_e$ and $1P_e$ states of HgSe. (A) When the Fermi level is low, the defect states are empty, and the QDs display intraband photoluminescence on excitation. (B, C) When the Fermi level is high, the defect states get filled. When the QD is photoexcited, the filled defect state could introduce a nonradiative decay channel either by (B) hole trapping or by (C) near-field energy transfer (FRET). Bulk CdS is known to absorb infrared light by transitions between defect states [2, 3]. This absorption might be too weak to measure by FTIR, but the close proximity of the core to the shell can lead to a significant nonradiative decay.

CHAPTER 4

NONRADIATIVE MECHANISMS IN THE SECOND NEAR-INFRARED (SHORTWAVE INFRARED) WINDOW

This section has been adapted from Kamath et. al. [39]

4.1 Introduction

Fluorophores in the second near-infrared (NIR-II) (1.3 µm – 2.3 µm) range have shown potential for non-invasive bioimaging due to reduced autofluorescence, and significantly larger penetration into tissue compared to visible wavelengths [9, 4, 10, 120, 121, 122]. The optimal wavelength for in-vivo imaging is the NIR-IIb range (1.5 µm – 1.7 µm) which allows deepest penetration as a balance between reduced scattering and absorption by water.1 In-vivo imaging in the NIR-II region has been demonstrated in imaging mouse brain vasculature [123], lymph nodes [9] and tumors [4].

Several fluorophores have been developed for NIR-II bioimaging including organic molecules [124, 125], inorganic quantum dots [9, 4, 10] and carbon nanotubes [123, 126]. Despite significant progress, organic molecules show very low PLQYs in the NIR, due to their intramolecular vibrational relaxation to molecular vibrations by the energy gap law [127, 128]. The brightest NIR fluorophores are based on inorganic quantum dots (QDs) which show QYs up to 43% at 1.5 µm emission [5]. However, the emission is quenched drastically when the QDs are solubilized in water, with QYs of ∼2% at 1.7 µm. Design of brighter QD fluorophores can lead to deeper penetration for in-vivo imaging, at lower excitation powers [9].

The brightest reported QDs in the NIR-II range (1.3 µm – 2.3 µm) include QD structures based on PbS [5, 129, 130, 6, 131], PbSe [6], Ag_2S [132], InAs [4, 11], HgTe [7, 133, 134, 8] and HgSe [37, 38]. Nonradiative relaxation in QDs via surface trapping dominate role in visible-gap QDs, while QDs in the infrared appear to be limited by a near-field Forster energy

transfer to ligand molecules on the QD surface [6, 22]. This is exacerbated on making the QDs water-soluble, as water is strongly absorbing, and leads to a drastic decrease in the PLQY [4].

The energy transfer can be suppressed by exchanging the organic ligands by less absorbing molecules, or by growth of a thick type-I shell [38, 22, 30]. Solid-state ligand exchange has been demonstrated in Ag_2S [132] and PbS [129, 130] QD films, which show a PLQY of up to 85% at 1.4 µm. For in-vivo imaging, the only option is the growth of a thick shell, to suppress energy transfer to the surface ligand and solvent molecules. While thick CdS and CdSe shells have been grown on PbS [5] and PbSe [46] QDs, no substantial improvement in the PLQY is seen. Growth of the thick shell is also accompanied by a redshift of the exciton and lengthening of the PL lifetime, [46] which has been attributed to the quasi-type-II band alignment between the core and the shell [5, 46]. Similar observations have been reported for InAs/CdSe QDs, where the PLQY does not improve with shell thickness due to the unfavorable band alignment [4, 135]. This motivates the design of a core/shell material system with a type-I alignment, to obtain bright fluorophores in the NIR-II region.

HgSe/CdS QDs show bright mid-infrared emission when n-doping through the intraband transition [38]. Undoped HgSe QDs show emission in the NIR-II range. In contrast to PbS [5], PbSe [46] and InAs [4], HgSe has a type-I band alignment with CdS and CdSe [38, 20], which makes it a promising candidate as bright NIR-II fluorophores. CdSe is the ideal shell candidate for obtaining bright emission in HgSe, due to the type-I band alignment and near-zero lattice mismatch. Previous works have reported growth of a thin CdSe shell $<\sim$ 1.5nm thickness [37, 20], but growth of a thick spherical shell was not achieved.

In this work, we show the growth of a thick, roughly spherical CdSe shell around HgSe QDs, up to a final QD diameter of 13 nm. These QDs exhibit a PLQY upto 63% at 1.7 µm wavelength, which is >3 times brighter than previous reports. Our calculations show that the QYs are consistent with a Forster energy transfer to ligands and solvent molecules, and

demonstrate a strategy to obtain bright NIR-II fluorophores.

4.2 Synthesis of HgSe/CdSe core/shell QDs

HgSe cores were synthesized by adapting a previous report [1]. The sizes of the QDs were characterized by Transmission electron microscopy (TEM) and Small Angle X-Ray Scattering (SAXS). The cores had a diameter of 4.8nm – 5.2nm for emission at (1.7 µm – 2.0 µm) wavelengths. Most reports of CdSe growth require temperatures in excess of 200°C to obtain large sizes [46, 47]. Since HgSe QDs have a poor thermal stability above 100°C, it is necessary to first grow a thin protective CdSe shell at a low temperature before growth of a thick shell [38]. While previous studies report growth of thin shell HgSe/CdSe QDs using c-ALD [37, 20], the procedure is tedious, limited to small reaction scales, and is easily susceptible to independent nucleation.

In order to develop a robust and scalable growth of a thin CdSe shell at a low temperature, we designed a shell growth strategy using cadmium acetate and $(TMS)_2Se$ (Fig. 4.1a). These precursors are highly reactive, and form CdSe nanocrystals at temperatures as low as room temperature. By subsequent addition of Cd- and Se- layers by successive ionic layer adsorption and reaction (SILAR) at 90°C, the shell thickness could be precisely controlled (Section 4.7.3). The synthesis was robust, and could be scaled up to 80 mg of HgSe, with little or no observed independent nucleation up to a thickness of 3 monolayers (Section 4.7.3). After growth of 3 monolayers, the HgSe/CdSe QDs were thermally stable up to at least 150°C, while the HgSe cores were not stable above 120°C (Section 4.7.4).

These thin shell HgSe/CdSe QDs were then used as seeds for growth of a thick CdSe shell. Synthesis of large core/shell nanocrystals requires the use of highly reactive precursors and a high reaction temperature, in order to maintain a spherical shape and avoid independent nucleation [38, 47, 136, 45]. We adapted the protocol by X Peng and coworkers, where they demonstrated growth of CdSe using cadmium carboxylates and selenium suspension in

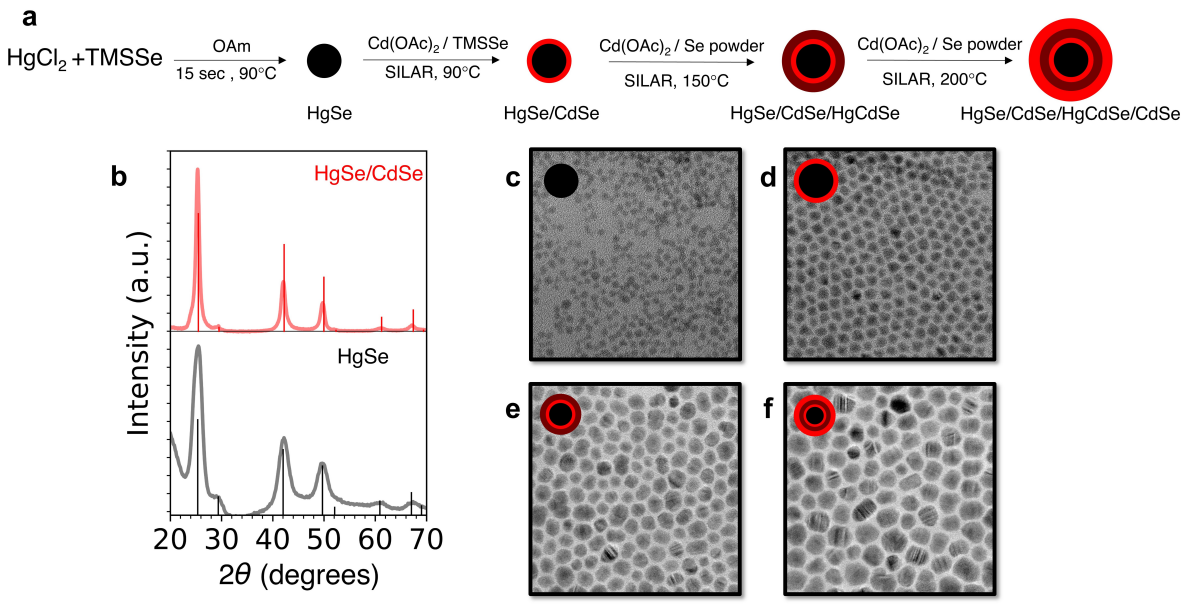

Figure 4.1: Synthesis of thick shell HgSe/CdSe QDs. a, Schematic of synthesis of HgSe/CdSe quantum dots (QDs). HgSe cores were synthesized by hot injection of $HgCl_2$ and bis(trimethylsilyl)selenide ($(TMS)_2Se$) at 90°C. A thin CdSe shell was then overcoated at 90°C using cadmium acetate and $(TMS)_2Se$, by successive ion layer addition and reaction (SILAR). Subsequent shell growth was performed at 150°C using cadmium acetate and selenium power. At this temperature, around 40-60% of the QDs dissolved and overcoated an alloyed HgCdSe shell around the remaining QDs. The final layers of CdSe were grown at 200°C. b, X-Ray diffraction (XRD) spectra of 5.2 nm HgSe (black curve) and 15.1 nm HgSe/CdSe (red curve) QDs, along with calculated bulk XRD spectra for zincblende HgSe (black bars) and CdSe (red bars) with lattice constants 6.08 Å and 6.05 Å respectively. The spectra confirm the growth of CdSe along the zincblende crystal structure like the cores, and the near-zero lattice mismatch between core and shell. c–f, Transmission electron microscopy (TEM) images of HgSe and HgSe/CdSe QDs with a diameter of (c) 5.2 nm, (d) 7.0 nm, (e) 10.2 nm, and (f) 13.0 nm.

oleylamine, which decomposed at a low temperature of 140°C [137].

A major challenge during growth of the CdSe shell is ripening and dissolution of QDs with a thin CdSe shell, which leads to deposition of an alloyed HgCdSe shell on the remaining QDs [38]. While the optical properties of the surviving HgSe cores are not affected, the alloyed HgCdSe shell absorbs part of the excitation light during PL measurements. To minimize ripening and dissolution of the cores (Section 4.7.7), we performed the shell growth through a two-step temperature increase. The reaction temperature was set to 150°C for two CdSe

monolayers, after which the temperature was increased to 200°C or higher for subsequent shell growth (Fig. 4.1a). During the heat-up to 150°C, typically ∼40-60% of the QDs dissolved and deposited an alloyed shell around the remaining QDs (Section 4.9.1).

Selection of the growth temperature is especially important. For obtaining thick spherical shells without independent nucleation, it is necessary to maximize the growth temperature [38, 136]. We observe substantial independent nucleation during growth at 180°C, which limits growth of QDs beyond 10 nm (Fig. 4.11). However, a higher growth temperature increases the tendency of alloying at the core/shell interface. We found the alloying temperature to depend on the core size. HgSe/CdSe QDs with cores emitting at 2.0 µm showed insignificant alloying during growth at 220°C, but cores emitting at 1.7 µm show a large blueshift in absorption and photoluminescence when grown at the same temperature (Fig. 4.12). We thus set the growth temperature for 1.7 µm - emitting QDs as 200°C. Using our synthetic design, we were able to obtain a final QD size of 13 nm at a growth temperature of 200°C, and a size of 16.5 nm at 220°C (Section 4.7.7).

4.3 Absorption spectra and optical properties of HgSe

An aliquot was taken after synthesis of HgSe cores at 15 seconds. The cores showed both interband absorption at 1.7 µm and an intraband absorption at 4.8 µm, which indicates they are partially n-doped (Section 4.10.1). By subtracting spectra of the cores at different dopings, we were able to calculate the average doping of the cores to be ∼1.05 electrons/QD (Section 4.9.2).

Aliquots were taken at different stages of the CdSe shell growth. Growth of the thick shell led to a steady increase in the CdSe absorption with a band-edge onset at 900 nm (Fig. 4.2a). X-Ray Diffraction measurements were performed on films of HgSe and HgSe/CdSe QDs (Fig. 4.1b). The measured spectra show good agreement with simulated spectra for zincblende HgSe and CdSe. The Scherer sizes calculated for the (220) peak at 42° were

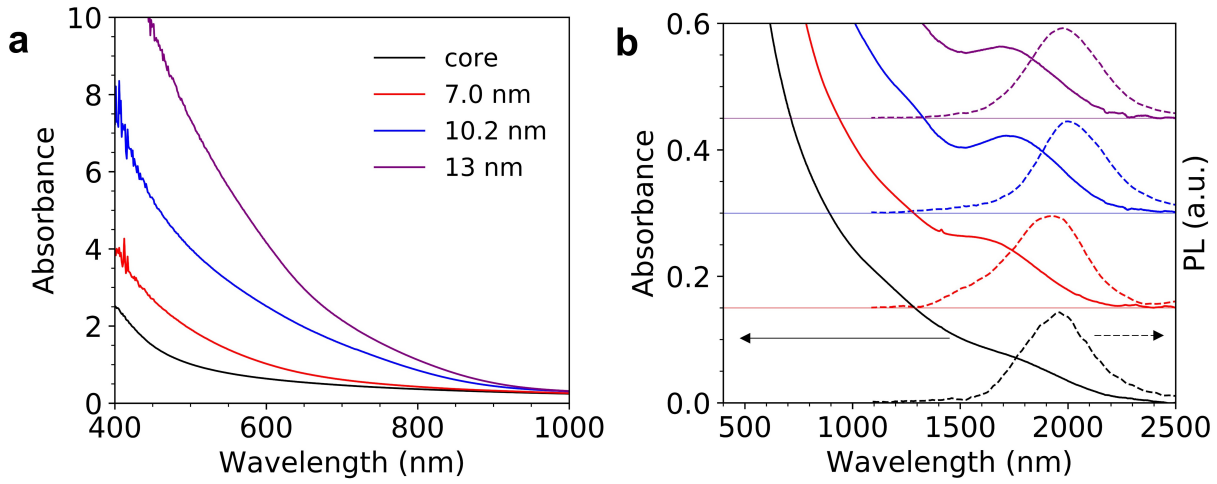

Figure 4.2: Absorption and photoluminescence. a, Absorption spectra of 5.2 nm HgSe cores and HgSe/CdSe QDs with different sizes. All spectra are normalized at 1400 nm. The increasing band-edge absorption from the CdSe shell is evident from the absorption onset at 900 nm. b, Absorption (solid) and photoluminescence (black) (PL) spectra of HgSe and HgSe/CdSe QDs. The absorptions have the same scale as in (a), but are vertically shifted for clarity. The absorption and PL spectra show negligible shift on shell growth, confirming the type-I band alignment of HgSe and CdSe.

3.7 nm and 9.3 nm respectively (Section 4.8.5), which show a fair agreement with the sizes measured by SAXS. The HgSe/CdSe QDs were intrinsic and showed a negligible intraband transition, regardless of whether the final layer was Cd- or Se- (Section 4.7.6). The thickest shell sample was an anomaly, which displayed an intraband absorption with roughly ∼0.85 electrons/QD upon ending with a Cd- step (Section 4.9.2). The interband emission was much weaker after stopping at a Se- step (Section 4.7.6), so all measurements were performed with Cd- as the final layer.

As seen from the absorption spectrum in Fig. 4.2b, the absorption features of the HgSe interband transition were maintained on growth of the thick CdSe shell. During growth of the thick shell at 150°C (Fig. 4.2a, blue), there was a significant decrease in the HgSe absorption intensity (Section 4.9.1), and a redshift of the absorption peak. This is consistent with dissolution of nearly half of the initial HgSe QDs, and deposition of an alloyed shell around the remaining QDs. The redshift of the absorption suggests that thin shell HgSe/CdSe QDs

with a smaller sized core were preferentially dissolved. Subsequent growth of the CdSe shell did not result in a change in the absorption peak wavelength or intensity. The lack of peak shifting confirms the type-I band alignment between HgSe and CdSe. This is in contrast to PbS, PbSe, and InAs QDs, which show a continuous redshift in the exciton peak upon growth of a thick shell due to their quasi type-II band alignment [4, 5, 46].

4.4 Photoluminescence and lifetime measurements

Photoluminescence (PL) spectra of the HgSe/CdSe QDs were recorded using an excitation wavelength of 808 nm and an incident power of 15 mW, using a step-scan FTIR. All spectra were recorded in solution in tetrachloroethylene (TCE). The HgSe/CdSe QDs showed bright interband emission with no shift in the spectra on shell growth. There was a ∼250 nm Stokes shift in the PL (∼90 meV), which likely arises from the size distribution of the cores.

Absolute PL quantum efficiency measurements were performed using a Spectralon integrating sphere, with an 808 nm excitation and a PbSe detector. We want to distinguish the PL quantum efficiency (PLQE) from quantum yield (PLQY). When the sample has a partial n-doping, there is an ensemble of QDs with 0, 1 and 2 electrons in the $1S_e$ state (denoted $1S_e(0)$, $1S_e(1)$, and $1S_e(2)$ respectively), each of which would have a specific PLQY. The absolute PLQE can be measured, but the PLQY would have to be calculated from the distribution of QDs with different $1S_e$ occupancies [38]. Only $1S_e(0)$ QDs would be expected to show interband emission due to Kasha's rule. To calculate the PLQY, we estimate the fraction of $1S_e(0)$ QDs in the ensemble by assuming a binomial distribution, and divide the PLQE by this fraction (Section 4.9.2).25 Since only the cores and 15.1 nm HgSe/CdSe QDs were partially n-doped, the PLQE and PLQY were the same for QDs of the remaining sizes (Section 4.10.1).

The HgSe cores showed a PLQY of 1.5% at 2.0 µm emission. Growth of the CdSe shell led to a monotonous increase in the PLQY, with a value of 48% for the thickest shell with

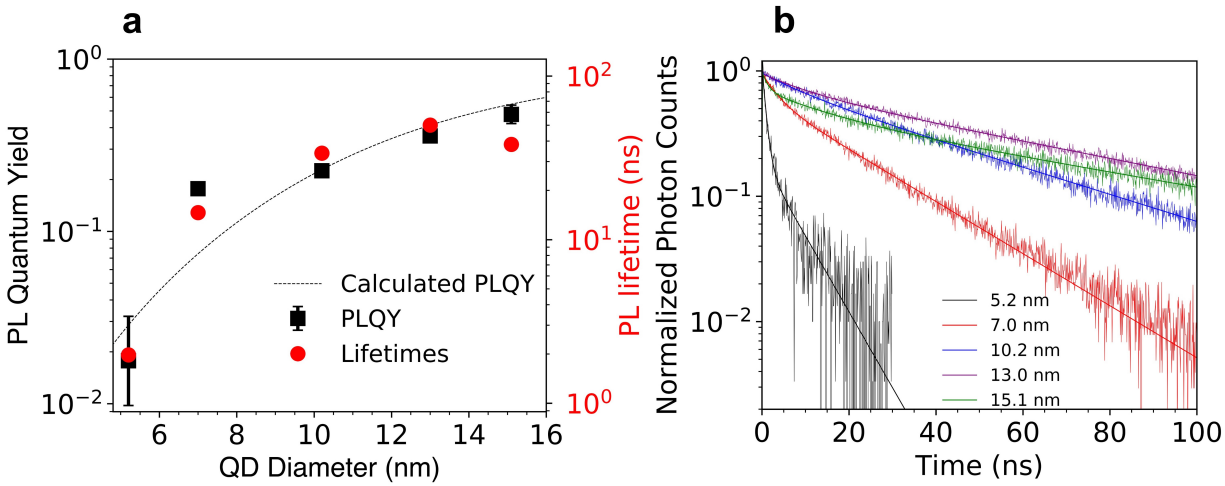

Figure 4.3: Quantum yield and lifetime measurements. a, Measured photoluminescence quantum yield (black squares) of HgSe/CdSe QDs with different shell thicknesses, calculated quantum yield (dashed curve) modelled by Forster-energy transfer to oleylamine ligands on the QD surface, and measured average PL lifetimes (red circles). The increase in average lifetime with QD size shows a quantitative agreement with the PLQY measurements. Error bars in PLQY correspond to lower and upper limits from the doping estimation. b, PL lifetime traces (line scatter) of the same HgSe and HgSe/CdSe QDs in (a). The 15.1 nm sample was fit to a triexponential, while the remaining samples were fit to biexponentials (fits are overlayed).

diameter of 15.1 nm (Fig. 4.3a). A similar trend was observed for QDs with smaller cores emitting at 1.7 µm, which showed a PLQY upto 63% (Section 4.9.5, 4.10.2). These QDs are >3 times brighter than the brightest fluorophores with PLQY ∼20% at 1.7 µm emission [8, 37].

To confirm that the increase in the PLQY is indeed due to a slowing of the nonradiative rate, we measured the PL lifetimes of HgSe and HgSe/CdSe QDs in solution (Fig. 4.3b). With the exception of the 15.1 nm diameter sample, the lifetime traces of all samples fit well to a biexponential function. The fast component comprised of ∼25% of the intensity for the HgSe/CdSe QDs, while it was ∼80% for the cores, which is likely due to a larger fraction of trap states in the cores. The 15.1 nm diameter sample was fit to a triexponential with ∼30% intensity exhibiting a very fast ∼1.4 ns decay. We attribute this to defects arising from the independent nucleation of CdSe on the surface of the QDs (Section 4.10.1).

We calculated the average PL lifetime to be a harmonic mean of the decay components (Section 4.10.1, 4B). The trend of the effective PL lifetime showed quantitative agreement with the PLQY measurements (Fig. 4.3a). From the measured lifetimes and PLQYs, we calculated the radiative lifetime for each QD sample. The radiative lifetime was similar for all QD samples, giving a value of 127 ns ± 30 ns. The constant radiative lifetime further confirms the type-I alignment of HgSe with CdSe.

4.5 Nonradiative mechanism

Quantum dots in the infrared show PLQYs that are lower than their visible counterparts. To determine the origin of the poor emission, we tabulated the PLQYs of the brightest reported QDs at different wavelengths (Fig. 4.4a). We have plotted the PLQY of our HgSe/CdSe QDs emitting at different frequencies (Fig. 4.4a, green stars). The QDs are ∼3 times brighter than previous QDs in the 1.7 µm – 2.0 µm range.

Despite the vast differences in the core and shell materials, all QDs in organic solvents (black and grey points) show a similar decreasing trend in the PLQY as the frequency is reduced. A similar trend is observed for QDs solubilized in water (Fig. 4.4a, red squares), which have ∼5 times lower PLQYs than their counterparts in organic solvents. This general trend suggests that the PLQY is limited by a mechanism that depends on the emission frequency, but is relatively insensitive to the QD material.

Guyot-Sionnest and coworkers [22] proposed a model for nonradiative relaxation involving Forster resonance energy transfer (FRET) of the QD emission to absorption of ligands on the QD surface. This model has been used to explain the lifetime and PLQY of QDs in the NIR and mid-IR regions [6, 7, 38, 22, 30, 138]. In this model, the PLQY of QDs in nonpolar solvents is calculated as follows [138] (See Section 4.9.4):

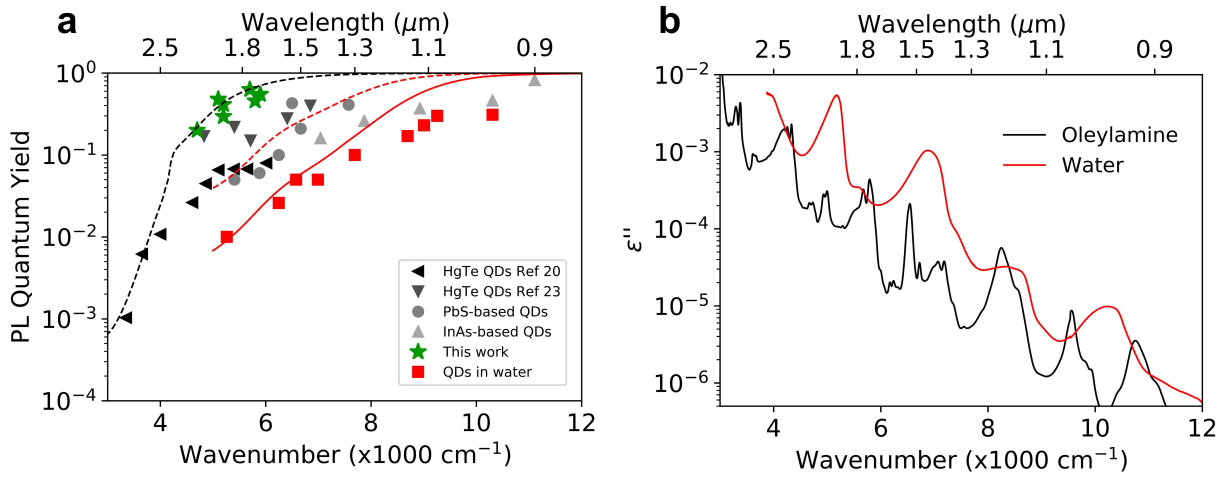

Figure 4.4: Predictions of FRET model, and comparison of PLQYs to other reports. a, Compilation of PLQYs of the brightest reported QDs at different emission wavelengths. Black and grey points are QDs in organic solvents [4, 5, 6, 7, 8]. Red points are QDs solubilized in water for in-vivo imaging [9, 4, 10, 11, 12]. Green stars are our HgSe/CdSe QDs in nonpolar solvents. The curves are calculated PLQY by ligand-FRET to oleylamine in TCE (black), and including solvent-FRET in water (red). Solid curve is for 6 nm diameter QDs, and dashed curve is for 13 nm diameter QDs. b, Measured imaginary refractive index of oleylamine and water as a function of frequency. Absorption by water is nearly 5 times stronger than oleylamine.

$$\frac{\gamma_{NR}}{\gamma_R} = \frac{3}{32\pi^3 n}\int_R^{R+\Delta R}\frac{dr}{r^4}\int\frac{\epsilon''(\bar{\nu})f_D(\bar{\nu})}{\bar{\nu}^3}d\bar{\nu} \tag{4.1}$$

Where γ_{NR} is the nonradiative rate, γ_R is the radiative rate, n is the index of the solvent, R is the QD radius, ΔR is the ligand length, ϵ'' is the imaginary dielectric function of the ligand absorption, f_D is the normalized QD emission spectrum and $\bar{\nu}$ is the frequency in wavenumbers. The PLQY can be calculated as:

$$PLQY = \frac{\gamma_R}{\gamma_R + \gamma_{NR}} = \frac{1}{1 + \frac{\gamma_{NR}}{\gamma_R}} \tag{4.2}$$

Since the nonradiative rate is proportional to the radiative rate, the PLQY is independent of the radiative rate, and hence insensitive to the QD material. This explains the relative insensitivity of the PLQY to the QD material. A notable exception is the series of HgTe QDs reported by Rogach and coworkers [8], where the PLQY is higher and shows a weaker frequency dependence than other reports.

To calculate the ligand-FRET rate for QDs in nonpolar solvents, we measured the absorption spectrum of oleylamine (Fig. 4.4b). Though the QDs reports in Fig. 4.4a have different nonpolar ligands, the FRET rate should be similar as the ligand absorption in the NIR-II is dominated by C-H overtones and combination bands (Section 4.9.3). We used the reported surface coverage of oleylamine on the QD surface as 1.8 nm^{-2} (see Section 4.9.4) [139], and set the emission spectra as Gaussians with standard deviation 0.1 times the emission frequency. We calculated the FRET- limited PLQY as a function of QD diameter (Fig. 4.4.3a), and as a function of frequency by setting the QD diameter at 13 nm, which is the average size of the HgSe/CdSe QDs (Fig. 4.4a dashed black curve).

The calculations show a good agreement with our measured PLQYs. The trend of calculated PLQY with frequency shows a reasonable agreement with the experimental data, with the scatter likely due to a variation in QD diameters, emission widths, different surface ligands, and contributions from other nonradiative processes.

Similar to ligands, FRET to solvent molecules can lead to a drastic quenching of the PLQY in NIR-absorbing solvents. To calculate the FRET rate to solvent molecules, we can use the solvent imaginary index ϵ'' in Eq. (1), and perform the integral from R+ΔR to infinity. To test the effect of solvent absorption on the nonradiative rate, we synthesized HgSe/CdSe QDs with an emission peak at 1.7 µm, and measured the PLQY in TCE (tetrachloroethylene), $CHCl_3$ and octane. These solvents show an increasing absorption at the QD emission wavelength (Fig. 4.18(c) and Fig. 4.20(a)). The PLQY shows a monotonous decrease with the solvent absorption, and shows good agreement with the simulation (Section

4.9.5).

FRET to water is expected to play a major role for QDs optimized for in-vivo imaging. Water exhibits a strong broadband absorption in the NIR-II, and leads to much poorer PLQYs compared to TCE. When we performed the FRET calculation for 6 nm diameter QDs, which is a typical size for water-solubilized QDs (Fig. 4.4a, solid red curve), we find a good agreement with the reported PLQYs. Our calculation for 13 nm QDs in water predict that the PLQY should be ∼12% at 1.7 µm emission (Fig. 4.4a, dashed red curve), which is ∼6 times brighter than the brightest fluorophores reported [9]. Growth of 20 nm QDs should lead to a PLQY of ∼30% in water. While this is not currently possible with our synthetic protocol, further shell growth can be achieved by using a lower-temperature shell material like an HgCdSe alloy.

4.6 Conclusions

Quantum dots (QDs) emitting in the NIR-IIb range show great potential for in-vivo imaging, but the PLQY of the fluorophores are quite low (∼2%). To determine the origin of the fast nonradiative decay, we use a model of Forster resonance energy transfer (FRET) to ligands and solvent molecules. Our calculation accounts for the ubiquitous decrease in the PLQY of QDs as the emission frequency is decreased, and also explains the lower PLQY of QDs solubilized in water. Previous attempts to improve the PLQY have been unsuccessful due to the lack of a type-I core/shell system. In order slow the nonradiative decay, we developed the synthesis of a thick CdSe shell on HgSe QDs. The type-I band alignment leads to a negligible spectral shift with increasing shell thickness. The thick shell HgSe/CdSe QDs show a PLQY upto 63% in the 1.7 µm – 2.0 µm range, which is ∼3 times brighter than the previous reported fluorophores. Our work demonstrates the importance of using thick shell QDs with a type-I band alignment for obtaining bright fluorophores.

4.7 Syntheses

4.7.1 Chemicals

Mercury chloride ($HgCl_2$) was purchased from Alfa Aesar (99.999%, #10808) and Sigma-Aldrich (99.5%, #215465). Mercury bromide ($HgBr_2$, 99%, #83353), cadmium acetate dihydrate ($Cd(OAc)_2$, 98%, #20901), selenium (Se, 99.99%, #229865), oleylamine (OAm, 70%, #909831) dodecanethiol (DDT, 98%, #471364), tetrachloroethylene (TCE, 99%, #443786), ethanedithiol (EdT, 98%, #02390), and octane (99%, #806910) were purchased from Sigma-Aldrich. Bis(trimethylsilyl)selenide ($(TMS)_2Se$, 97%, #SIB1871.0) was purchased from Gelest. Isopropanol (IPA, 99.9%, #A451-4) was purchased from Fisher. (Di-n-dodecyl) dimethylammonium bromide (DDAB, 98%, #B22839) was purchased from Alfa Aesar. $(TMS)_2Se$ was stored in a N_2 glovebox, while the rest were stored in ambient conditions. All syntheses were performed using the same bottle of oleylamine, as we observed variability in HgSe size and colloidal stability between different batches of the chemical.

4.7.2 Precursors and stock solutions

0.2M $(TMS)_2Se$ solution: The solution was prepared by adding 100 µL $(TMS)_2Se$ (0.4 mmol) to 1.9mL oleylamine in a N_2 glovebox.

0.2M $Cd(OAc)_2$ solution: 78 mg of $Cd(OAc)_2.2H_2O$ (0.3 mmol) was added to 1.5 mL oleylamine in a test tube, and heated till the solids dissolved. The solution remained clear as it cooled to room temperature.

0.1M $Cd(OAc)_2$ solution: 78 mg of $Cd(OAc)_2.2H_2O$ was added to 3 mL oleylamine and prepared as above.

0.1M Se suspension: 24 mg selenium powder was added to a vial, and 3 mL oleylamine was added. The suspension was kept on the sonicator during the thick CdSe shell synthesis, and mixed vigorously before use.

0.1M $HgBr_2$ solution: 36 mg of $HgBr_2$ (0.1 mmol) was added to 1 mL oleylamine in a test tube, and heated till the solids dissolved. The solution remained clear as it cooled to room temperature.

0.1M DDAB solution: 231 mg of DDAB (1 mmol) was added to 5 mL TCE in a vial, and sonicated till the solids dissolved.

2% EdT/IPA: 0.1 mL of EdT was added to 5 mL IPA in a vial.

4.7.3 Thin shell HgSe/CdSe QD synthesis

Rationale for synthetic protocol

HgSe cores were synthesized following the work of Melnychuk et. al . [1] using $HgCl_2$ and bis(trimethylsilyl)selenide ($(TMS)_2Se$) at 90°C – 100°C by hot-injection. A thin CdSe shell had to be grown at a low temperature, in order to impart thermal stability to the QDs before growth of a thicker shell. We did not observe robust and reproducible growth while attempting previous protocols for CdSe shell growth using cALD at room temperature [20, 37]. This motivated us to develop a protocol for growth of CdSe around 80°C – 100°C using successive ionic layer adsorption and reaction (SILAR). We chose cadmium acetate ($Cd(OAc)_2$) and bis(trimethylsilyl)selenide ($(TMS)_2Se$) as highly reactive precursors, which formed CdSe at temperatures as low as room temperature.

Due to the labile nature of the HgSe QD surface and the tendency to aggregate after precipitations, we designed the growth of the thin CdSe shell in the HgSe reaction mixture without purification. Unlike typical mercury chalcogenide syntheses which use a 2:1 excess of Hg to chalcogen [1, 140], we used a 1:1 ratio to avoid incorporation of Hg during the CdSe growth. During our trials, we observed that growth of HgSe QDs was complete in less than 15 seconds (Fig. 4.5), while the n-doping of the QDs increased after further reaction. This suggests that $(TMS)_2Se$ completely reacts within 15 seconds, and the $HgCl_2$ in solution continues to react and n-dope the QDs through a surface dipole-dependent Fermi level [85].

This motivated us to start the CdSe growth at 15 seconds after HgSe nucleation.

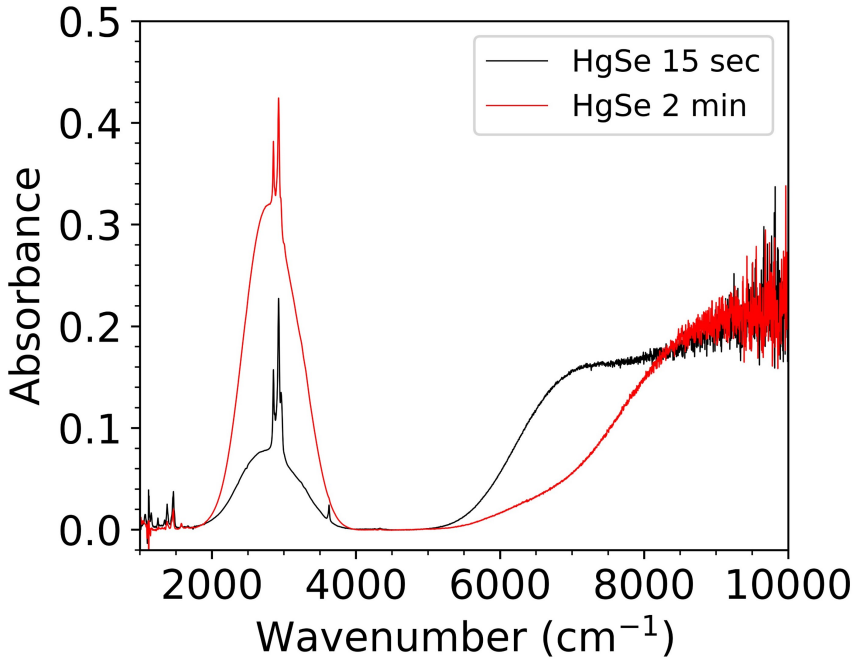

Figure 4.5: Testing kinetics of HgSe QD synthesis. FTIR absorption spectra of equal volumes of cleaned HgSe aliquots at 15 seconds (black) and 2 minutes (red) after $(TMS)_2Se$ injection. The equal absorption at 9000 cm^{-1} and identical intraband peak positions suggests complete reactivity within 15 seconds of $(TMS)_2Se$ injection. The n-doping increases through 2 minutes, suggesting the $HgCl_2$ continues to react.

Calculation of Cd- and Se- precursor volumes

The Cd precursor was 0.2M $Cd(OAc)_2$ in oleylamine, and the Se precursor was 0.2M $(TMS)_2Se$ in oleylamine. It was critical to add equal molar amounts of Cd- and Se- precursors to prevent independent nucleation. During synthesis of HgSe,1 we observed the formation of ~20 mg HgSe (0.07mmol) for addition of 0.1 mmol of $(TMS)_2Se$ and 0.2 mmol of $HgCl_2$. This was contrary to the observation of 100% $(TMS)_2Se$ reaction at 15 seconds (Fig. 4.5). We reasoned that the $(TMS)_2Se$ stock has a partial reactivity of ~70% due to decomposition over extended storage. The calculated Se- volumes was divided by 0.7 to account for the incomplete reactivity. Precursor volumes for each Cd- and Se- cycle were calculated for

saturation of the QDs by one monolayer of the ion. Fig. 4.6 shows the calculated volumes for a 20mg scale of HgSe:

Time (min)	HgSe Mass (mg)	Precursor	Inject vol (mL)	Total vol (mL)	Final Size (nm)
0				5.5	4.8
0.25	20	0Cd	0.17	5.67	5.15
5	20	1Se	0.27	5.94	5.5
7	20	1Cd	0.22	6.16	5.85
12	20	2Se	0.35	6.51	6.2
14	20	2Cd	0.28	6.79	6.55
19	20	3Se	0.44	7.23	6.9
21	20	3Cd	0.34	7.57	7.25

Figure 4.6: Calculation of Cd- and Se- precursor volumes during growth of thin shell HgSe/CdSe QDs.

Using this protocol, we were able to observe quantitative growth of the CdSe shell, with roughly ∼0.7 nm increase in the total QD diameter as expected. Little or no independent nucleation with observed till 3 monolayers of CdSe. Subsequent layers led to observation of independent nuclei with a smaller final QD size than expected (Fig. 4.7).

The volumes of injected Cd- and Se- were critical to prevent independent nucleation. If the volumes for each cycle were doubled, substantial independent nucleation was observed.

Synthetic protocol

The following protocol yielded ∼20 mg of HgSe cores. The protocol could be scaled 4x with no noticeable differences. HgSe core size was ∼4.8 nm.

$HgCl_2$ (0.1 mmol, 27 mg) was added to a 3-neck flask with 5mL oleylamine. The flask was equipped with a stir bar, rubber sleeve stoppers with a thermocouple attached, and connected to a Schlenk line manifold. Three vacuum (p∼1 torr) – Argon flush cycles were performed at room temperature, and the flask was heated at 100°C for ∼30-60 minutes. The temperature was then set to 90°C. 0.5mL of 0.2M $(TMS)_2Se$ solution was injected swiftly

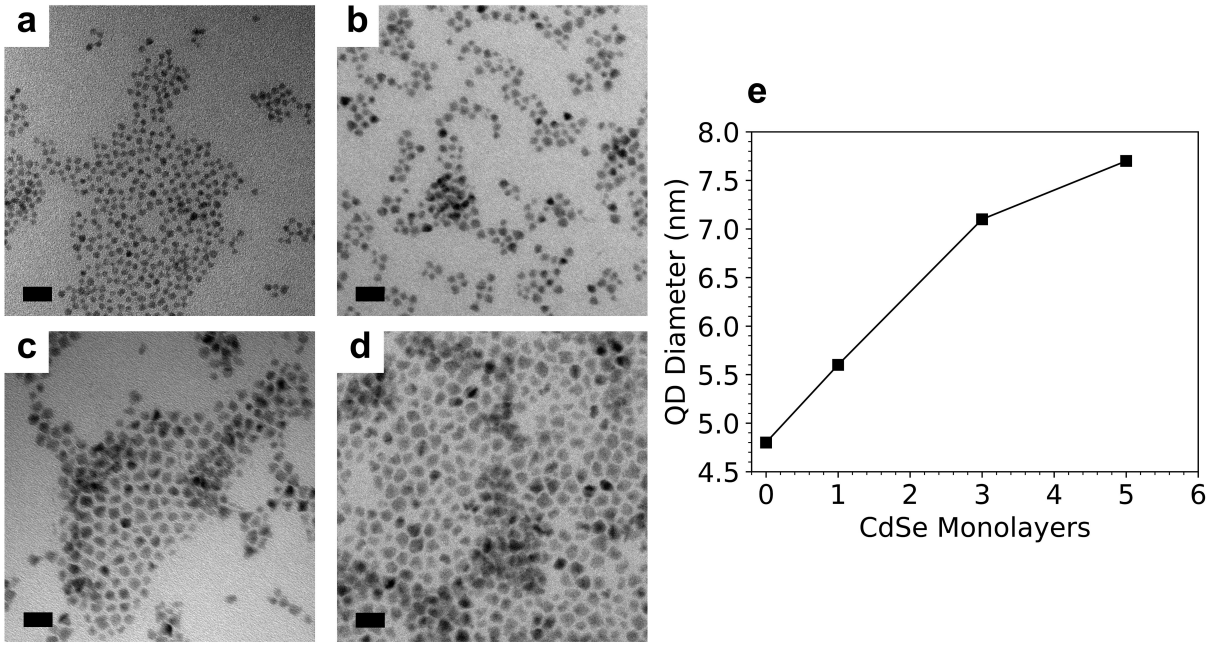

Figure 4.7: Testing the limit of thin CdSe shell growth. a-d, TEM of HgSe QDs (a) and HgSe/CdSe QDs with one (b), three (c) and five (d) monolayers of CdSe grown at 90°C. Significant independent nucleation is observed at five monolayers. Scale bars are 20 nm. e, Plot of total QD diameter vs CdSe monolayers grown. The size increase is linear till 3 monolayers with roughly 0.7 nm increase per monolayer as expected. The growth tapers at 5 monolayers, likely due to deposition of CdSe precursors on the independent nuclei.

into the flask, which led to the solution instantly turning black, and a stopwatch was started. At 15 seconds, a calculated volume of 0.2M $Cd(OAc)_2$ solution ("0Cd") was injected over a period of ∼15 seconds. After 5 minutes, a calculated volume of 0.2M $(TMS)_2Se$ solution ("1Se") was injected over a period of ∼15 seconds. Subsequent cycles were performed as necessary, with a 2-minute reaction time for Se- cycles and 5 minute reaction time for Cd-cycles. Aliquots were taken if necessary, using a glass syringe with a metal cannula. For HgSe (at 15 secs from start of reaction), the aliquot was added to a test tube containing 0.1M $HgBr_2$ – oleylamine solution (equimolar to the amount of Hg in the aliquot). This was found necessary to maintain colloidal stability during precipitations. Aliquots were rinsed with equal volume of octane to collect residual solution in the syringe. The reaction was typically stopped after 3 CdSe monolayers, leading to QDs with a diameter $\sim$ 7 nm (denoted

HgSe/3CdSe).

Concentration of the thin shell HgSe/CdSe stock solution was determined by measuring the absorbance at 700 nm. Absorption at this wavelength should be dominated by the HgSe cores, with negligible shell absorption. The concentration of HgSe was determined using the cross-section of HgSe as 3.5×10^{-18} cm^2 per Hg atom (calculated from the reported cross-section at 415 nm and the measured HgSe absorption spectrum) [1]. The typical reaction yield was ∼20-25 mg of HgSe.

The stock solution was transferred into a glass vial and stored in a freezer. The stock solution was directly used for synthesis of a thick CdSe shell.

Aliquots were purified by two cycles of precipitation – dissolution before characterization. All purifications were performed in air at ambient conditions. The solution was centrifuged to precipitate larger QDs (if any). The solution was then precipitated by addition of IPA (ethanol for HgSe) and centrifugation. The supernatant was discarded, and the precipitate was dispersed in TCE, leading to a concentration of ∼10 mg/mL of HgSe. 0.1M DDAB/TCE was added (0.1× volume of TCE), and the solution was precipitated by addition of IPA and centrifugation. The supernatant was discarded, the precipitate was lightly dried by blowing nitrogen, and then dispersed in TCE for characterization.

4.7.4 Testing the thermal stability of thin shell HgSe/CdSe QDs

The thin shell HgSe/CdSe QDs were tested for thermal stability at 150°C, which would be the growth temperature of the thicker CdSe shell. Thermal stability was tested through PL measurements as it is more convenient than annealing in solution.

For testing thermal stability of the cores, HgSe/Cd QDs (after the '0Cd' cycle, Fig. 4.6) were purified twice, dispersed into TCE and dropcasted into a film on an aluminum substrate. The PL of the film was measured. The sample was annealed at 80°C for 2 minutes, and the PL was recorded again. The annealing was performed again at 120°C for 2 minutes, and the

PL was recorded.

For HgSe/CdSe films with different shell thicknesses, the solutions were similarly purified twice, dispersed into TCE and dropcasted on aluminum substrates. The films were treated with a 2% solution of EdT in IPA for removing the long chain ligands. The PL was then recorded. Annealing was sequentially performed at 110°C and 150°C for 2 minutes each, and PL spectra were recorded.

The data is presented in Fig. 4.8, where the samples are the same as in Fig. 4.6. The PL spectra clearly show that the cores are not thermally stable at 120°C, while the thermal stability of HgSe/CdSe QDs progressively increases with number of monolayers. The 3-monolayer sample is thermally stable at 150°C, and these QDs were used as seeds for growth of a thicker CdSe shell.

4.7.5 Thick shell HgSe/CdSe QD synthesis

Rationale for synthetic protocol

The thin shell HgSe/CdSe QDs were used as seeds for growth of a thicker shell. We adapted the work of Xiaogang Peng and coworkers, which employed a suspension of selenium in oleylamine, that reacted at temperatures as low as 140°C [137]. We used cadmium acetate as the Cd- reagent, as it is much more reactive than longer carboxylates and enables a lower growth temperature.

The growth temperature was set as 150°C for growth of two monolayers of SeCd. During the heat-up stage, roughly ∼60% of the QDs dissolved and deposited as an alloyed HgCdSe shell on the remaining QDs (see Section 4.9.1 for characterizations). After the first monolayer of SeCd, the QDs were thermally stable, and no further dissolution was observed. After growth of two SeCd layers at 150°C, the temperature was increased to 200°C for further shell growth. The higher growth temperature was necessary to enable growth of a spherical shell. After a final QD size of ∼13 nm, the shell started to develop a tetrahedral-like morphology

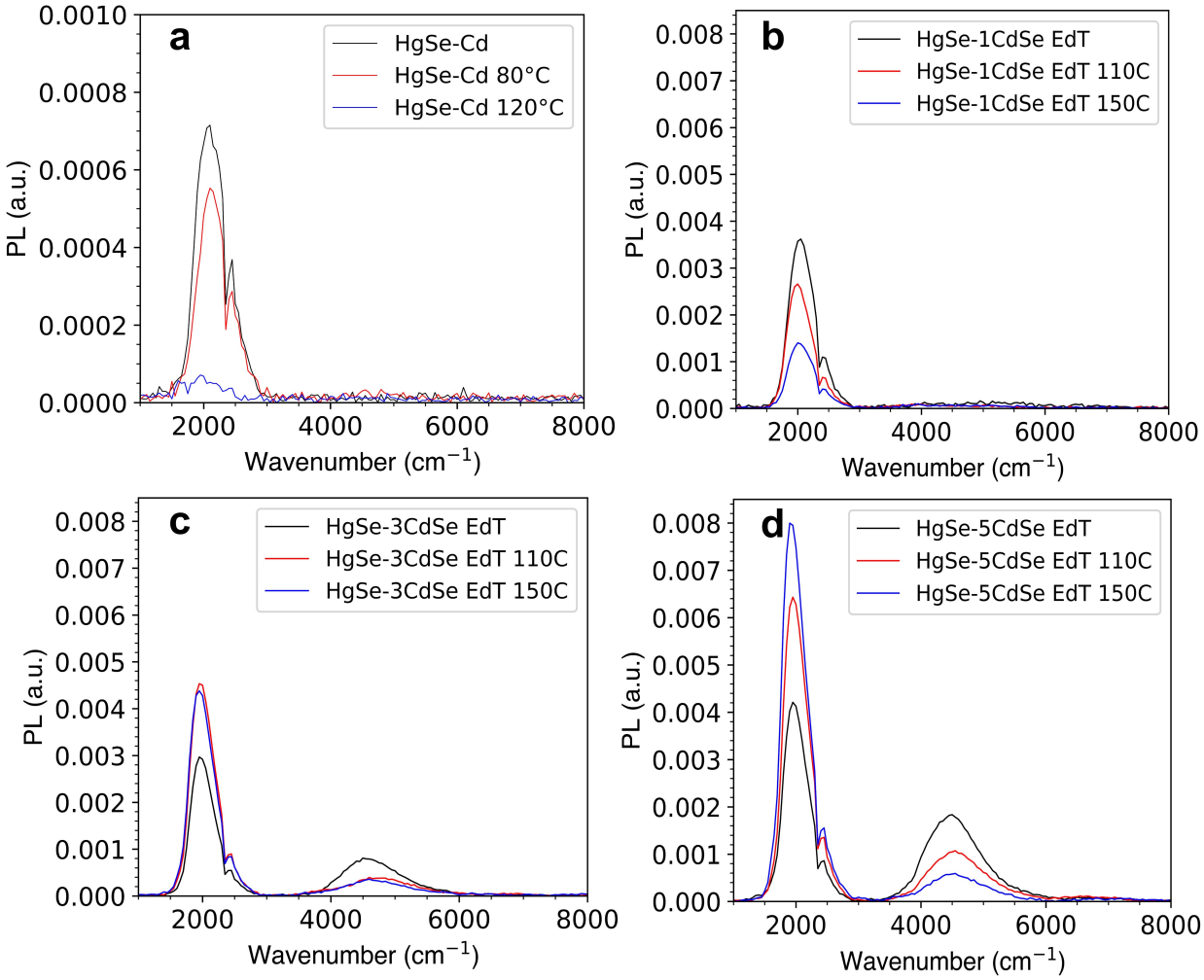

Figure 4.8: Testing thermal stability of: a, HgSe QDs and b-d, HgSe/CdSe QDs with different number of shell monolayers. Samples are the same as in Fig. 4.6.

with the onset of independent nucleation (see Section 4.7.7). When the growth temperature was 220°C, the QDs remained spherical up to ∼16.5 nm, after which independent nucleation was observed. The synthesis was ended with a Cd- cycle, as the PL was much weaker after ending with a Se- cycle (see Section 4.7.6).

The thin shell HgSe/CdSe QDs could directly be heated to 200°C/220°C for shell growth, but this led to a larger fraction of dissolved QDs compared to 150°C.

Calculation of Cd- and Se- precursor volumes

The Cd precursor was 0.1M $Cd(OAc)_2$ in oleylamine, and the Se precursor was 0.1M Se suspension in oleylamine. Precursor volumes for each Cd- and Se- cycle were calculated for saturation of the QDs by one monolayer of the ion. After growth of the first SeCd monolayer, the calculation was modified to account for the ∼60% dissolution of QDs. For example, starting with 7.0 nm diameter HgSe/CdSe QDs with 8 mg of HgSe, the expected QD diameter after one SeCd layer is 7.7 nm, but the measured size is typically 10.5 nm, which corresponds to a 60% dissolution of QDs. The amount of HgSe cores remaining is therefore 4.8 mg. The subsequent volumes of Se- and Cd- additions are calculated to account for this change in size and HgSe amount.

Fig. 4.9 is an example of the volumes added for an 8mg scale of HgSe:

Temperature (°C)	Time (min)	HgSe Mass (mg)	Precursor	Inject vol (mL)	Total vol (mL)	Final Size (nm)
					3.10	7.00
150	0	8	4Se	0.28	3.38	7.35
150	5	8	4Cd	0.31	3.69	10.45
150	7	3.2	5Se	0.25	3.93	10.80
150	12	3.2	5Cd	0.26	4.19	11.15
200	14	3.2	6Se	0.28	4.47	11.50
200	16	3.2	6Cd	0.30	4.77	11.85
200	18	3.2	7Se	0.31	5.08	12.20
200	20	3.2	7Cd	0.33	5.41	12.55
200	22	3.2	8Se	0.35	5.77	12.90
200	24	3.2	8Cd	0.37	6.14	13.25

Figure 4.9: Calculation of Cd- and Se- precursor volumes during growth of thick shell HgSe/CdSe QDs.

Synthetic protocol

The following protocol started with HgSe/3CdSe QDs containing 8 mg of HgSe. The fraction of QDs dissolved during the initial heat-up step was sensitive to the reaction scale.

HgSe/3CdSe stock solution from the freezer was fully thawed. A measured volume of the

solution (containing 8 mg of HgSe) was added to a 3-neck flask, equipped with a stir bar, rubber sleeves, a thermocouple, and connected to a Schlenk line. The solution was heated to 150°C. A certain fraction (typically ∼60%) of the QDs dissolved during the heat-up stage, and deposited as an alloyed HgCdSe on the remaining QDs.

The Cd- and Se- precursor solutions were kept ready with 1 mL syringes. The Se-suspension was kept on the sonicator, and mixed vigorously before adding the desired volume of precursor.

On reaching the set temperature, the Se precursor was added, and left to react for 5 minutes. The Cd precursor was then added, and left to react for 2 minutes. At this stage, the QD diameter was typically ∼10.5 nm.

One more Se- and Cd- cycle was performed. After the Cd addition, the temperature was set to 200°C. Further Se- and Cd- cycles were performed, with a reaction time of 2 minutes for each cycle. Aliquots were taken if necessary, using a glass syringe with a metal cannula. Aliquots were rinsed with equal volume of TCE to collect residual solution in the syringe. The QDs diameters increased by roughly 0.7 nm per SeCd cycle. After ∼13 nm, the QDs start to develop a tetrahedral-like morphology with a possibility of independent nucleation unless the reaction temperature is increased.

Aliquots were purified by two cycles of precipitation – dissolution before characterization:

All purifications were performed in air at ambient conditions. The solution was centrifuged, leading to precipitation of a fraction of the QDs (which increased with the QD size). If QDs remained in the supernatant, 0.1M DDAB/TCE was added (0.1× volume of solution), and the solution was precipitated by addition of IPA and centrifugation. The QDs precipitated in fractions (likely due to broad size distribution), and it was necessary to performed several IPA additions and centrifugations to completely precipitate the QDs. The supernatant was discarded, and the precipitate was dispersed in TCE, leading to a concentration of ∼5 mg/mL of HgSe. 0.1M DDAB/TCE was added (0.1× volume of TCE),

and the solution was precipitated by addition of IPA and centrifugation. Precipitation of several fractions was observed, and the QDs were fully precipitated. The supernatant was discarded, the precipitate was lightly dried by blowing nitrogen, and then dispersed in TCE for characterization.

4.7.6 Influence of Cd- and Se- cycles on doping and PL of HgSe/CdSe QDs

To decide between ending the HgSe/CdSe synthesis with a Cd- or Se- cycle, we tested the effect of the final cycle on the doping and the PL of the QDs. Thick shell HgSe/CdSe QDs with a final diameter of ∼10-12 nm were synthesized at 180°C. An aliquot was taking after a Se- cycle. Different amounts of Cd- were then added (corresponding to 1, 2 and 3 surface equivalents of Cd), with aliquots between additions. Partial independent nucleation was observed, but this should not affect the conclusions of these trials.

The QDs were purified twice by precipitation-dissolution, before redispersing in TCE. The final solutions were characterized by FTIR absorption and PL spectroscopy (Fig. 4.10). A slight decrease in the n-doping was observed after Cd- treatment, but the PL was much stronger for the Cd- samples compared to the Se- sample. This motivated us to stop the HgSe/CdSe syntheses at the Cd- cycle.

4.7.7 Effect of synthesis temperature on dissolution, alloying, and morphology of HgSe/CdSe QDs

The synthesis temperature was crucial to the morphology of the HgSe/CdSe QDs. If the temperature was too low, the onset of independent nucleation was observed at smaller QD sizes (Fig. 4.11). If the temperature was too high, alloying at the core/shell interface was observed, with a blueshift in the absorption and PL (Fig. 4.12). Smaller sized cores emitting at 5800 cm^{-1} showed core/shell interface alloying at 220°C. We thus set the optimal synthesis temperature as 200°C to achieve large shell thicknesses while avoiding interfacial alloying.

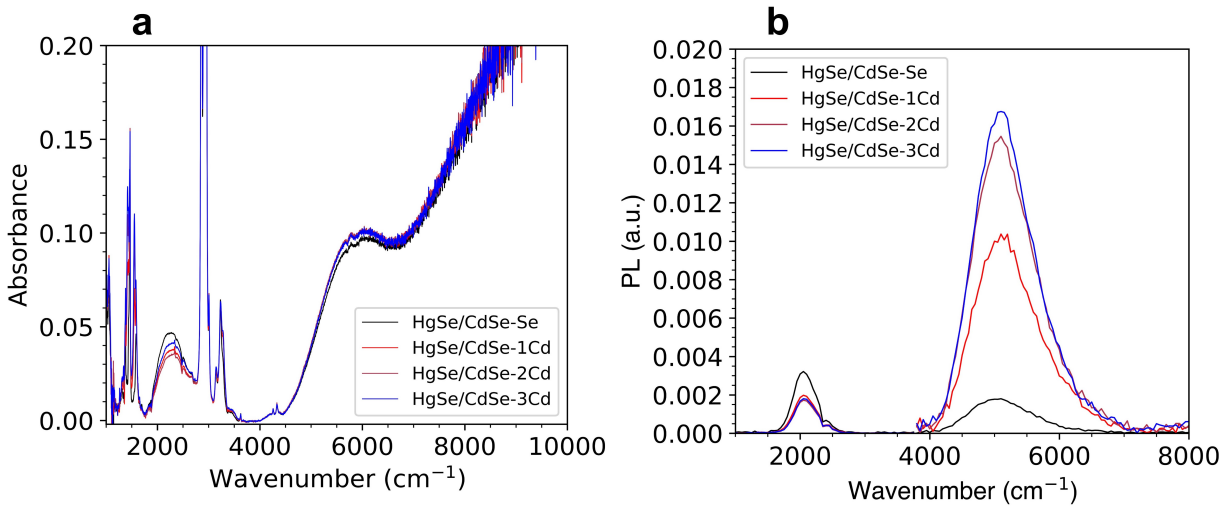

Figure 4.10: Effect of Se- and Cd- half cycles on absorption and PL of ∼10-12 nm HgSe/CdSe QDs. Testing thermal stability of: a, HgSe QDs and b-d, HgSe/CdSe QDs with different number of shell monolayers. Samples are the same as in Fig. 4.6.

4.8 Characterizations

4.8.1 Particle size characterization by TEM and SAXS measurements

Transmission Electron Microscopy (TEM) images were recorded using an FEI Spirit 120kV electron microscope and an FEI Tecnai F30 300kV microscope. Samples were prepared by dropcasting the purified QD solution in TCE on a Formvar/Carbon 200 mesh grid (Ted Pella 01801), and evaporated in a vacuum pump before performing measurements. The QD size was determined using imageJ software, by visually estimating the boundary of ∼100 nanoparticles, measured along a single orientation for consistency.

Small Angle X-Ray Scattering (SAXS) measurements were performed using a SAXSLAB GANESHA instrument. The sample was prepared in a Kapton capillary tube and sealed.

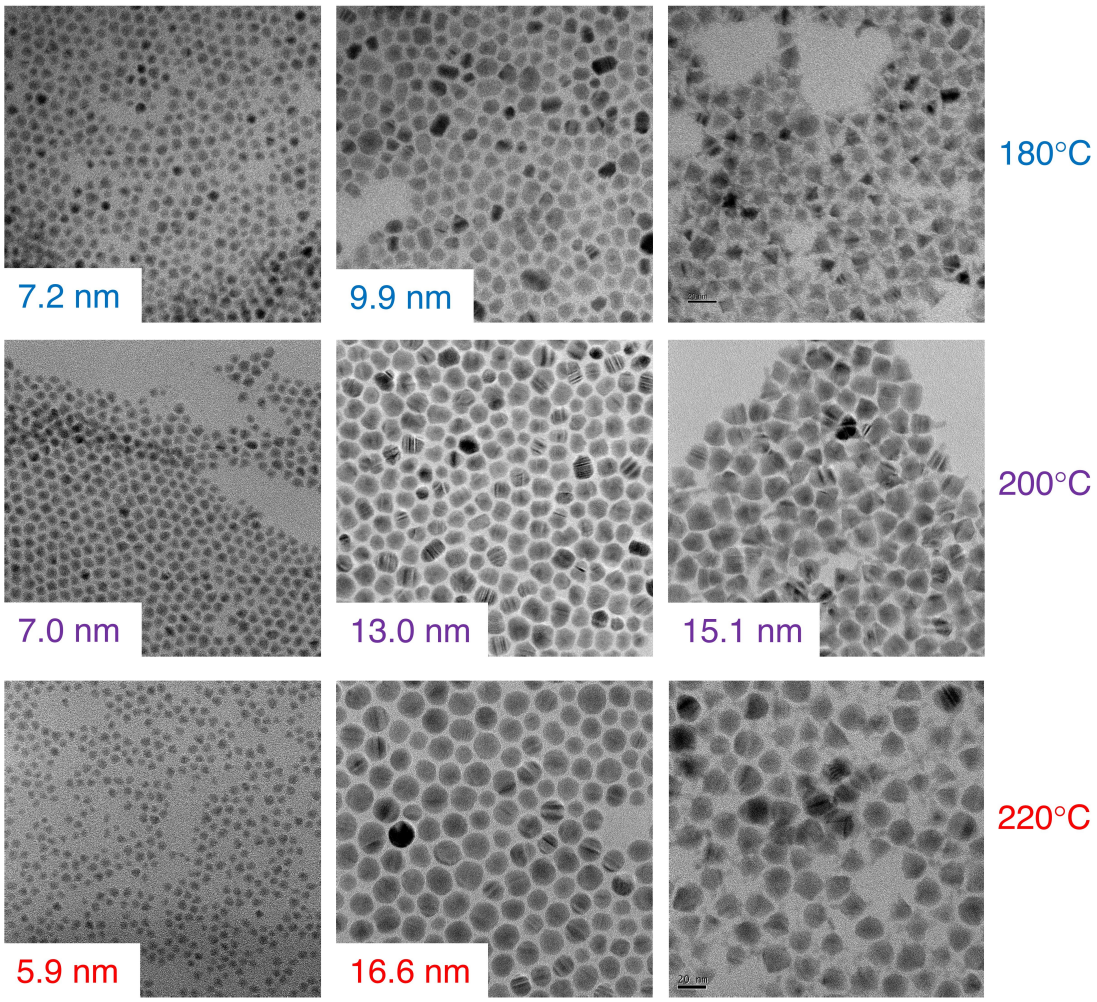

Figure 4.11: Effect of synthesis temperature on the onset of independent nucleation. The onset of independent nucleation at 180°C, was at a size around 10 nm; at 200°C it was ∼15 nm, and at 220°C it was ∼17 nm.

4.8.2 Absorption measurements

UV-NIR absorption measurements in the 300 nm – 2500 nm range were performed using an Agilent Cary 5000 UMA Spectrophotometer. Samples were prepared in a glass cuvette with 1 cm path length, using TCE as the solvent.

FTIR absorption measurements in the 1600 nm – 10,000 nm range were performed using a ThermoNicolet iS50 spectrometer. Samples were prepared in a cell with CaF_2 windows with 0.5 mm path length, using TCE as the solvent. FTIR measurements allowed a quantitative

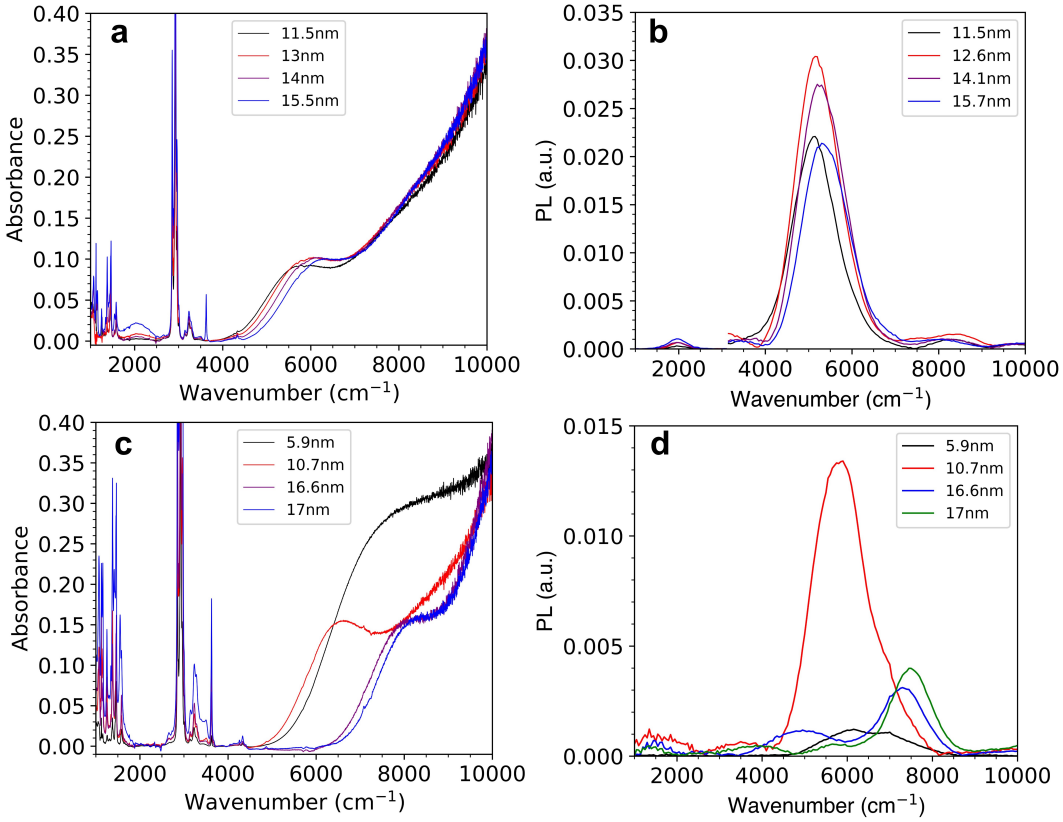

Figure 4.12: Core/shell interface alloying at 220°C, for HgSe/CdSe QDs emitting at different frequencies. The red curve shows the shell grown at 150°C, and the thicker shell samples are grown at 220°C a-b, Absorption and PL of HgSe/CdSe QDs emitting at 5100 cm^{-1}. There is a small, but insignificant blueshift in the absorption and PL during subsequent stages of shell growth at 220°C. c-d, Absorption and PL of HgSe/CdSe QDs emitting at 5800 cm^{-1}. There is a large blueshift in the absorption and PL on heating to 220°C, which indicates alloying at the core/shell interface. This shows that the smaller cores have a lower temperature for alloying at the core/shell interface.

determination of the amount of HgSe cores in aliquots.

4.8.3 Photoluminescence and PLQY measurements

PL spectra

Samples were prepared in a cell with CaF_2 windows with 0.5 mm path length, using TCE as the solvent. Photoluminescence (PL) spectra were recorded using a step-scan FTIR spectrometer with an MCT detector and a gated integrator. The samples were excited with a

15mW 808nm diode laser, modulated at 90 kHz. A Si wafer was placed in front of the detector to block the excitation light. The transmittance of the solution at 808nm was measured using a Si diode detector behind the sample cell. The spectra were corrected for the combined optics/spectrometer/detector combined response, which was determined by measuring the spectrum of a 1268 Kelvin blackbody at the sample position. The PL spectra were normalized by the fraction of 808 nm light absorbed, and were also corrected for the absorption by TCE. The PLQY could be calculated as the area under the corrected PL spectrum, by comparing to the measured PLQY of a reference sample. Since the spectrometer sensitivity in the 4000 – 8000 cm^{-1} was weak, the PLQYs determined this way had an uncertainty of a factor of $\sim$2.

Absolute PLQY measurements

Setup and sample preparation:

Absolute PLQY measurements were performed on QD solutions in TCE in a home-built CaF_2 cuvette with a path length of $\sim$3mm. The concentration of the solution was adjusted to keep the absorption of the 808 nm light between 20% - 80%, to provide adequate signal, while avoiding reabsorption of the PL (see Fig. 4.13). The cuvette area is 0.65 cm^2, smaller than the 1.2 cm^2 input port in order to minimize indirect re-absorption of incident and emitted light in the integrating sphere.

The sample was placed in a Spectralon integrating sphere (Thorlabs IS200-4), with the 808 nm laser excitation at one port, with a PbSe detector (Thorlabs PDA20H) and Si diode detector at perpendicular ports (see Fig. 4.13). The 808 nm laser was modulated as a square wave at 1kHz, with average power of 15mW. PLQYs measured at 150mW excitation were roughly $\sim$15% lower than 15mW excitation, likely due to localized heating at the laser spot.

Direct reflection of the excitation light into the PbSe or Si detectors is avoided as this leads to abnormally high signals. The measurements are performed in two geometries: the 'N'

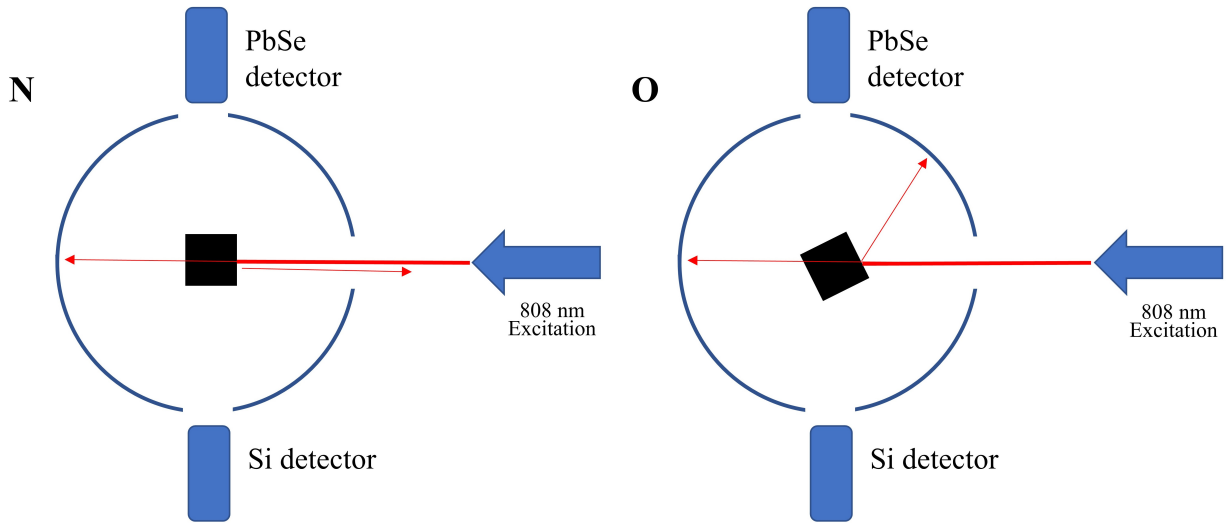

Figure 4.13: Schematic of PLQY measurements in a Spectralon integrating sphere. The cuvette was oriented in two angles: the 'N' (normal) geometry and the 'O' (oblique) geometry.

geometry, where the CaF_2 cuvette is normal to the excitation laser, and the light reflected off the cuvette is sent out of the integrating sphere. In the 'O' geometry, the cuvette is rotated at an angle, so that the reflected excitation light is incident on a wall of the integrating sphere. To precisely obtain the N geometry, the cuvette is first oriented visually to make the face parallel to the excitation light, and is rotated until the signal on the PbSe detector is at a minimum. To obtain the O geometry, the cuvette is rotated until the signal on the PbSe detector is relatively insensitive to the cuvette orientation. If the cuvette is further rotated, a drastic increase in the PbSe signal is observed, which indicates direct reflection of the excitation light to the detector. By such control of the cuvette orientation, we obtained PLQY measurements with a relative error of only $\sim$3%. Measurement:

A blank TCE solution is placed in the integrating sphere in the N geometry. The signal on the Si detector is N_{Si} (TCE), and the signal on the PbSe detector is N_{PbSe}(TCE). A silicon wafer is then placed in front of the PbSe detector to block the 808 nm excitation, giving a signal of N_{PbSe-B} (TCE). Similarly, the signals in the O geometry are O_{Si} (TCE), O_{PbSe} (TCE), and O_{PbSe-B} (TCE) respectively. The signals N_{PbSe-B} (TCE) and O_{PbSe-B}

(TCE) should be zero in principle, but a small ∼25 mV signal is observed, which sets the lower bound for the PLQY that can be measured with this setup.

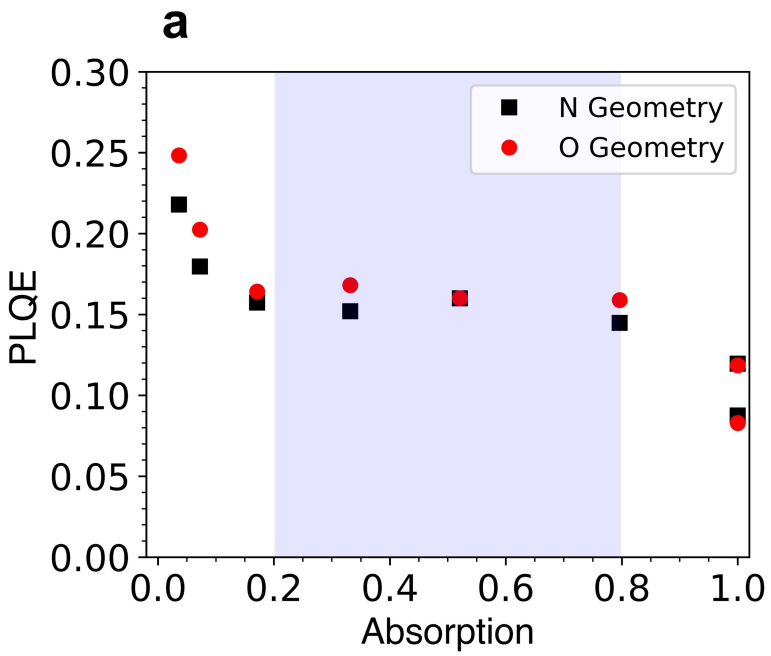

b

Absorption	PLQE
4%	21.8%
7%	18.0%
17%	15.7%
33%	15.2%
52%	16.0%
80%	14.5%
99.998%	12.0%
99.999%	8.8%

Figure 4.14: a, Effect of the absorption (at 808 nm) on the measured PLQE. At absorption $>\sim$ 0.8, the sample reabsorbs the PL light emitted along the excitation direction, and leads to underestimation of the PLQE. At a very high absorption, the measured PLQE saturates to half of the actual value. At absorption $<\sim$0.2, the PL signal is low and comparable to the signal from the blank TCE sample, and leads to overestimation of the PLQE. The PLQE measurement is accurate when the absorption is between 0.2 – 0.8, denoted by the shaded region. b, Data for PLQE vs absorption for the 'N' geometry.

The QD solution is then placed in the integrating sphere and measurements are performed in the two geometries. PbSe is a photon detector with a close to linear response (V/W) throughout the 800 nm – 4000 nm range, therefore the signal is taken to be directly proportional to the photon count.

The 'N' and 'O' geometries provided two measurements of the PLQY.

For the N-geometry, the signal from the laser excitation for the clean TCE cell is:

$$Excitation \ = \ N_{PbSe}(TCE) \tag{4.3}$$

This comes from the laser light scattering from the sphere and some of that light getting to the detector.

N_{PbSe-B} (QD) is the signal arising from emission of the sample. Taking into account the transmittance of Si is 56% in the 1.3 µm – 5 µm range, the QD emission signal is:

$$Emission \ = \ \frac{N_{PbSe-B}(QD)}{0.56} \tag{4.4}$$

The QD absorption is determined by subtracting the emission signal from the PbSe signal such that

$$Absorption \ = \ 1 - \frac{N_{PbSe}(QD) - \frac{N_{PbSe-B}(QD)}{0.56}}{N_{PbSe}(TCE)} \tag{4.5}$$

The QD absorption is independently determined from the signal on the Si diode:

$$Absorption \ = \ 1 - \frac{N_{Si}(QD)}{N_{Si}(TCE)} \tag{4.6}$$

The absorptions determined from both measurements were close, with a relative standard deviation of <10%

The PLQY is then determined as:

$$PLQY = \frac{Emission}{Absorption \times Excitation} \tag{4.7}$$

A similar calculation was done for the 'O' geometry. Measurements in the two independent geometries provided PLQY values that are close, with a relative standard deviation <3%. We used this is as the uncertainty in the absolute PLQY measurement. Additional uncertainty could arise from a nonlinear response curve for the PbSe diode detector.

4.8.4 Photoluminescence lifetime measurements

Photoluminescence lifetime measurements were recorded using time-correlated single photon counting for samples in a 1 mm cuvette dispersed in TCE. Samples were excited with a Picoquant 50 ps pulsewidth laser diode operating at 976 nm and 1 MHz repetition rate. PL was collected with a lens, directed through a silicon longpass filter, dispersed in a 0.3 m spectrograph set to pass the PL emission maximum, and detected with a Quantum Opus superconducting nanowire single photon detector. Single photon arrival times were collected as a histogram for 300 s with a timing bin resolution of 200 ps.

4.8.5 X-Ray Diffraction Measurements

X-Ray Diffraction (XRD) measurements were performed using a Rigaku Miniflex Benchtop spectrometer. Samples were dropcasted on a silicon holder. Peak fitting was performed using the Rigaku SmartLab Studio II software. The background of the spectrum was calculated as a polynomial, and the peaks were fit to Split pseudo-Voigt functions.

The pXRD spectra for bulk zincblende HgSe and CdSe were simulated using the software Diamond 3.2, using lattice constants of 6.08 Å and 6.05 Å respectively.

4.9 Calculations and analyses

4.9.1 Dissolution of thin shell HgSe/CdSe QDs and deposition of HgCdSe shell

During the heat-up of thin shell HgSe/CdSe QDs to 150°C, we noticed the measured QD size to be much larger than the calculated size. This was accompanied by a decrease in the HgSe absorption (as determined by quantitative FTIR spectra of aliquots). We attributed this to dissolution of a fraction of the HgSe/CdSe QDs, and deposition on the remaining QDs as a HgCdSe shell. The absorption and PL of the surviving QDs were not affected by the dissolution. Estimation of the dissolution fraction is shown below:

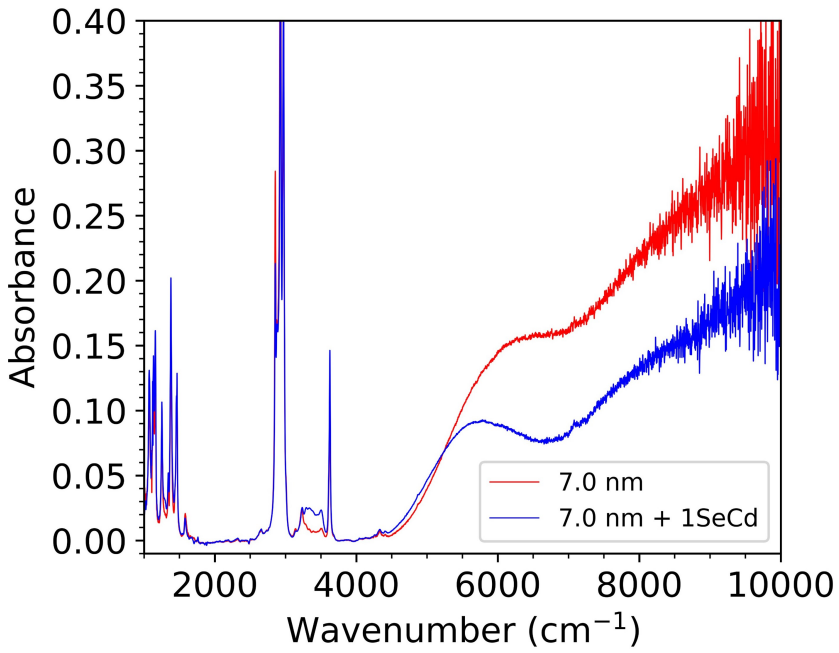

Figure 4.15: FTIR absorption spectra of thin shell HgSe/CdSe before (red) and after (blue) performing one Se-Cd cycle. The HgSe absorption decreases by ∼41%.

A solution of 7.0 nm thin shell HgSe/CdSe QDs (containing 2mg of HgSe, measured by absorption at 700 nm) was cleaned and the FTIR spectrum was recorded. A reaction mixture of thin shell HgSe/CdSe (containing 8mg of HgSe) was heated to 150°C and one

Se-Cd- cycle was performed (see Section 4.7.5). A quarter of the reaction mixture was taken as an aliquot, purified twice, and an FTIR spectrum was recorded.

The ratio of absorbance at 8000 cm^{-1} is 0.13 / 0.22 = 0.59, which suggests that 41% of the initial QDs are dissolved.

As an independent measure of the dissolved fraction, we calculated the discrepancy between the measured and calculated TEM size. The expected size after growth of one SeCd cycle is 7.7 nm, while the measured size was 10.2 nm (measured by SAXS). This suggests that the fraction of surviving QDs is $\left(\frac{7.7}{10.2}\right)^3 = 0.43$, which suggests that 57% of the initial QDs are dissolved. This estimate qualitatively agrees with the decrease in the intensity of the HgSe absorption.

4.9.2 Estimating PLQY of partially doped HgSe and HgSe/CdSe QDs

The HgSe and 15.1 nm HgSe/CdSe QDs were observed to be partially n-doped, as seen from the intraband absorption (Fig. 4.16) and presence of both interband and intraband emission (see Section 4.10.1). It is necessary to determine the doping fraction in order to calculate the interband PLQY. We followed the procedure by Kamath et. al. [38] to measure the doping. The absorption spectrum of the QD sample in TCE was first measured, after which the PL spectrum was recorded. The doping of the sample would typically increase after the PL measurement, likely due to photochemical processes on excitation with the 808 nm laser. The spectra were subtracted to yield the intraband absorption and interband bleach (Fig. 4.16, blue). This curve was used to extrapolate the HgSe absorption to determine the intraband absorption for a fully n-doped sample.

One way is to add the blue spectrum to the HgSe absorption, till the interband edge appears flat. This gives the lower limit on the intraband absorbance of a fully n-doped sample (Fig. 4.16, green). Another way is to add the blue spectrum to the HgSe spectrum till the absorbance at the interband peak (6000 cm^{-1}) is zero. This gives the upper limit

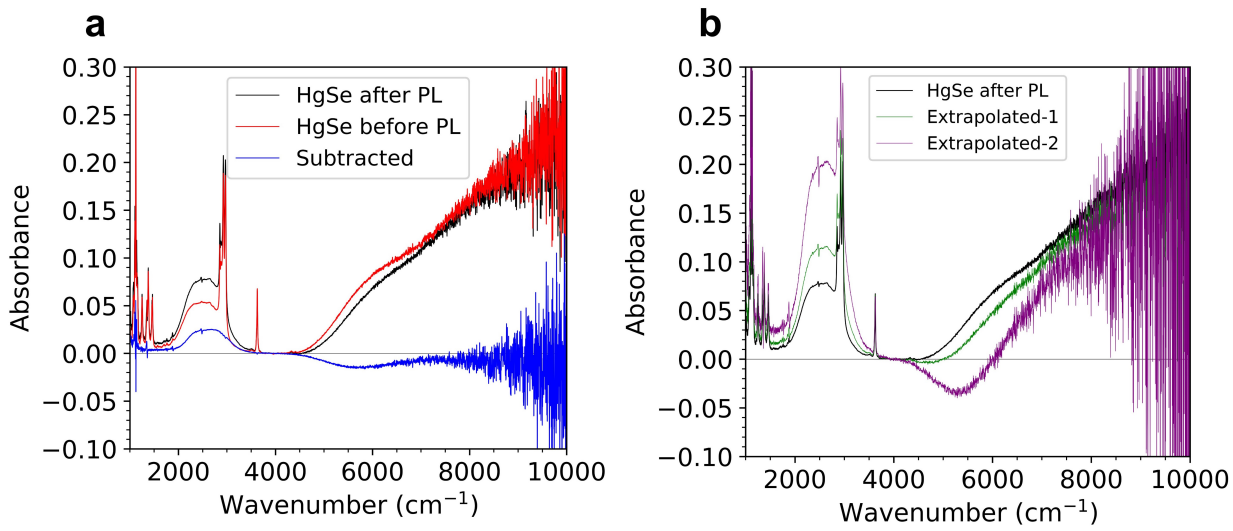

Figure 4.16: Estimating the doping of HgSe QDs. a, Absorption spectra of HgSe QDs in TCE before (red) and after (black) PL measurement. The spectra are subtracted (blue) to obtain the intraband absorption and interband bleach. b, The blue curve from (a) is added to the HgSe spectrum till the interband edge appears to be flat (green), or gives zero absorbance at 6000 cm^{-1} (purple).

to the absorbance of a fully n-doped sample (Fig. 4.16, purple). The $1S_e$ occupancy was then calculated to be ratio of the intraband peak absorbance of the HgSe spectrum to the extrapolated spectrum. The lower and upper limit on the $1S_e$ occupancy was determined to be 0.77 and 1.3 electrons/QD respectively. The average doping was thus found to be 1.04 electrons / QD.

Assuming a binomial distribution for QDs with 0, 1 and 2 electrons in the $1S_e$ state (denoted $1S_e(0)$, $1S_e(1)$ and $1S_e(2)$ respectively), the fraction of QDs in $1S_e(0)$ was calculated as [38]:

$$(1S_e(0)\ fraction\ =\ \left(1-\left(\frac{N_e}{2}\right)^2\right) \tag{4.8}$$

Where N_e is the average number of electrons in $1S_e$. Using $N_e = 1.04$, we get the average $1S_e(0)$ occupancy is 23%, with lower and upper limits 12% and 38% respectively.

For 15.1 nm HgSe/CdSe, a similar subtraction was performed. Since the doping did not decrease after PL measurement, we used the absorption spectrum of the 13.0 nm sample, which was completely undoped. Since the QD absorption shapes were identical (except for the ligand absorption), we could perform a reliable subtraction using the two different samples (Fig. 4.17). Similar to the HgSe sample, the blue curve was added to the 15.1 nm HgSe/CdSe QD absorption to determine the lower and upper limits on the absorption of a fully n-doped sample. The lower and upper limit on the $1S_e$ occupancy was determined to be 0.76 and 0.93 electrons/QD respectively. The average doping was thus found to be 0.85 electrons / QD.

Using $N_e = 0.85$ (Eq. S3B-1), we get the average $1S_e(0)$ occupancy is 33%, with lower and upper limits 29% and 38% respectively.

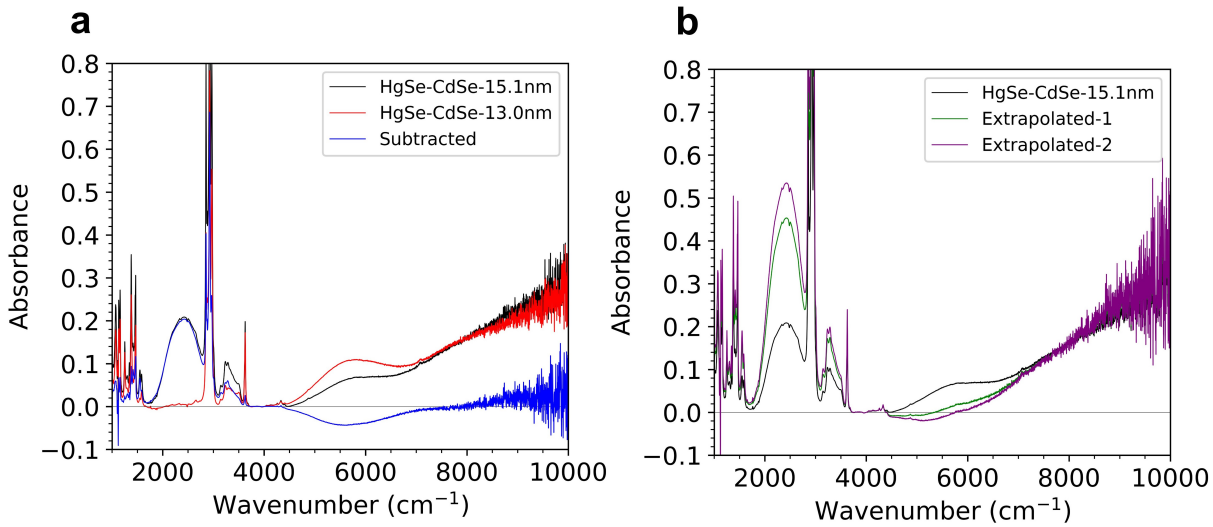

Figure 4.17: Estimating the doping of 15.1 nm HgSe/CdSe QDs. a, Absorption spectra of HgSe/CdSe QDs with sizes 15.1 nm (black) and 13.0 nm (red). The spectra are subtracted (blue) to obtain the intraband absorption and interband bleach. b, The blue curve from (a) is added to the 15.1 nm HgSe/CdSe spectrum till the interband edge appears to be flat (green), or gives zero absorbance at 5800 cm^{-1} (purple).

The PLQY was calculated by dividing the measured PLQE (see Section 4.10.1, 4.10.2) by 0.23 (for HgSe) and 0.33 (for 15.1 nm HgSe/CdSe). The error bar limits (in Fig. 4.3a) were set using the lower and upper limits for the $1S_e(0)$ occupancy.

4.9.3 Imaginary dielectric function of ligands and solvents

The absorption spectra of oleylamine, dodecanethiol, chloroform, octane and water were measured in the 750 nm – 2500 nm range. The spectra were recorded using TCE as a background, since the absorption is negligible in this wavelength range.

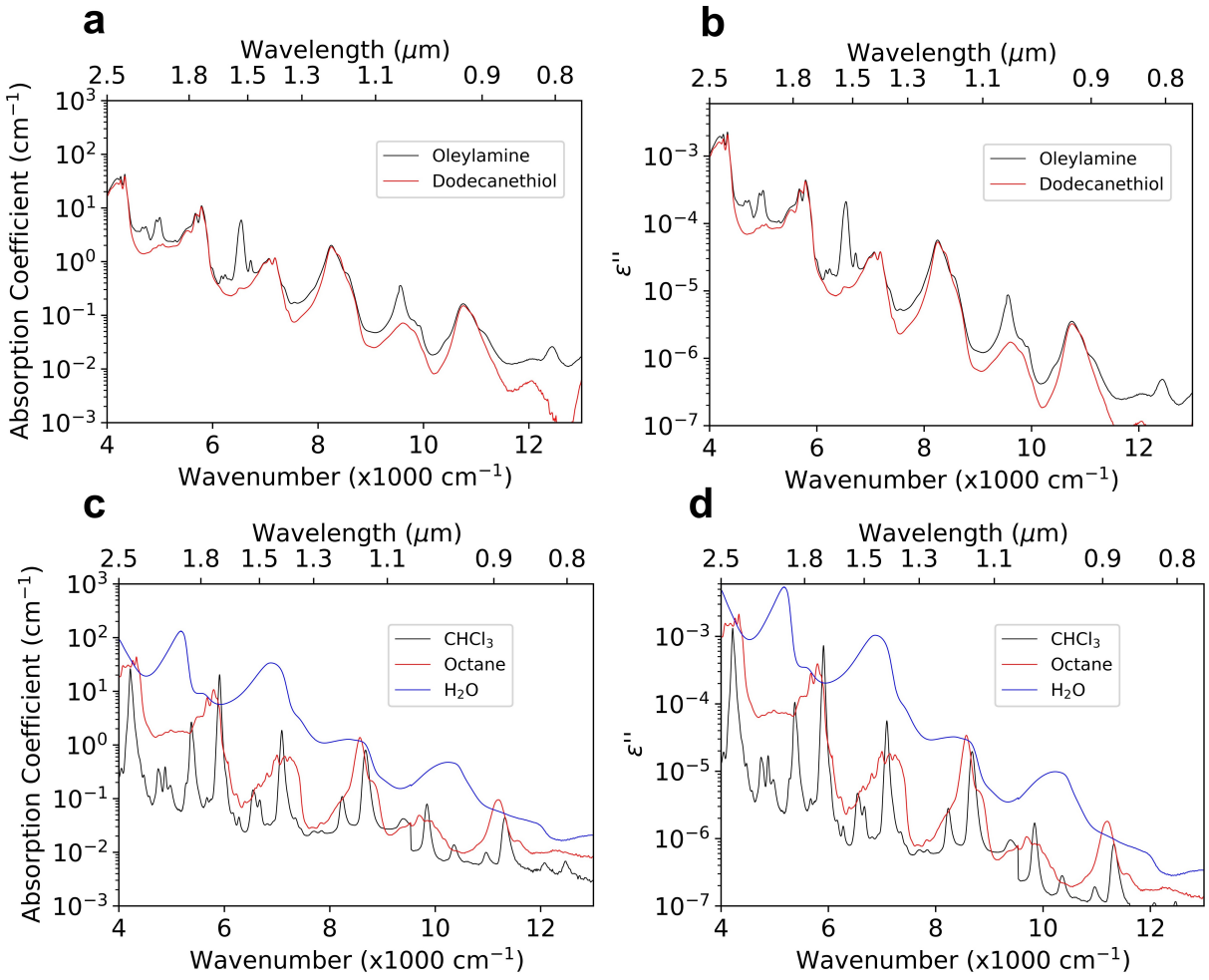

Figure 4.18: a,c, Absorption coefficient and b,d, imaginary refractive index of ligands (a,b) and solvents (c,d). The absorption of oleylamine and dodecanethiol are similar, as they are dominated by C-H overtone and combination bands.

For oleylamine, spectra were recorded in a 1 cm cuvette. Accurate spectra were obtained at absorbance $>\sim$0.01 (due to reflection from index difference of TCE and oleylamine) and $<$2 (due to spectrometer sensitivity). To obtain accurate spectra, we recorded absorptions

of 3 concentrations of oleylamine in TCE (100% OAm, 10% OAm and 1% OAm), scaled the absorptions of the diluted samples, and stitched the overlapping areas. Spectra of different concentrations were also recorded in the 1.6 µm - 10 µm range using an FTIR spectrometer.

For dodecanethiol, chloroform, octane and water, we recorded spectra in a 1 cm cuvette and 1 mm cuvette (absorption scaled 10x), and stitched the overlapping areas.

The measured absorbance A for a 1 cm cell was used to calculate the absorption coefficient α by:

$$\alpha \;=\; \frac{A\ ln(10)}{l} \;=\; 2.303\ A\ cm^{-1} \tag{4.9}$$

The imaginary index of refraction ϵ'' was calculated by:

$$\epsilon'' \;=\; \frac{\alpha n \lambda}{2\pi} \tag{4.10}$$

Where n is the real refractive index and λ is the vacuum wavelength. The data are presented in Fig. 4.18.

Fig. 4.18(a,b) shows that the absorption from oleylamine and dodecanethiol are similar, and mainly determined by the C-H overtones.

4.9.4 Calculation of FRET-limited PLQY

The rate of Forster Resonance Energy Transfer (FRET) from the QD to the ligands is well-described in the supplementary information of Liu. Et. al. [138] and Melnychuk [18]. The nonradiative FRET rate $\gamma_{NR_{ligand}}$ is directly proportional to the radiative rate γ_R, and the ratio is calculated to be (Eq. 1.3 in Melnychuk) [18]:

$$\frac{\gamma_{NR_{ligand}}}{\gamma_R} = \frac{3\epsilon''}{32\pi^3 n\bar{\nu}^3}\int_R^{R+\Delta R}\frac{dr}{r^4} \tag{4.11}$$

Where ϵ'' and n are the imaginary and real indices of refraction for the ligand / solvent, $\bar{\nu}$ is the wavenumber, R is the total nanocrystal radius and ΔR is the thickness of the ligand shell. Eq. S3D-1 was performed at a single frequency. For a QD with a given absorption spectrum, the ratio of nonradiative to radiative rates can be calculated as:

$$\frac{\gamma_{NR_{ligand}}}{\gamma_R} = \frac{3}{32\pi^3 n}\int_R^{R+\Delta R}\frac{dr}{r^4}\int\frac{\epsilon'' f_D(\bar{\nu})d\bar{\nu}}{\bar{\nu}^3} \tag{4.12}$$

Where $f_D(\bar{\nu})$ is the normalized QD emission spectrum ('D' stands for 'donor', using the terminology of FRET literature).

The photoluminescence quantum yield (PLQY) could be calculated by:

$$PLQY = \frac{\gamma_R}{\gamma_R + \gamma_{NR}} = \frac{1}{1+\frac{\gamma_{NR}}{\gamma_R}} \tag{4.13}$$

The magnitude of ϵ'' depends on the surface density of ligands on the QD surface. We used the surface density of oleylamine ligands on a CdSe surface as 1.8 nm^{-2} following the report by Owen and coworkers [139]. To determine the ϵ'' for a surface density of 1.8 nm^{-2} , we estimated the surface density if the oleylamine ligand shell had the volume density of bulk oleylamine. Using the density of oleylamine as 0.813 g/cm^3 , molar mass as 267.5 g/mol, and oleylamine ligand length = 1.8 nm [138], we estimated the surface coverage to be 4.3 nm^{-2} on a QD of diameter 13 nm. Hence, we scaled the bulk oleylamine ϵ'' by 0.18/4.3 to account for the reported surface coverage.

To calculate the FRET rate to solvent molecules, Eq. S3D-2 was used, but using the ϵ'' for the solvent absorption, and performing the integration from R+ΔR to infinity.

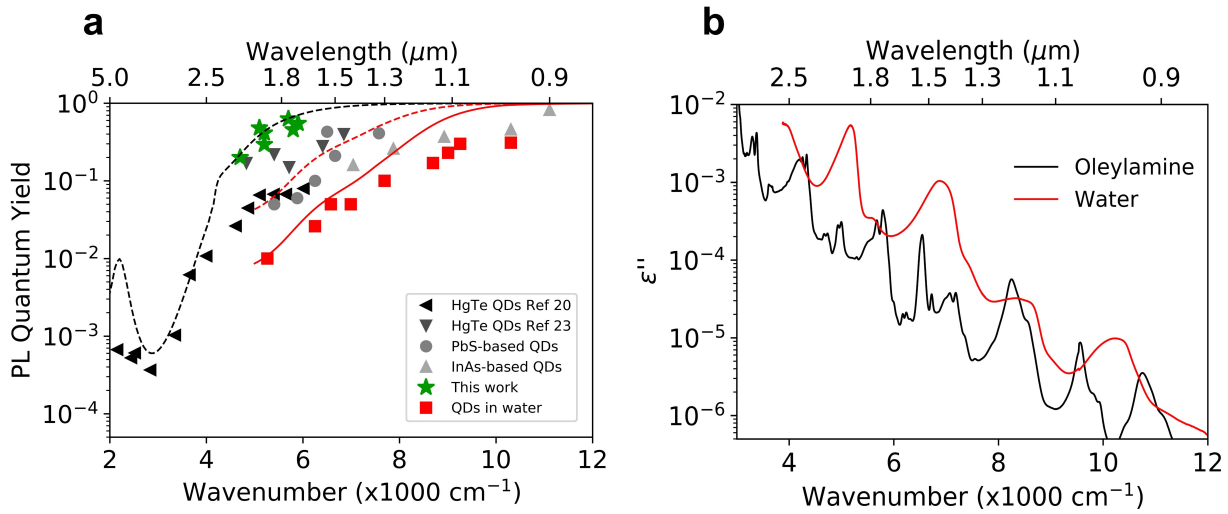

Figure 4.19: a, Compilation of PLQYs of the brightest reported QDs at different emission wavelengths (see main text for references and details). The curves are calculated PLQY by FRET to oleylamine ligands in TCE (black), and water (red). Solid curve is for 6 nm diameter QDs, and dashed curve is for 13 nm diameter QDs.b, Measured imaginary refractive index of oleylamine and water at a function of frequency.

$$\frac{\gamma_{NR_{solvent}}}{\gamma_R} = \frac{3}{32\pi^3 n}\int_{R+\Delta R}^{\infty}\frac{dr}{r^4}\int\frac{\epsilon'' f_D(\bar{\nu})d\bar{\nu}}{\bar{\nu}^3} \tag{4.14}$$

This integral range was appropriate for QDs in both nonpolar solvents as well as water. This is because QDs for in-vivo imaging are usually overcoated with amphiphilic ligands to impart water solubility, without affecting the original ligand shell [9, 11]. ΔR was set to be 1.8 nm for oleylamine ligands (following Liu et. al.) [138]. The QD emission spectrum was simulated as a Gaussian with standard deviation as 0.1 times the emission frequency, which was a good approximation for HgSe QDs emitting at 5 µm (intraband) and 2 µm (interband).

4.9.5 PLQY in different solvents

To experimentally validate our model of FRET to solvent molecules, we have performed PLQY measurements of HgSe/CdSe in organic solvents with varying solvent absorption. TCE, $CHCl_3$ and octane were chosen as the solvents due to their ability to disperse the oleylamine-capped QDs without affecting the ligand shell. This avoided possible aggregation of QDs which would complicate the analyses. The solvent quenching is expected to increase between TCE, $CHCl_3$ and octane, as seen from the solvent absorption in Fig. 4.18(c). Since TCE exhibits negligible absorption in the QD emission wavelength, the difference in PLQY in TCE and the other solvents can be used to measure the FRET to solvent molecules in $CHCl_3$ and octane.

HgSe/CdSe QDs with a diameter of 9.5 nm and emission peak at 5700 cm^{-1} were synthesized following the protocol in Section 4.7.5, starting with 8mg HgSe. The QDs were purified twice by precipitation / dissolution, but using octane as the solvent instead of TCE. Half of the QD solution ($\sim$1.6mg cores, assuming 60% dissolution during shell growth) were finally dispersed in $\sim$0.05 mL of octane to obtain a concentrated solution. The high concentration was necessary to minimize solvent reabsorption during PL measurements.

The PL spectra was measured in a CaF_2 cell with path length $\sim$3 mm. The solution was evaporated using a nitrogen line before dispersing in the next solvent. The QDs were colloidally stable, and showed no visual change between measurements. PL spectra were recorded in octane, TCE and $CHCl_3$ in that order. The PLQY is determined by measuring the absolute PLQY of a dilute solution in TCE, and comparing the area under the PL spectrum against this reference sample. The results are shown in Fig. 4.20. A steady decreasing trend is observed in the PLQY, which shows good agreement with the simulations. The FRET rate to solvents agrees well with the simulations, but the FRET rate to ligands is measured to be $\sim$2.5 times slower than simulated (Fig. 4.20(c)). This could arise due to the uncertainty in composition of the ligand shell. A lower ligand density, and presence of

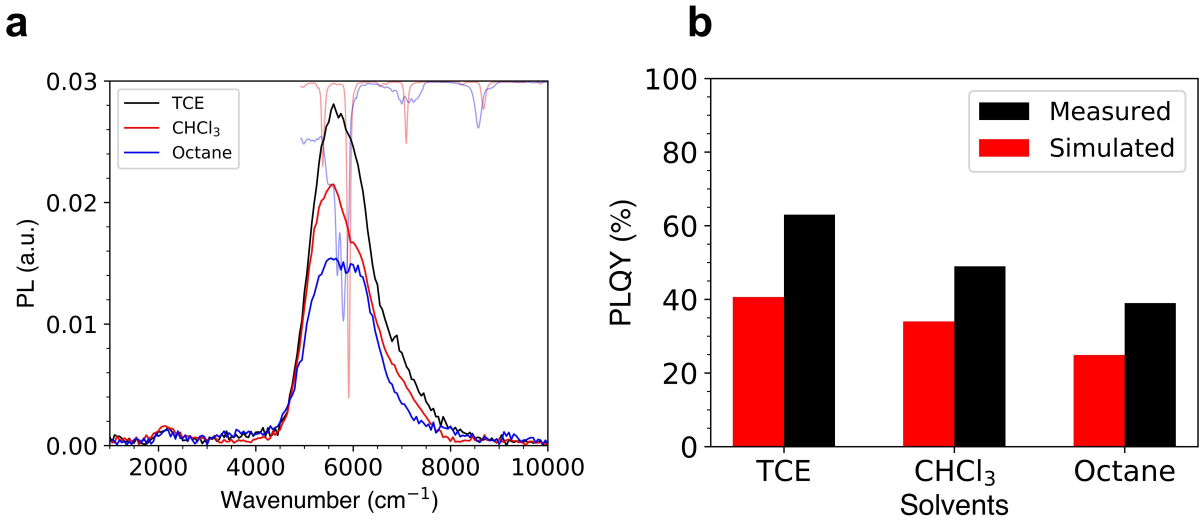

c

Solvent	PLQY	$\gamma_{nr\text{-}total}/\gamma_r$	$\gamma_{nr\text{-}ligand}/\gamma_r$		$\gamma_{nr\text{-}solvent}/\gamma_r$	
	Measured	Measured	Measured	Simulated	Measured	Simulated
TCE	63%	0.59	0.59	1.5	0	0
$CHCl_3$	49%	1.0	0.59	1.5	0.46	0.48
Octane	39%	1.6	0.59	1.5	0.99	1.6

Figure 4.20: a, Measured PL spectra (opaque) of HgSe/CdSe QDs in different solvents, overlayed with (translucent) transmission spectra of the solvents (arbitrary scale). b, Comparison of measured and simulated PLQY in different solvents. c, Comparison of measured and simulated nonradiative rates to ligands and solvent. The measured FRET to ligands is ∼2.5 times slower than simulated, but the measured FRET to solvent shows a good agreement with simulations.

smaller ligands like acetate could lead to a lower ligand FRET rate than calculated. Though the agreement is not exact, the PLQY trend supports our FRET nonradiative model.

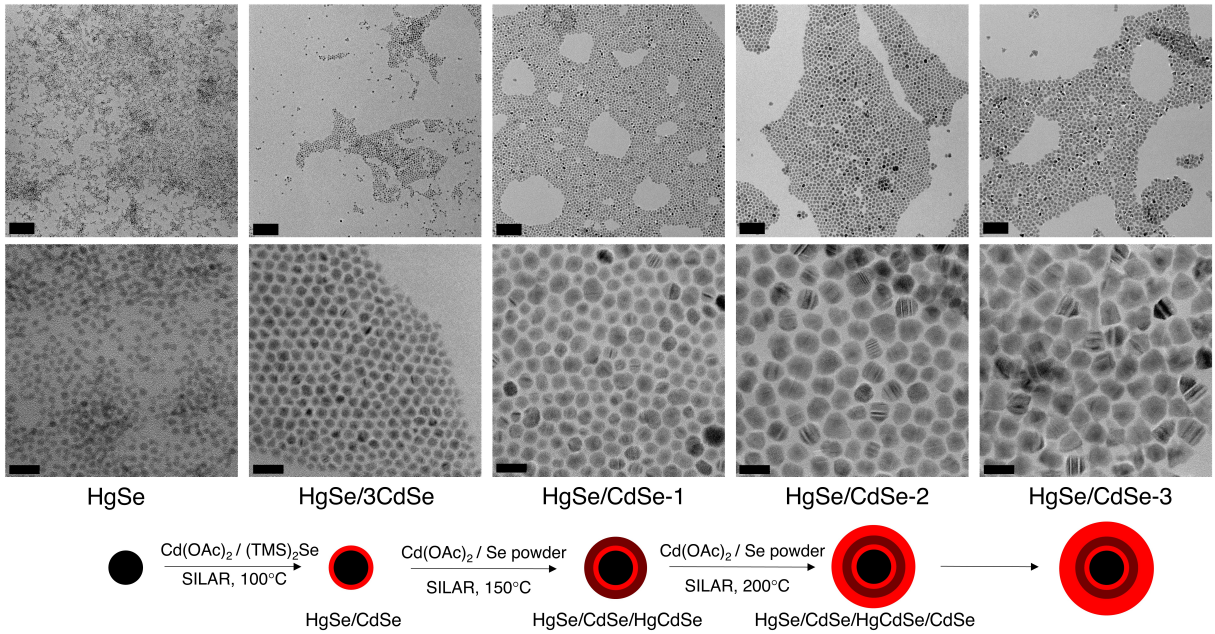

Figure 4.21: TEM images of HgSe and HgSe/CdSe QDs emitting at 2.0 µm. The scale bars are 100 nm for the top panels, and 20 nm for the bottom panels.

4.10 Additional data

4.10.1 TEM, SAXS, absorption, PL, and lifetimes of HgSe/CdSe QDs emitting at 2.0 µm

4.10.2 TEM, SAXS, absorption, PL, and lifetimes of HgSe/CdSe QDs emitting at 1.7 µm

Sample	TEM Size (nm)	SAXS Size (nm)
HgSe	4 ± 0.8	5.2 ± 1.2
HgSe/3CdSe	6.4 ± 0.7	7.0 ± 1.1
HgSe/CdSe-1	9.6 ± 1.6	10.2 ± 1.7
HgSe/CdSe-2	13.0 ± 1.8	13.0 ± 2.1
HgSe/CdSe-3	15.3 ± 1.8	15.1 ± 3.4

Table 4.1: Sizes of HgSe and HgSe/CdSe QDs measured by SAXS and TEM. The measurement of QD size by TEM were not precise at smaller sizes, and hence the SAXS sizes were used in the main text.

Sample	PLQE (150mW)	PLQE (15mW)	$1S_e$ occupancy	PLQY (15mW)
HgSe *	0.4% *	-	1.04	1.8% *
HgSe/3CdSe	14%	18%	0	18%
HgSe/CdSe-1	20%	22%	0	22%
HgSe/CdSe-2	31%	36%	0	36%
HgSe/CdSe-3	13%	16%	0.85	48%

Table 4.2: PL quantum efficiency (PLQE) of HgSe and HgSe/CdSe QDs measured using an integrating sphere with and 808 nm excitation, with powers 150 mW and 15 mW. The PLQE was lower at 150 mW excitation, likely due to localized heating of the sample. The PL signal from the HgSe sample was comparable to the PL signal from the blank sample, so the PLQE was estimated using area under the PL spectrum. The doping of HgSe and HgSe/CdSe-3 were determined using the absorption spectrum (see Section 4.9.2), and was used to calculate the PLQY.

Sample	TEM Size (nm)	SAXS Size (nm)
HgSe/3CdSe	5.9 ± 0.8	6.3 ± 0.9
HgSe/CdSe-1	8.4 ± 1.2	9.2 ± 1.8
HgSe/CdSe-2	11.7 ± 2.3	11.7 ± 2.2
HgSe/CdSe-3	12.6 ± 2.4	13.3 ± 2.3

Table 4.3: Sizes of HgSe and HgSe/CdSe QDs measured by SAXS and TEM.

Sample	PLQE (150mW)	PLQE (15mW)	$1S_e$ occupancy	PLQY (15mW)
HgSe/3CdSe	14%	17%	0	17%
HgSe/CdSe-1	34%	39%	0	39%
HgSe/CdSe-2	34%	43%	0	43%
HgSe/CdSe-3	44%	55%	∼0	55%

Table 4.4: PL quantum efficiency (PLQE) of HgSe and HgSe/CdSe QDs measured using an integrating sphere with and 808 nm excitation, with powers 150 mW and 15 mW. The PLQE was lower at 150 mW excitation, likely due to localized heating of the sample.

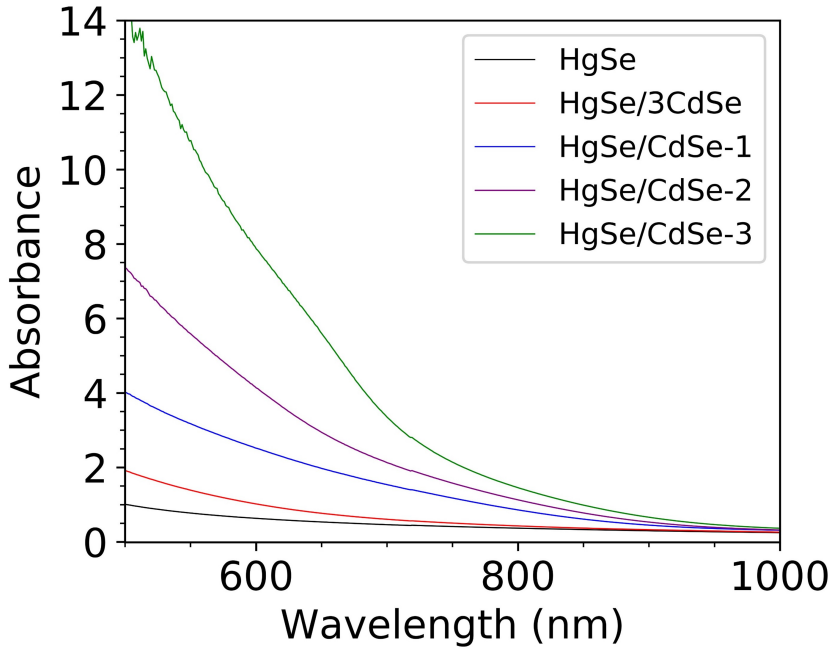

Figure 4.22: Vis-NIR absorption of HgSe and HgSe/CdSe QDs.

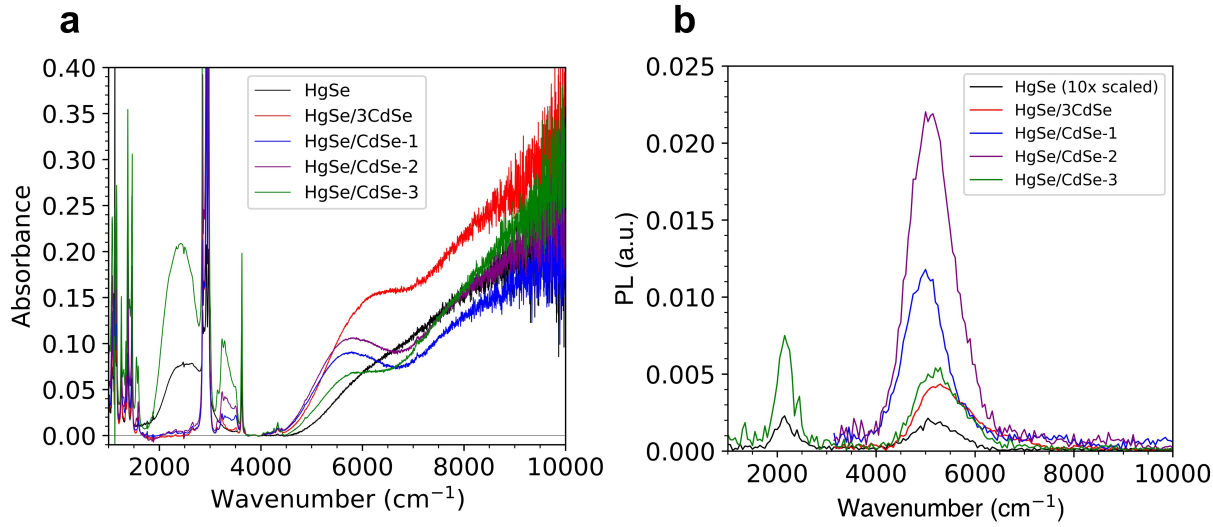

Figure 4.23: a, Absorption spectra of HgSe and HgSe/CdSe QDs. Spectra are quantitative, corresponding to equal masses of cores (as estimated from aliquots). Spectra are vertically shifted to set absorbance = 0 at 3800 cm^{-1}. b, PL spectra of HgSe and HgSe/CdSe QDs. The HgSe and HgSe/CdSe-3 samples are partially n-doped, and show both intraband and interband PL.

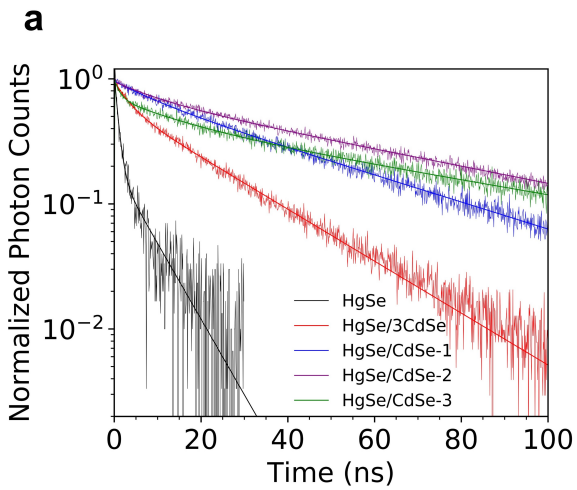

b

Sample	T1 (ns)	A	T2 (ns)	B	T3 (ns)	C
HgSe	0.86	82%	7.2	18%		
HgSe/3CdSe	3.50	36%	20.9	64%		
HgSe/CdSe-1	9.61	21%	40.2	79%		
HgSe/CdSe-2	11.05	25%	63.3	75%		
HgSe/CdSe-3	1.36	29%	14.4	24%	73.0	47%

$$PL = Ae^{-t/T1} + Be^{-t/T2} + Ce^{-t/T3}$$

Figure 4.24: a, PL lifetime data for HgSe and HgSe/CdSe QDs. Data are the same as in Fig. 4.3b. The HgSe/CdSe-3 sample was fit to a triexponential, while the remaining spectra fit well to biexponential functions. b, Fit results.

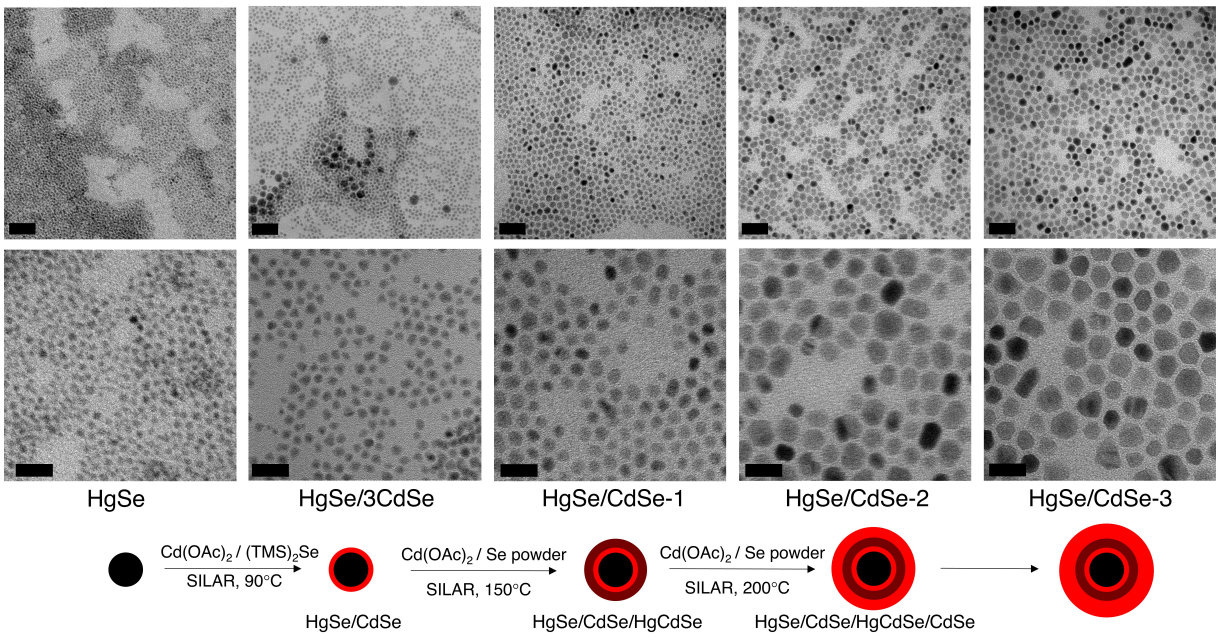

Figure 4.25: TEM images of HgSe and HgSe/CdSe QDs emitting at 1.7 µm. The scale bars are 50 nm for the top panels, and 20 nm for the bottom panels. There was a broad distribution of QDs seen in the HgSe and HgSe/3CdSe samples, which led to broad PL spectra.

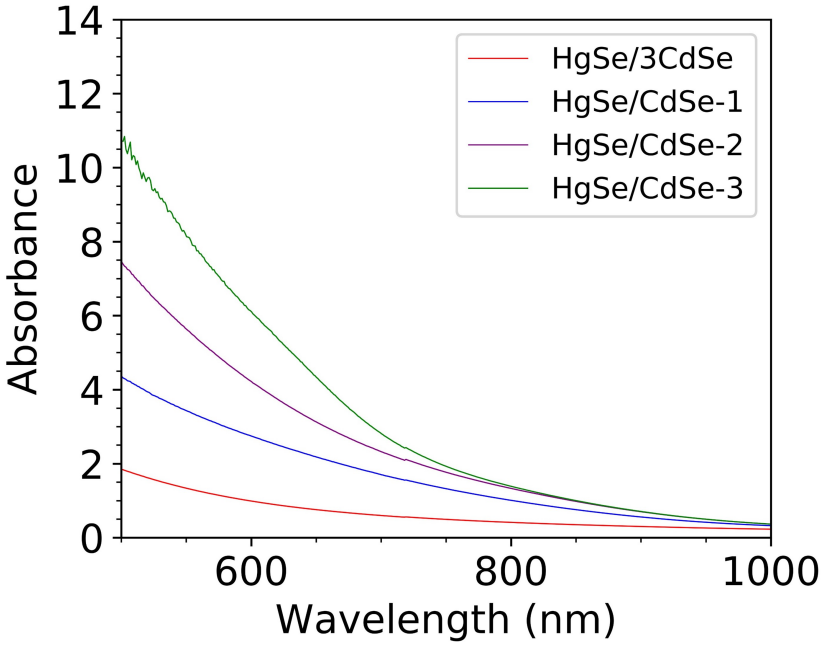

Figure 4.26: Vis-NIR absorption of HgSe/CdSe QDs

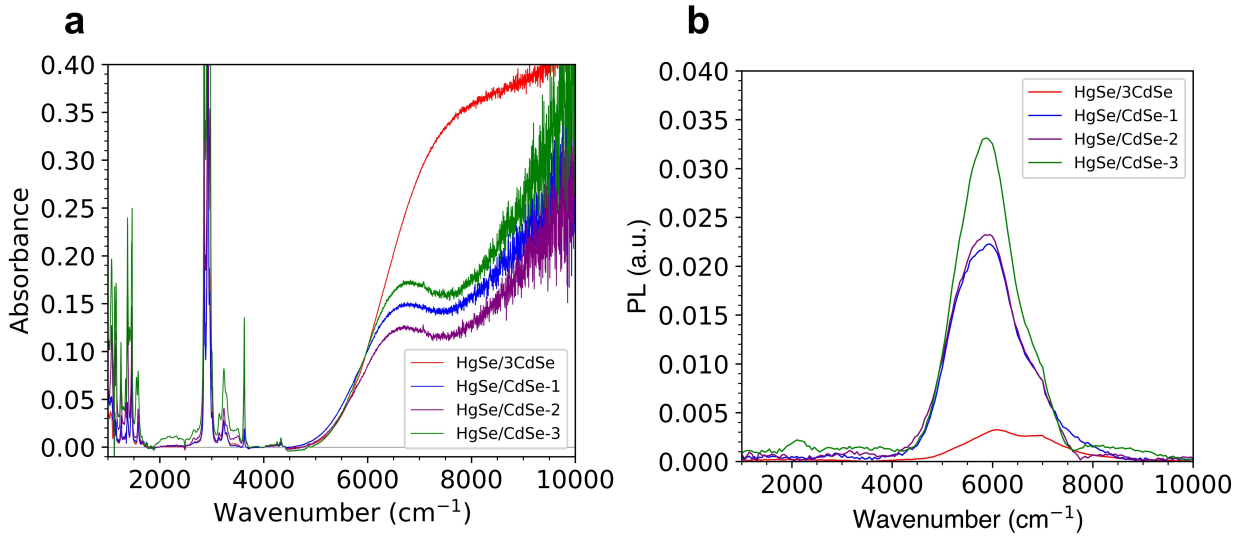

Figure 4.27: a, Absorption spectra of HgSe/CdSe QDs. Spectra are quantitative, corresponding to equal masses of cores (as estimated from aliquots). Spectra are vertically shifted to set absorbance = 0 at 3800 cm^{-1}. b, PL spectra of HgSe/CdSe QDs. The HgSe/CdSe-3 sample is partially n-doped, and show both intraband and interband PL. The spectra show broad PL due to a broad size distribution of cores.

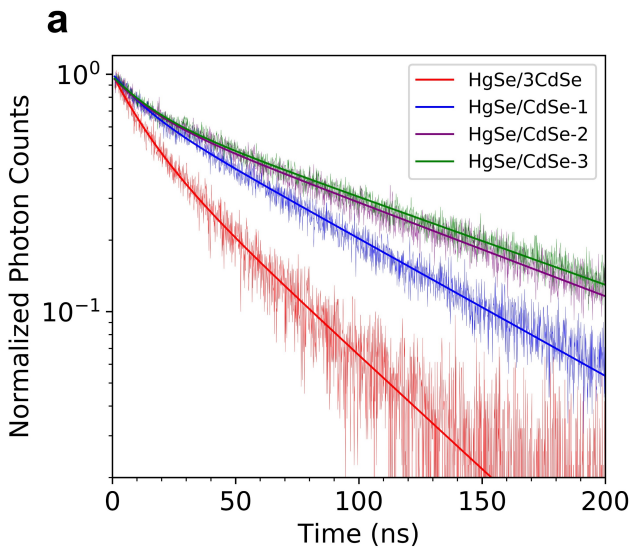

b

Sample	T1 (ns)	A	T2 (ns)	B
HgSe/3CdSe	12.6	41%	45.4	59%
HgSe/CdSe-1	12.3	24%	75.0	76%
HgSe/CdSe-2	14.8	27%	110.1	73%
HgSe/CdSe-3	15.1	28%	117.4	72%

$$PL = Ae^{-t/T1} + Be^{-t/T2}$$

Figure 4.28: a, PL lifetime data for HgSe/CdSe QDs. All spectra fit well to biexponential functions. b, Fit results.

CHAPTER 5

FUTURE DIRECTIONS

5.1 Overview

My work has demonstrated the dominance of ligand-FRET as the nonradiative mechanism in QDs emitting in the midwave- and shortwave- infrared regions. We have achieved a PLQY of 2% at 5 μm [38], and $\sim$60% at 1.7 μm [39] emission wavelengths. Our work has not shown evidence of a multiphonon relaxation for QDs emitting at 5µm. With the 2% emission quantum yield obtained, the relaxation is still dominated by FRET and the multiphonon limit was not yet attained [38]. The impact of my work has been in the direction of demonstrating a fundamental understanding of the underlying nonradiative mechanism at these wavelengths. Our work has led to several open questions, both in terms of fundamental understanding, as well as practical applications. In the sections below, I discuss a few future directions for research.

5.2 PLQY vs doping at 5 μm emission

While the thick shell HgSe/CdS QDs show a PLQY of 2% at 5 μm emission [38], this PLQY is only observed at low dopings of $<\sim$0.2 electrons/QD. At higher dopings, the PLQY drastically reduces (Figure 3.4). We attribute this doping-dependent PLQY quenching to arise from defects in the QD, which can act as trap states (Figure 3.20). These defect states could be present either within the core, at the core/shell interface, within the shell, or at the surface. Since this doping-dependent PLQY quenching is not observed for HgSe cores (Fig. 3.4), we can rule out presence of these states in the cores. We had initially proposed these defects states to lie at the core/shell interface in HgSe/CdS QDs, due to the large lattice mismatch between HgSe and CdS (Figure 3.20) [38].However, a qualitatively similar doping-dependent PLQY quenching is observed for HgSe/CdSe QDs (data not shown here).

Since HgSe and CdSe show a near-perfect lattice match, and a gradient core/shell interface is expected from our synthetic protocol, this likely rules out the presence of these defects at the core/shell interface.

These observations suggest that the defect states are present either within the shell, or at the QD surface. The former is more likely, since the thick shell is grown rapidly (∼5 mins per monolayer), at a relatively low temperature (200-220°C). These conditions might lead to shell growth in a kinetically trapped state, leading to defects near the $1S_e$ state of HgSe. One way to reduce these defects is by a post-synthetic annealing of the QDs at a relatively low temperature (possibly around 100°C). This annealing should lead to reconstruction of the shell and removal of the defect states, while avoiding ripening of the QDs. This hypothesis is supported by anecdotal evidence: a one-year old thick shell HgSe/CdSe QD sample (stored in a vial in the dark, at room temperature) was dispersed in TCE, and PL was recorded in solution. At a doping of ∼0.5 electrons/QD, the QDs showed an intraband PLQE of roughly 7%. The ageing of the QDs might have led to a slow reconstruction of the shell.

Furthermore, it is not clear whether the doping-dependent PLQY quenching is observed only for a thick CdS(/Se) shell, or it is seen for a thin shell (<∼3 monolayers) too. It is also unclear whether this quenching is observed only in solution, or in films too. This is an important question, because fabrication of mid-IR LEDs requires bright films of thin shell HgSe/CdS or HgSe/CdSe QDs. Future experiments of doping-dependent PLQY of films of HgSe/CdS or HgSe/CdSe QDs can demonstrate whether the doping-dependent quenching is observed in films and thin-shell QDs as well.

5.3 Incorporating QDs in inorganic matrices

The most important application of bright mid-IR emitting QDs is for fabricating cost-effective mid-IR LEDs [141]. Since a high mobility and efficient charge injection into the cores is necessary, this limits to use of QDs with a relatively thin shell (∼3-5 monolayers). To

overcome ligand-FRET quenching, it is necessary to perform a ligand exchange to replace the oleylamine ligands with shorter infrared-transparent ligands. An ideal situation is to incorporate the QDs into an all-inorganic matrix, which should show negligible absorption at 5 μm. Some possible candidates for the matrix are metal chalcogenide glasses like As_2S_3 [142], or perovskites like $CsPbBr_3$ [143]. A polar ligand exchange would first be performed on the core/shell QDs to cap them with short metal ion ligands. These QDs would then be dispersed into a metal-ligand precursor solution, which would decompose to a clear matrix upon spincoating and annealing. While this has been attempted in previous works [142], there has been no clear demonstration of a high PLQY in films emitting at 5 μm.

A major challenge in obtaining bright emission after a polar ligand exchange, is to completely remove residual solvent molecules during the annealing process. Typical polar solvents (DMF, NMF, formamide etc) show a strong absorption at 5 μm due to the C=O stretch and the broad N-H absorption due to hydrogen bonding. Presence of even a small amount of these molecules can lead to a drastic quenching of the PLQY.

In order to obtain bright films after polar exchange and incorporating into an inorganic matrix, it is necessary to perform routine optical characterizations of the films. This would involve FTIR absorption measurements to ensure that QDs are not etched during the baking, and measurement of doping, to control for a doping-dependent PLQY quenching. It is also necessary to measure the transmission of the excitation laser to control for the film thicknesses and QD concentration in the matrix.

The QD concentration in the matrix is expected to play an important role in the PLQY in films, as this would affect the rate of FRET between QDs in the film. For HgSe/CdSe QDs with a core diameter of 4.8 nm and total diameter of 7 nm, the rate of FRET between two QDs in contact with each other, is $\sim$ 2100 times faster than the radiative rate (see Appendix). This rate is much faster than the FRET rate observed for visible-emitting QDs [144], as the FRET efficiency scales with the frequency ν as $\sim \nu^{-3}$ (Eq. 4.11). Due to

the fast QD-QD FRET rate, an exciton would sample several QDs before emission, and would be quickly quenched if there is a subpopulation of defective QDs in the film. While this is unlikely in QDs after a solid-state ligand exchange with EdT, presence of defective QDs is much more likely after incorporation into an As_2S_3 matrix, as the annealing process often leads to etching of the QDs, accompanied by a blueshift of the interband absorption of HgSe. Attempts to incorporate HgSe/CdS or HgSe/CdSe QDs into an inorganic matrix will require a careful control of the QD concentration in the film, to account for QD-QD FRET processes.

5.4 Longwave QDs

The observation of a 2% PLQY in HgSe/CdS QDs at 5 μm shows that the multiphonon relaxation rate is slower than $\sim$15 ns [38]. This leads to the question: what is the rate of multiphonon relaxation, and what is the highest PLQY that can be attained by HgSe (or HgTe, HgS) QDs at 5 μm? A clear test for multiphonon relaxation would be the presence of a strong temperature-dependent PLQY (Eq. 1.2). Our experiments show that HgSe/CdS QDs show a negligible change in intraband PL upon cooling to 77 Kelvins (data not shown here), which suggests that they are not currently limited by the multiphonon relaxation limit. Further improvements in the PLQY upon growth of a thicker shell, or by a ligand exchange, might lead to reaching the multiphonon limit.

Another way to obtain multiphonon-limited QDs is by increasing the emission wavelength. Since the phonon relaxation increases exponentially as the phonon number is reduced, core/shell QDs emitting at 1000 cm^{-1} are expected to show a much larger rate of multiphonon relaxation. A major challenge in obtaining core/shell QDs at this size range is the difficulty in growth of a shell on larger QDs. Since we now have a synthetic protocol for growing a CdSe shell in the HgSe reaction mixture, this should allow for an easier growth of a thin CdSe shell, compared to previous cALD procedures [20, 37]. This should allow for

a subsequent growth of a thick CdSe shell, and performing temperature-dependent PLQY measurements to observe the multiphonon limit.

5.5 Bright HgSe/CdSe QDs in water

A major application of bright fluorophores in the SWIR (NIR-II) range is to perform deep-tissue in-vivo imaging [9, 4, 10, 120, 121, 122]. While PEG-ylated PbS/CdS QDs emitting at 1.7 μm have enabled imaging in-vivo upto a depth of 1 mm, the PLQY of these QDs is only 2% [9]. Brighter QDs should enable imaging at greater depths.

Our calculation of FRET to water molecules predicts that HgSe/CdSe QDs with a diameter of 13 nm should lead to a PLQY of 12% at 1.7 μm emission [39]. However, we have not experimentally measured the PLQY after water-solubilization of these QDs. Future work will involve PEG-ylation of these QDs, and possibly growing a thicker shell, to obtain bright fluorophores for in-vivo imaging.

CHAPTER 6

SUMMARY AND CONCLUDING REMARKS

Quantum dots show a great potential for fabricating low-cost detectors and emitters in the midwave- and shortwave- infrared wavelengths. Quantum dots also show potential as fluorophores for deep in-vivo imaging in the second near-infrared window.

To overcome the fast nonradiative decay in quantum dots at these wavelengths, I have developed the growth of a thick CdS and CdSe shell on HgSe quantum dots. Growth of the thick shell led to a dramatic increase in the photoluminescence quantum yield, leading to record quantum yields of 2% at 5μm and 63% at 1.7μm. The trend of the quantum yield with shell thickness demonstrated that the dominant nonradiative mechanism is a Forster energy transfer to ligand and solvent molecules.

My research paves the wave for developing better performing detectors and emitters in the midwave infrared, and also provides motivation for using our thick-shell quantum dots for deep in-vivo imaging.

APPENDIX A

CALCULATION OF QD-QD FRET RATE

The goal is to calculate the rate of FRET-energy transfer between individual QDs in film. Let us consider a film of HgSe/CdS QDs with a core diameter of r_{core}, and a total QD diameter of r_{QD}. For the sake of simplicity, let us assume an FCC close-packed structure, with a QD-QD separation of d_{sep}. In this film, each QD is surrounded by 12 nearest neighbors.

Let us assume the approximation that the FRET rate between QDs is identical to the FRET rate between two point particles with the same separation. To calculate the FRET rate from a QD to one of its nearest neighbors, we will follow Eq. 4.12 and perform the spatial integral to obtain the volume of the QD absorber. The ratio of FRET rate to nonradiative rate is then:

$$\frac{\gamma_{FRET}}{\gamma_{rad}} = \frac{3}{128\pi^4 n}\frac{V_{core}}{d_{sep}^6}\int \frac{\epsilon''(\overline{\nu})f_D(\overline{\nu})d\overline{\nu}}{\overline{\nu}^3} \tag{A.1}$$

Where n is the refractive index, V_{core} is the the volume of the core QD, $V_{core} = \frac{4}{3}\pi r_{core}^3$, ϵ'' is the imaginary index, f_D is the normalized QD emission spectrum, and $\overline{\nu}$ is the wavenumber.

Let us set n = 1.6 for a HgSe/CdS film, 2^*r_{core} = 4.8 nm, 2^*r_{QD} = 7.0 nm, d_{sep} = 10.6 nm when QDs are coated with a 1.8 nm long oleylamine ligand.

From Fig. 1A, we can approximate the emission spectrum to be a Gaussian with peak at 2100 cm^{-1} and FWHM 450 cm^{-1}, and the absorption to be a Gaussian with peak at 2450 cm^{-1} and FWHM 950 cm^{-1}. From the calculated imaginary dielectric function in Fig. 1B, we can set the peak of ϵ'' to be 5, with a Gaussian shape as the absorption spectrum.

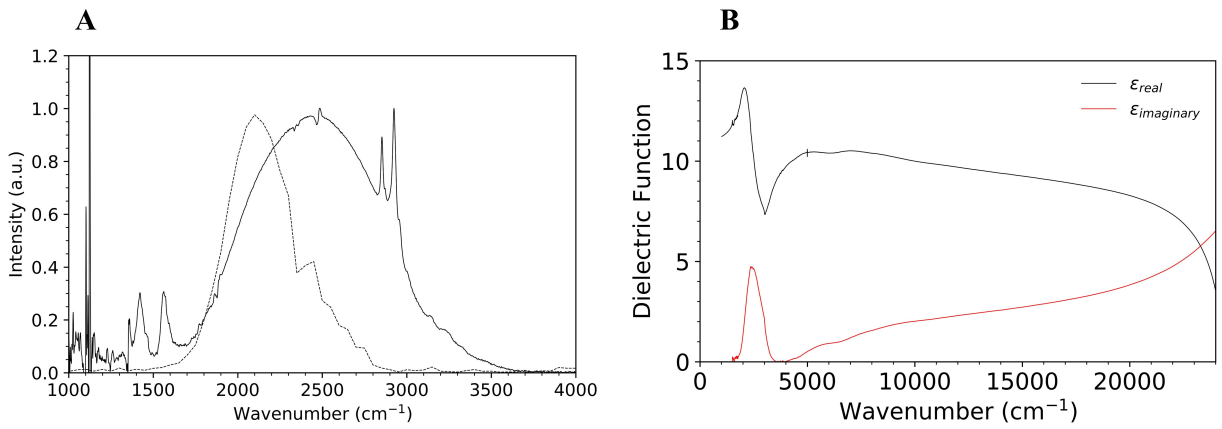

Figure A.1: (A)(Solid) Normalized intraband absorption spectrum of HgSe/CdS QDs after subtraction of ligands, and (dotted) normalized intraband PL of HgSe/CdS QDs; (B) Real and imaginary dielectric of HgSe core QDs, calculated by Kramers-Kronig relations.

Using these values, we obtain $\frac{V_{core}}{d_{sep}^6}$=$4.1 \times 10^{16} cm^{-3}$, $\int \frac{\epsilon''(\overline{\nu}) f_D(\overline{\nu}) d\overline{\nu}}{\overline{\nu}^3} = 3.4 \times 10^{-10} cm^3$. So we get $\frac{\gamma_{FRET}}{\gamma_{rad}} = 2080$. Including 12 nearest neighbors, we get the FRET rate to be 25,000 faster than the radiative rate. Performing the calculation for subsequent nearest neighbors will lead to a negligible change in the FRET rate.

Thus, on an average, an excited QD will interact with $\sim$ 25,000 before radiating, which corresponds to a range of $\sim$300 nm. If the PLQY is 2%, the QD will interact with $\sim$500 other QDs before radiating, which corresponds to a range of $\sim$80 nm. Therefore, there should be less than 1 in 500 defective QDs in order to obtain a PLQE of 2%.

Performing the calculation for QDs in an As_2S_3 matrix, for a 100% QD loading we have $d_{sep} = 7nm$, giving FRET rate = 25,000 times faster than the radiative rate. When d_{sep} is increased, the QD loading fraction scales as d_{sep}^{-3}. Thus for a 10% loading, FRET rate is 3000 times faster than radiative rate. For a 1% loading, FRET rate is 30 times faster than radiative rate. Hence, to obtain a PLQY of $\sim$3%, we need a QD loading of $\sim$1% in order to be insensitive to the presence of defective QDs.

REFERENCES

[1] C. Melnychuk and P. Guyot-Sionnest, "Auger Suppression in n-Type HgSe Colloidal Quantum Dots," *ACS Nano*, vol. 13, pp. 10512–10519, 2019.

[2] S. Tutihasi, "Quenching of Photoconductivity in Cadmium Sulfide," *Journal of the Optical Society of America*, vol. 46, p. 443, 1956.

[3] B. A. Kulp, "Defects in cadmium sulfide crystals," *Journal of Applied Physics*, vol. 36, pp. 553–558, 1965.

[4] D. Franke, D. K. Harris, O. Chen, O. T. Bruns, J. A. Carr, M. W. Wilson, and M. G. Bawendi, "Continuous injection synthesis of indium arsenide quantum dots emissive in the short-wavelength infrared," *Nature Communications*, vol. 7, p. 12749, 2016.

[5] S. Krishnamurthy, A. Singh, Z. Hu, A. V. Blake, Y. Kim, A. Singh, E. A. Dolgopolova, D. J. Williams, A. Piryatinski, A. V. Malko, H. Htoon, M. Sykora, and J. A. Hollingsworth, "PbS/CdS Quantum Dot Room-Temperature Single-Emitter Spectroscopy Reaches the Telecom O and S Bands via an Engineered Stability," *ACS Nano*, vol. 15, pp. 575–587, 2021.

[6] O. E. Semonin, J. C. Johnson, J. M. Luther, A. G. Midgett, A. J. Nozik, and M. C. Beard, "Absolute photoluminescence quantum yields of IR-26 Dye, PbS, and PbSe quantum dots," *Journal of Physical Chemistry Letters*, vol. 1, pp. 2445–2450, 2010.

[7] S. Keuleyan, J. Kohler, and P. Guyot-Sionnest, "Photoluminescence of mid-infrared HgTe colloidal quantum dots," *Journal of Physical Chemistry C*, vol. 118, pp. 2749–2753, 2014.

[8] N. M. Abdelazim, Q. Zhu, Y. Xiong, Y. Zhu, M. Chen, N. Zhao, S. V. Kershaw, and A. L. Rogach, "Room Temperature Synthesis of HgTe Quantum Dots in an Aprotic Solvent Realizing High Photoluminescence Quantum Yields in the Infrared," *Chemistry of Materials*, vol. 29, pp. 7859–7867, 2017.

[9] F. Wang, F. Ren, Z. Ma, L. Qu, R. Gourgues, C. Xu, A. Baghdasaryan, J. Li, I. E. Zadeh, J. W. Los, A. Fognini, J. Qin-Dregely, and H. Dai, "In vivo non-invasive confocal fluorescence imaging beyond 1,700 nm using superconducting nanowire single-photon detectors," *Nature Nanotechnology*, vol. 17, pp. 653–660, 2022.

[10] M. Zhang, J. Yue, R. Cui, Z. Ma, H. Wan, F. Wang, S. Zhu, Y. Zhou, Y. Kuang, Y. Zhong, D. W. Pang, and H. Dai, "Bright quantum dots emitting at 1,600 nm in the NIR-IIb window for deep tissue fluorescence imaging," *Proceedings of the National Academy of Sciences of the United States of America*, vol. 115, pp. 6590–6595, 2018.

[11] O. T. Bruns, T. S. Bischof, D. K. Harris, D. Franke, Y. Shi, L. Riedemann, A. Bartelt, F. B. Jaworski, J. A. Carr, C. J. Rowlands, M. W. Wilson, O. Chen, H. Wei, G. W. Hwang, D. M. Montana, I. Coropceanu, O. B. Achorn, J. Kloepper, J. Heeren, P. T.

So, D. Fukumura, K. F. Jensen, R. K. Jain, and M. G. Bawendi, "Next-generation in vivo optical imaging with short-wave infrared quantum dots," *Nature Biomedical Engineering*, vol. 1, p. 0056, 2017.

[12] Y. Zhong, Z. Ma, F. Wang, X. Wang, Y. Yang, Y. Liu, X. Zhao, J. Li, H. Du, M. Zhang, Q. Cui, S. Zhu, Q. Sun, H. Wan, Y. Tian, Q. Liu, W. Wang, K. C. Garcia, and H. Dai, "In vivo molecular imaging for immunotherapy using ultra-bright near-infrared-IIb rare-earth nanoparticles," *Nature Biotechnology*, vol. 37, pp. 1322–1331, 2019.

[13] M. Liu, N. Yazdani, M. Yarema, M. Jansen, V. Wood, and E. H. Sargent, "Colloidal quantum dot electronics," *Nature Electronics*, vol. 4, no. 8, pp. 548–558, 2021.

[14] Y. Shirasaki, G. J. Supran, M. G. Bawendi, and V. Bulović, "Emergence of colloidal quantum-dot light-emitting technologies," *Nature Photonics*, vol. 7, pp. 13–23, 2013.

[15] M. M. ACKERMAN, "FROM BASIC CONCEPTS TO EMERGING DEVICES: MERCURY TELLURIDE COLLOIDAL QUANTUM DOT INFRARED PHOTODIODES FOR 1 - 5 MICRONS DETECTION A," *University of Chicago*, vol. 68, no. 1, pp. 1–12, 2020.

[16] A. Rogalsky, "History of infrared detectors," *OPTOELECTRONICS REVIEW*, vol. 20, no. 3, pp. 279–308, 2012.

[17] M. M. Ackerman, X. Tang, and P. Guyot-sionnest, "SUPPORTING INFORMATION Fast and Sensitive Colloidal Quantum Dot Mid-Wave Infrared Photodetectors Matthew M. Ackerman, Xin Tang, Philippe Guyot-Sionnest James Franck Institute, 929 E. 57," 2018.

[18] C. Melnychuk, "Infrared Carrier Dynamics in Mercury Chalcogenide Quantum Dots: from Fundamental Spectroscopy to Next-Generation Optoelectronics," *University of Chicago*, 2022.

[19] P. Guyot-Sionnest, M. M. Ackerman, and X. Tang, "Colloidal quantum dots for infrared detection beyond silicon," *The Journal of Chemical Physics*, vol. 151, p. 060901, 2019.

[20] G. Shen and P. Guyot-sionnest, "HgTe/CdTe and HgSe/CdX (X = S, Se, and Te) Core/Shell Mid- Infrared Quantum Dots," *Chemistry of Materials*, vol. 31, pp. 286–293, 2019.

[21] M. D. Peterson, L. C. Cass, R. D. Harris, K. Edme, K. Sung, and E. A. Weiss, "The role of ligands in determining the exciton relaxation dynamics in semiconductor quantum dots," *Annual Review of Physical Chemistry*, vol. 65, pp. 317–339, 2014.

[22] P. Guyot-Sionnest, B. Wehrenberg, and D. Yu, "Intraband relaxation in CdSe nanocrystals and the strong influence of the surface ligands," *Journal of Chemical Physics*, vol. 123, p. 074709, 2005.

[23] P. Han and G. Bester, "Carrier relaxation in colloidal nanocrystals: Bridging large electronic energy gaps by low-energy vibrations," *Physical Review B*, vol. 91, p. 085305, 2015.

[24] X. Li, H. Nakayama, and Y. Arakawa, "Phonon bottleneck in quantum dots: role of lifetime of the confined optical phonons," *Physical Review B*, vol. 59, pp. 5069–5073, 1999.

[25] T. Grange, R. Ferreira, and G. Bastard, "Polaron relaxation in self-assembled quantum dots: Breakdown of the semiclassical model," *Physical Review B*, vol. 76, p. 241304, 2007.

[26] I. A. Dmitriev and R. A. Suris, "Anharmonicity-assisted multiphonon transitions between distant levels in semiconductor quantum dots," *Physical Review B*, vol. 90, p. 155431, 2014.

[27] D. Bozyigit, N. Yazdani, M. Yarema, O. Yarema, W. M. M. Lin, S. Volk, K. Vuttivorakulchai, M. Luisier, F. Juranyi, and V. Wood, "Soft surfaces of nanomaterials enable strong phonon interactions," *Nature*, vol. 531, pp. 618–622, 2016.

[28] D. A. Hanifi, N. D. Bronstein, B. A. Koscher, Z. Nett, J. K. Swabeck, K. Takano, A. M. Schwartzberg, and L. Maserati, "Redefining near-unity luminescence in quantum dots with photothermal threshold quantum yield," *Science*, vol. 363, no. March, pp. 1199–1202, 2019.

[29] B. O. Dabbousi, J. Rodriguez-Viejo, F. V. Mikulec, J. R. Heine, H. Mattoussi, R. Ober, K. F. Jensen, and M. G. Bawendi, "(CdSe)ZnS CoreShell Quantum Dots: Synthesis and Characterization of a Size Series of Highly Luminescent Nanocrystallites," *The Journal of Physical Chemistry B*, vol. 101, no. 46, pp. 9463–9475, 1997.

[30] A. Pandey and P. Guyot-Sionnest, "Slow Electron Cooling in Colloidal Quantum Dots," *Science*, vol. 322, pp. 929–932, 2008.

[31] B. K. Ridley, "Quantum Processes in Semiconductors," *Oxford University Press*, vol. 5 ed., 2013.

[32] B. K. Ridley, "Multiphonon, non-radiative transition rate for electrons in semiconductors and insulators," *Journal of Physics C: Solid State Physics*, vol. 11, no. 11, pp. 2323–2341, 1978.

[33] H. Zhu, A. Prakash, D. N. Benoit, C. J. Jones, and V. L. Colvin, "Low temperature synthesis of ZnS and CdZnS shells on CdSe quantum dots.," *Nanotechnology*, vol. 21, no. 25, p. 255604, 2010.

[34] M. A. Hines and P. Guyot-Sionnest, "Synthesis and characterization of strongly luminescing ZnS-capped CdSe nanocrystals," *Journal of Physical Chemistry*, vol. 100, no. 2, pp. 468–471, 1996.

[35] Z. Deng, K. S. Jeong, and P. Guyot-Sionnest, "Colloidal quantum dots intraband photodetectors," *ACS Nano*, vol. 8, pp. 11707–11714, 2014.

[36] Z. Deng and P. Guyot-Sionnest, "Intraband Luminescence from HgSe/CdS Core/Shell Quantum Dots," *ACS Nano*, vol. 10, pp. 2121–2127, 2016.

[37] L. K. Sagar, W. Walravens, J. Maes, P. Geiregat, and Z. Hens, "HgSe/CdE (E = S, Se) Core/Shell Nanocrystals by Colloidal Atomic Layer Deposition," *Journal of Physical Chemistry C*, vol. 121, pp. 13816–13822, 2017.

[38] A. Kamath, C. Melnychuk, and P. Guyot-Sionnest, "Toward Bright Mid-Infrared Emitters Thick-Shell n-Type HgSe-CdS Nanocrystals," *Journal of the American Chemical Society*, vol. 143, pp. 19567–19575, 2021.

[39] A. Kamath, R. D. Schaller, and P. Guyot-sionnest, "Bright Fluorophores in the Second Near-Infrared Window: HgSe/CdSe Quantum Dots," *arXiv*, vol. arXiv:2301, 2023.

[40] X. Chen, J. L. Hutchison, P. J. Dobson, and G. Wakefield, "A one-step aqueous synthetic route to extremely small CdSe nanoparticles," *Journal of Colloid and Interface Science*, vol. 319, no. 1, pp. 140–143, 2008.

[41] B. Mahler, P. Spinicelli, S. Buil, X. Quelin, J. P. Hermier, and B. Dubertret, "Towards non-blinking colloidal quantum dots," *Nature Materials*, vol. 7, pp. 659–664, 2008.

[42] J. Van Embden, J. Jasieniak, and P. Mulvaney, "Mapping the optical properties of CdSe/CdS heterostructure nanocrystals: The effects of core size and shell thickness," *Journal of the American Chemical Society*, vol. 131, pp. 14299–14309, 2009.

[43] O. Chen, J. Zhao, V. P. Chauhan, J. Cui, C. Wong, D. K. Harris, H. Wei, H. S. Han, D. Fukumura, R. K. Jain, and M. G. Bawendi, "Compact high-quality CdSe-CdS core-shell nanocrystals with narrow emission linewidths and suppressed blinking," *Nature Materials*, vol. 12, pp. 445–451, 2013.

[44] W. K. Bae, L. A. Padilha, Y. S. Park, H. McDaniel, I. Robel, J. M. Pietryga, and V. I. Klimov, "Controlled alloying of the core-shell interface in CdSe/CdS quantum dots for suppression of auger recombination," *ACS Nano*, vol. 7, pp. 3411–3419, 2013.

[45] H. Zhao, G. Sirigu, A. Parisini, A. Camellini, G. Nicotra, F. Rosei, V. Morandi, M. Zavelani-Rossi, and A. Vomiero, "Dual emission in asymmetric "giant" PbS/CdS/CdS core/shell/shell quantum dots," *Nanoscale*, vol. 8, pp. 4217–4226, 2016.

[46] D. C. Lee, I. Robel, J. M. Pietryga, and V. I. Klimov, "Infrared-active heterostructured nanocrystals with ultralong carrier lifetimes," *Journal of the American Chemical Society*, vol. 132, pp. 9960–9962, 2010.

[47] C. J. Hanson, N. F. Hartmann, A. Singh, X. Ma, W. J. Debenedetti, J. L. Casson, J. K. Grey, Y. J. Chabal, A. V. Malko, M. Sykora, A. Piryatinski, H. Htoon, and J. A.

Hollingsworth, "Giant PbSe/CdSe/CdSe Quantum Dots: Crystal-Structure-Defined Ultrastable Near-Infrared Photoluminescence from Single Nanocrystals," *Journal of the American Chemical Society*, vol. 139, pp. 11081–11088, 2017.

[48] K. P. Acharya, H. M. Nguyen, M. Paulite, A. Piryatinski, J. Zhang, J. L. Casson, H. Xu, H. Htoon, and J. A. Hollingsworth, "Elucidation of two giants: Challenges to thick-shell synthesis in CdSe/ZnSe and ZnSe/CdS Core/shell quantum dots," *Journal of the American Chemical Society*, vol. 137, pp. 3755–3758, 2015.

[49] A. M. Dennis, B. D. Mangum, A. Piryatinski, Y. S. Park, D. C. Hannah, J. L. Casson, D. J. Williams, R. D. Schaller, H. Htoon, and J. A. Hollingsworth, "Suppressed blinking and auger recombination in near-infrared type-II InP/CdS nanocrystal quantum dots," *Nano Letters*, vol. 12, pp. 5545–5551, 2012.

[50] V. K. Lamer and R. H. Dinegar, "Theory, Production and Mechanism of Formation of Monodispersed Hydrosols," *Journal of the American Chemical Society*, vol. 72, no. 11, pp. 4847–4854, 1950.

[51] T. Sugimoto, "The theory of the nucleation of monodisperse particles in open systems and its application to agbr systems," *Journal of Colloid And Interface Science*, vol. 150, no. 1, pp. 208–225, 1992.

[52] J. J. Li, Y. A. Wang, W. Guo, J. C. Keay, T. D. Mishima, M. B. Johnson, and X. Peng, "Large-scale synthesis of nearly monodisperse CdSe/CdS core/shell nanocrystals using air-stable reagents via successive ion layer adsorption and reaction," *Journal of the American Chemical Society*, vol. 125, no. 41, pp. 12567–12575, 2003.

[53] H. Zhang and P. Guyot-Sionnest, "Shape-Controlled HgTe Colloidal Quantum Dots and Reduced Spin-Orbit Splitting in the Tetrahedral Shape," *Journal of Physical Chemistry Letters*, vol. 11, no. 16, pp. 6860–6866, 2020.

[54] I. L. Medintz, H. T. Uyeda, E. R. Goldman, and H. Mattoussi, "Quantum dot bioconjugates for imaging, labelling and sensing," *Nature Materials*, vol. 4, pp. 435–446, 2005.

[55] J. M. Pietryga, Y. S. Park, J. Lim, A. F. Fidler, W. K. Bae, S. Brovelli, and V. I. Klimov, "Spectroscopic and device aspects of nanocrystal quantum dots," *Chemical Reviews*, vol. 116, pp. 10513–10622, 2016.

[56] C. Melnychuk and P. Guyot-Sionnest, "Multicarrier dynamics in quantum dots," *Chemical Reviews*, vol. 121, pp. 2325–2372, 2021.

[57] W. A. Tisdale, K. J. Williams, B. A. Timp, D. J. Norris, E. S. Aydil, and X. Y. Zhu, "Hot-Electron Transfer from Semiconductor Nanocrystals," *Science*, vol. 328, pp. 1543–1547, 2010.

[58] I. J. Kramer and E. H. Sargent, "Colloidal quantum dot photovoltaics: A path forward," *ACS Nano*, vol. 5, pp. 8506–8514, 2011.

[59] M. Park, D. Choi, Y. Choi, H. B. Shin, and K. S. Jeong, "Mid-Infrared Intraband Transition of Metal Excess Colloidal Ag2Se Nanocrystals," *ACS Photonics*, vol. 5, pp. 1907–1911, 2018.

[60] I. Ramiro, B. Kundu, M. Dalmases, O. Özdemir, M. Pedrosa, and G. Konstantatos, "Size- And Temperature-Dependent Intraband Optical Properties of Heavily n-Doped PbS Colloidal Quantum Dot Solid-State Films," *ACS Nano*, vol. 14, pp. 7161–7169, 2020.

[61] R. Bera, G. Kim, D. Choi, J. Kim, and K. S. Jeong, "Beyond the Bandgap Photoluminescence of Colloidal Semiconductor Nanocrystals," *Journal of Physical Chemistry Letters*, vol. 12, pp. 2562–2569, 2021.

[62] H. Benisty, C. M. Sotomayor-Torrès, and C. Weisbuch, "Intrinsic mechanism for the poor luminescence properties of quantum-box systems," *Physical Review B*, vol. 44, pp. 10945–10948, 1991.

[63] I. Vurgaftman and J. Singh, "Effect of spectral broadening and electron-hole scattering on carrier relaxation in GaAs quantum dots," *Applied Physics Letters*, vol. 64, pp. 232–234, 1994.

[64] A. L. Efrosa, V. A. Kharchenkob, and M. Rosen, "Breaking the phonon bottleneck in nanometer quantum dots: Role of Auger-Like Processes," *Solid State Communications*, vol. 93, pp. 281–284, 1995.

[65] V. I. Klimov, D. W. McBranch, C. A. Leatherdale, and M. G. Bawendi, "Electron and hole relaxation pathways in semiconductor quantum dots," *Physical Review B*, vol. 60, pp. 13740–13749, 1999.

[66] R. R. Cooney, S. L. Sewall, K. E. H. Anderson, E. A. Dias, and P. Kambhampati, "Breaking the phonon bottleneck for holes in semiconductor Quantum dots," *Physical Review Letters*, vol. 98, no. 17, pp. 1–4, 2007.

[67] L. Wang, Z. Chen, G. Liang, Y. Li, R. Lai, T. Ding, and K. Wu, "Observation of a phonon bottleneck in copper-doped colloidal quantum dots," *Nature Communications*, vol. 10, p. 4532, 2019.

[68] J. Wang, L. Wang, S. Yu, T. Ding, D. Xiang, and K. Wu, "Spin blockade and phonon bottleneck for hot electron relaxation observed in n-doped colloidal quantum dots," *Nature Communications*, vol. 12, p. 550, 2021.

[69] N. Yazdani, D. Bozyigit, K. Vuttivorakulchai, M. Luisier, I. Infante, and V. Wood, "Tuning Electron-Phonon Interactions in Nanocrystals through Surface Termination," *Nano Letters*, vol. 18, pp. 2233–2242, 2018.

[70] M. Chen and P. Guyot-Sionnest, "Reversible Electrochemistry of Mercury Chalcogenide Colloidal Quantum Dot Films," *ACS Nano*, vol. 11, pp. 4165–4173, 2017.

[71] C. Livache, B. Martinez, N. Goubet, C. Gréboval, J. Qu, A. Chu, S. Royer, S. Ithurria, M. G. Silly, B. Dubertret, and E. Lhuillier, "A colloidal quantum dot infrared photodetector and its use for intraband detection," *Nature Communications*, vol. 10, p. 2125, 2019.

[72] W. Nan, Y. Niu, H. Qin, F. Cui, Y. Yang, R. Lai, W. Lin, and X. Peng, "Crystal structure control of zinc-blende CdSe/CdS core/shell nanocrystals: Synthesis and structure-dependent optical properties," *Journal of the American Chemical Society*, vol. 134, pp. 19685–19693, 2012.

[73] C. Pu and X. Peng, "To Battle Surface Traps on CdSe/CdS Core/Shell Nanocrystals: Shell Isolation versus Surface Treatment," *Journal of the American Chemical Society*, vol. 138, pp. 8134–8142, 2016.

[74] Y. Niu, C. Pu, R. Lai, R. Meng, W. Lin, H. Qin, and X. Peng, "One-pot/three-step synthesis of zinc-blende CdSe/CdS core/shell nanocrystals with thick shells," *Nano Research*, vol. 10, pp. 1149–1162, 2017.

[75] C. E. Morrison, F. Wang, N. P. Rath, B. M. Wieliczka, R. A. Loomis, and W. E. Buhro, "Cadmium Bis(phenyldithiocarbamate) as a Nanocrystal Shell-Growth Precursor," *Inorganic Chemistry*, vol. 56, pp. 12920–12929, 2017.

[76] D. V. Talapin, J. H. Nelson, E. V. Shevchenko, S. Aloni, B. Sadtler, and A. P. Alivisatos, "Seeded growth of highly luminescent CdSe/CdS nanoheterostructures with rod and tetrapod morphologies," *Nano Letters*, vol. 7, pp. 2951–2959, 2007.

[77] S. Singh and K. M. Ryan, "Occurrence of Polytypism in Compound Colloidal Metal Chalcogenide Nanocrystals, Opportunities, and Challenges," *Journal of Physical Chemistry Letters*, vol. 6, pp. 3141–3148, 2015.

[78] Y.-w. Jun, S.-M. Lee, N.-J. Kang, and J. Cheon, "Controlled synthesis of multi-armed CdS nanorod architectures using monosurfactant system," *Journal of the American Chemical Society*, vol. 123, pp. 5150–5151, 2001.

[79] Y. Gao and X. Peng, "Crystal structure control of CdSe nanocrystals in growth and nucleation: Dominating effects of surface versus interior structure," *Journal of the American Chemical Society*, vol. 136, pp. 6724–6732, 2014.

[80] A. W. Wills, M. S. Kang, K. M. Wentz, S. E. Hayes, A. Sahu, W. L. Gladfelter, and D. J. Norris, "Synthesis and characterization of Al- and In-doped CdSe nanocrystals," *Journal of Materials Chemistry*, vol. 22, pp. 6335–6342, 2012.

[81] J. H. Choi, A. T. Fafarman, S. J. Oh, D. K. Ko, D. K. Kim, B. T. Diroll, S. Muramoto, J. G. Gillen, C. B. Murray, and C. R. Kagan, "Bandlike transport in strongly coupled and doped quantum dot solids: A route to high-performance thin-film electronics," *Nano Letters*, vol. 12, pp. 2631–2638, 2012.

[82] C. Tuinenga, J. Jasinski, T. Iwamoto, and V. Chikan, "In situ observation of heterogeneous growth of CdSe quantum dots: Effect of indium doping on the growth kinetics," *ACS Nano*, vol. 2, pp. 1411–1421, 2008.

[83] J. Tang, L. Brzozowski, D. A. R. Barkhouse, X. Wang, R. Debnath, R. Wolowiec, E. Palmiano, L. Levina, A. G. Pattantyus-Abraham, D. Jamakosmanovic, and E. H. Sargent, "Quantum dot photovoltaics in the extreme quantum confinement regime: The surface-chemical origins of exceptional air- and light-stability," *ACS Nano*, vol. 4, pp. 869–878, 2010.

[84] A. Stavrinadis and G. Konstantatos, "Strategies for the Controlled Electronic Doping of Colloidal Quantum Dot Solids," *ChemPhysChem*, vol. 17, pp. 632–644, 2016.

[85] K. S. Jeong, Z. Deng, S. Keuleyan, H. Liu, and P. Guyot-Sionnest, "Air-stable n-doped colloidal HgS quantum dots," *Journal of Physical Chemistry Letters*, vol. 5, pp. 1139–1143, 2014.

[86] S. Christodoulou, I. Ramiro, A. Othonos, A. Figueroba, M. Dalmases, O. Özdemir, S. Pradhan, G. Itskos, and G. Konstantatos, "Single-Exciton Gain and Stimulated Emission across the Infrared Telecom Band from Robust Heavily Doped PbS Colloidal Quantum Dots," *Nano Letters*, vol. 20, pp. 5909–5915, 2020.

[87] M. Shim and P. Guyot-Sionnest, "Intraband hole burning of colloidal quantum dots," *Physical Review B*, vol. 64, p. 245342, 2001.

[88] B. L. Wehrenberg and P. Guyot-Sionnest, "Electron and hole injection in PbSe quantum dot films," *Journal of the American Chemical Society*, vol. 125, pp. 7806–7807, 2003.

[89] D. Yu, C. Wang, and P. Guyot-Sionnest, "n -Type Conducting CdSe Nanocrystal Solids," *Science*, vol. 300, pp. 1277–1280, 2003.

[90] H. Liu, S. Keuleyan, and P. Guyot-Sionnest, "N- and p-type HgTe quantum dot films," *Journal of Physical Chemistry C*, vol. 116, pp. 1344–1349, 2012.

[91] W. J. Chang, K. Y. Park, Y. Zhu, C. Wolverton, M. C. Hersam, and E. A. Weiss, "N-Doping of Quantum Dots by Lithium Ion Intercalation," *ACS Applied Materials and Interfaces*, vol. 12, pp. 36523–36529, 2020.

[92] J. J. Geuchies, B. Brynjarsson, G. Grimaldi, S. Gudjonsdottir, W. Van Der Stam, W. H. Evers, and A. J. Houtepen, "Quantitative Electrochemical Control over Optical Gain in Quantum-Dot Solids," *ACS Nano*, vol. 15, pp. 377–386, 2021.

[93] W. K. Koh, A. Y. Koposov, J. T. Stewart, B. N. Pal, I. Robel, J. M. Pietryga, and V. I. Klimov, "Heavily doped n-type PbSe and PbS nanocrystals using ground-state charge transfer from cobaltocene," *Scientific Reports*, vol. 3, p. 2004, 2013.

[94] M. Shim and P. Guyot-sionnest, "N-type collidal semiconductor nanocrystals," *Nature*, vol. 407, pp. 981–983, 2000.

[95] J. H. Engel, Y. Surendranath, and A. P. Alivisatos, "Controlled chemical doping of semiconductor nanocrystals using redox buffers," *Journal of the American Chemical Society*, vol. 134, pp. 13200–13203, 2012.

[96] Y. K. Jung, J. I. Kim, and J.-K. Lee, "Thermal decomposition mechanism of single-molecule precursors forming metal sulfide nanoparticles," *Journal of the American Chemical Society*, vol. 132, pp. 178–184, 2010.

[97] M. H. Hudson, M. Chen, V. Kamysbayev, E. M. Janke, X. Lan, G. Allan, C. Delerue, B. Lee, P. Guyot-Sionnest, and D. V. Talapin, "Conduction Band Fine Structure in Colloidal HgTe Quantum Dots," *ACS Nano*, vol. 12, pp. 9397–9404, 2018.

[98] M. Kasha, "Characterization of electronic transitions in complex molecules," *Discussions of the Faraday Society*, vol. 9, pp. 14–19, 1950.

[99] H. Yin, A. Akey, and R. Jaramillo, "Large and persistent photoconductivity due to hole-hole correlation in CdS," *Physical Review Materials*, vol. 2, p. 084602, 2018.

[100] P. de Vries and A. Lagendijk, "Resonant scattering and spontaneous emission in dielectrics: Microscopic derivation of local-field effects," *Physical Review Letters*, vol. 81, pp. 1381–1384, 1998.

[101] E. Yablonovitch, T. J. Gmitter, and R. Bhat, "Inhibited and enhanced spontaneous emission from optically thin AlGaAs/GaAs Double Heterostructures," *Physical Review Letters*, vol. 61, pp. 2546–2549, 1988.

[102] R. C. Hilborn, "Einstein coefficients, cross sections, f values, dipole moments, and all that," *American Journal of Physics*, vol. 50, pp. 982–986, 1982.

[103] D. Toptygin, "Effects of the Solvent Refractive Index and Its Dispersion on the Radiative Decay Rate and Extinction Coefficient of a Fluorescent Solute," *Journal of Fluorescence*, vol. 13, pp. 201–219, 2003.

[104] N. J. Orfield, J. R. McBride, J. D. Keene, L. M. Davis, and S. J. Rosenthal, "Correlation of atomic structure and photoluminescence of the same quantum dot: Pinpointing surface and internal defects that inhibit photoluminescence," *ACS Nano*, vol. 9, pp. 831–839, 2015.

[105] A. J. Muhowski, A. M. Muellerleile, J. T. Olesberg, and J. P. Prineas, "Internal quantum efficiency in 6.1 Å superlattices of 77% for mid-wave infrared emitters," *Applied Physics Letters*, vol. 117, p. 061101, 2020.

[106] D. Jung, S. Bank, M. L. Lee, and D. Wasserman, "Next-generation mid-infrared sources," *Journal of Optics*, vol. 19, p. 123001, 2017.

[107] A. E. Siegman, *Lasers*. University Science Books, 1986.

[108] E. Humeres, N. A. Debacher, J. D. Franco, B. S. Lee, and A. Martendal, "Mechanisms of acid decomposition of dithiocarbamates. 3. Aryldithiocarbamates and the torsional effect," *Journal of Organic Chemistry*, vol. 67, pp. 3662–3667, 2002.

[109] T. Kim, Y. K. Jung, and J.-K. Lee, "The formation mechanism of CdSe QDs through the thermolysis of Cd(oleate)2 and TOPSe in the presence of alkylamine," *Journal of Materials Chemistry C*, vol. 2, pp. 5593–5600, 2014.

[110] I. G. Dance, R. G. Garbutt, D. C. Craig, and M. L. Scudder, "The Different Nonmolecular Polyadamantanoid Crystal Structures of Cd(SPh)2 and Cd(SC6H4Me-4)2: Analogies with Microporous Aluminosilicate Frameworks1," *Inorganic Chemistry*, vol. 26, pp. 4057–4064, 1987.

[111] H. Qin, Y. Niu, R. Meng, X. Lin, R. Lai, W. Fang, and X. Peng, "Single-dot spectroscopy of zinc-blende CdSe/CdS core/shell nanocrystals: Nonblinking and correlation with ensemble measurements," *Journal of the American Chemical Society*, vol. 136, pp. 179–187, 2014.

[112] J. Zhou, M. Zhu, R. Meng, H. Qin, and X. Peng, "Ideal CdSe/CdS Core/Shell Nanocrystals Enabled by Entropic Ligands and Their Core Size-, Shell Thickness-, and Ligand-Dependent Photoluminescence Properties," *Journal of the American Chemical Society*, vol. 139, pp. 16556–16567, 2017.

[113] P. Guyot-Sionnest and M. A. Hines, "Intraband transitions in semiconductor nanocrystals," *Applied Physics Letters*, vol. 72, pp. 686–688, 1998.

[114] G. Allan and C. Delerue, "Tight-binding calculations of the optical properties of HgTe nanocrystals," *Physical Review B*, vol. 86, p. 165437, 2012.

[115] S. Einfeldt, F. Goschenhofer, C. R. Becker, and G. Landwehr, "Optical Properties of HgSe," *Physical Review B*, vol. 51, pp. 4915–4925, 1995.

[116] W. Szuszkiewicz, A. M. Witowski, and M. Grynberg, "The Dynamic Dielectric Function in HgSe and HgTe," *Physica Status Solidi (B)*, vol. 87, pp. 637–645, 1978.

[117] S. Ninomiya and S. Adachi, "Optical properties of wurtzite CdS," *Journal of Applied Physics*, vol. 78, pp. 1183–1190, 1995.

[118] C. K. Duan and M. F. Reid, "Macroscopic models for the radiative relaxation lifetime of luminescent centers embedded in surrounding media," *Spectroscopy Letters*, vol. 40, pp. 237–246, 2007.

[119] A. Zangwill, *Modern Electrodynamics*. Cambridge University Press, 2012.

[120] F. Wang, H. Wan, Z. Ma, Y. Zhong, Q. Sun, Y. Tian, L. Qu, H. Du, M. Zhang, L. Li, H. Ma, J. Luo, Y. Liang, W. J. Li, G. Hong, L. Liu, and H. Dai, "Light-sheet microscopy in the near-infrared II window," *Nature Methods*, vol. 16, pp. 545–552, 2019.

[121] C. T. Jackson, S. Jeong, G. F. Dorlhiac, and M. P. Landry, "Advances in engineering near-infrared luminescent materials," *iScience*, vol. 24, p. 102156, 2021.

[122] F. Xia, M. Gevers, A. Fognini, A. T. Mok, B. Li, N. Akbari, I. E. Zadeh, J. Qin-Dregely, and C. Xu, "Short-Wave Infrared Confocal Fluorescence Imaging of Deep Mouse Brain with a Superconducting Nanowire Single-Photon Detector," *ACS Photonics*, vol. 8, pp. 2800–2810, 2021.

[123] G. Hong, S. Diao, J. Chang, A. L. Antaris, C. Chen, B. Zhang, S. Zhao, D. N. Atochin, P. L. Huang, K. I. Andreasson, C. J. Kuo, and H. Dai, "Through-skull fluorescence imaging of the brain in a new near-infrared window," *Nature Photonics*, vol. 8, pp. 723–730, 2014.

[124] H. Wan, J. Yue, S. Zhu, T. Uno, X. Zhang, Q. Yang, K. Yu, G. Hong, J. Wang, L. Li, Z. Ma, H. Gao, Y. Zhong, J. Su, A. L. Antaris, Y. Xia, J. Luo, Y. Liang, and H. Dai, "A bright organic NIR-II nanofluorophore for three-dimensional imaging into biological tissues," *Nature Communications*, vol. 9, p. 1171, 2018.

[125] J. A. Carr, D. Franke, J. R. Caram, C. F. Perkinson, M. Saif, V. Askoxylakis, M. Datta, D. Fukumura, R. K. Jain, M. G. Bawendi, and O. T. Bruns, "Shortwave infrared fluorescence imaging with the clinically approved near-infrared dye indocyanine green," *Proceedings of the National Academy of Sciences of the United States of America*, vol. 115, pp. 4465–4470, 2018.

[126] G. Hong, J. C. Lee, J. T. Robinson, U. Raaz, L. Xie, N. F. Huang, J. P. Cooke, and H. Dai, "Multifunctional in vivo vascular imaging using near-infrared II fluorescence," *Nature Medicine*, vol. 18, pp. 1841–1846, 2012.

[127] K. F. Freed and J. Jortner, "Multiphonon processes in the nonradiative decay of large molecules," *The Journal of Chemical Physics*, vol. 52, pp. 6272–6291, 1970.

[128] H. C. Friedman, E. D. Cosco, T. L. Atallah, S. Jia, E. M. Sletten, and J. R. Caram, "Establishing design principles for emissive organic SWIR chromophores from energy gap laws," *Chem*, vol. 7, pp. 3359–3376, 2021.

[129] S. Pradhan, M. Dalmases, N. Taghipour, B. Kundu, and G. Konstantatos, "Colloidal Quantum Dot Light Emitting Diodes at Telecom Wavelength with 18% Quantum Efficiency and Over 1 MHz Bandwidth," *Advanced Science*, vol. 9, p. 2200637, 2022.

[130] S. Pradhan, F. Di Stasio, Y. Bi, S. Gupta, S. Christodoulou, A. Stavrinadis, and G. Konstantatos, "High-efficiency colloidal quantum dot infrared light-emitting diodes via engineering at the supra-nanocrystalline level," *Nature Nanotechnology*, vol. 14, pp. 72–79, 2019.

[131] Y. Tsukasaki, M. Morimatsu, G. Nishimura, T. Sakata, H. Yasuda, A. Komatsuzaki, T. M. Watanabe, and T. Jin, "Synthesis and optical properties of emission-tunable PbS/CdS core-shell quantum dots for in vivo fluorescence imaging in the second near-infrared window," *RSC Advances*, vol. 4, pp. 41164–41171, 2014.

[132] M. Vasilopoulou, H. P. Kim, B. S. Kim, M. Papadakis, A. E. Ximim Gavim, A. G. Macedo, W. Jose da Silva, F. K. Schneider, M. A. Mat Teridi, A. G. Coutsolelos, and A. R. bin Mohd Yusoff, "Efficient colloidal quantum dot light-emitting diodes operating in the second near-infrared biological window," *Nature Photonics*, vol. 14, pp. 50–56, 2020.

[133] S. M. Tenney, V. Vilchez, M. L. Sonnleitner, C. Huang, H. C. Friedman, A. J. Shin, T. L. Atallah, A. P. Deshmukh, S. Ithurria, and J. R. Caram, "Mercury Chalcogenide Nanoplatelet–Quantum Dot Heterostructures as a New Class of Continuously Tunable Bright Shortwave Infrared Emitters," *The Journal of Physical Chemistry Letters*, vol. 11, pp. 3473–3480, 2020.

[134] M. V. Kovalenko, E. Kaufmann, D. Pachinger, J. Roither, M. Huber, J. Stangl, G. Hesser, F. Schäffler, and W. Heiss, "Colloidal HgTe nanocrystals with widely tunable narrow band gap energies: From telecommunications to molecular vibrations," *Journal of the American Chemical Society*, vol. 128, pp. 3516–3517, 2006.

[135] L. K. Sagar, G. Bappi, A. Johnston, B. Chen, P. Todorović, L. Levina, M. I. Saidaminov, F. P. García De Arquer, D. H. Nam, M. J. Choi, S. Hoogland, O. Voznyy, and E. H. Sargent, "Suppression of Auger Recombination by Gradient Alloying in InAs/CdSe/CdS QDs," *Chemistry of Materials*, vol. 32, pp. 7703–7709, 2020.

[136] Y. Chen, J. Vela, H. Htoon, J. L. Casson, D. J. Werder, D. A. Bussian, V. I. Klimov, and J. A. Hollingsworth, ""Giant" multishell CdSe nanocrystal quantum dots with suppressed blinking," *Journal of the American Chemical Society*, vol. 130, pp. 5026–5027, 2008.

[137] R. Lai, C. Pu, and X. Peng, "On-Surface Reactions in the Growth of High-Quality CdSe Nanocrystals in Nonpolar Solutions," *Journal of the American Chemical Society*, vol. 140, pp. 9174–9183, 2018.

[138] H. Liu and P. Guyot-Sionnest, "Photoluminescence lifetime of lead selenide colloidal quantum dots," *Journal of Physical Chemistry C*, vol. 114, pp. 14860–14863, 2010.

[139] N. C. Anderson and J. S. Owen, "Soluble, chloride-terminated CdSe nanocrystals: Ligand exchange monitored by 1H and 31P NMR spectroscopy," *Chemistry of Materials*, vol. 25, pp. 69–76, 2013.

[140] G. Shen, M. Chen, and P. Guyot-Sionnest, "Synthesis of Nonaggregating HgTe Colloidal Quantum Dots and the Emergence of Air-Stable n-Doping," *Journal of Physical Chemistry Letters*, vol. 8, pp. 2224–2228, 2017.

[141] X. Shen, J. C. Peterson, and P. Guyot-Sionnest, "Mid-infrared HgTe Colloidal Quantum Dot LEDs," *ACS Nano*, 2022.

[142] E. Lhuillier, S. Keuleyan, P. Zolotavin, and P. Guyot-Sionnest, "Mid-infrared HgTe/As2S3 field effect transistors and photodetectors," *Advanced Materials*, vol. 25, no. 1, pp. 137–141, 2013.

[143] Z. Ning, X. Gong, R. Comin, G. Walters, F. Fan, O. Voznyy, and E. Yassitepe, "Quantum-dot-in-perovskite solids," 2015.

[144] K. F. Chou and A. M. Dennis, "Förster resonance energy transfer between quantum dot donors and quantum dot acceptors," *Sensors (Switzerland)*, vol. 15, no. 6, pp. 13288–13325, 2015.